論文 / 著書情報
Article / Book Information

題目(和文)	白金微粒子を堆積したイオンビーム照射炭素材料に対する分光学的研究
Title(English)	Spectroscopic Study on Ion-beam-irradiated Carbon Materials with Platinum Nanoparticles
著者(和文)	木全哲也
Author(English)	Tetsuya Kimata
出典(和文)	学位:博士(理学), 学位授与機関:東京工業大学, 報告番号:甲第11570号, 授与年月日:2020年9月25日, 学位の種別:課程博士, 審査員:中村 一隆,笹川 崇男,吉本 護,舟窪 浩,松田 晃史,和田 裕之,多田 朋史
Citation(English)	Degree:Doctor (Science), Conferring organization: Tokyo Institute of Technology, Report number:甲第11570号, Conferred date:2020/9/25, Degree Type:Course doctor, Examiner:,,,,,,
学位種別(和文)	博士論文
Type(English)	Doctoral Thesis

Tetsuya Kimata

Spectroscopic Study on Ion-beam-irradiated Carbon Materials with Platinum Nanoparticles

Doctoral Thesis
Tokyo Institute of Technology, Japan

Supervisor: Prof. Kazutaka Nakamura

August 2020

Acknowledgements

To begin, I would like to thank my supervisor, Prof. Kazutaka Nakamura, for his instruction and encouragement. I could not start my great journey in the Laboratory for Materials and Structures, Institute of Innovative Research, Tokyo Institute of Technology (Tokyo Tech) without your acceptance of my application for admission. He provided an opportunity for discussion on the weekends for me because I could not come to the laboratory on weekdays due to my job. Without his support and guidance, I could not have so much as submitted my doctoral dissertation. He helped me to enhance my ability to be a physicist and I am very lucky to work with you.

I would also like to express my gratitude to my sub-supervisors, Prof. Tomofumi Tada (present position: Kyushu University) and Prof. Takao Sasagawa, for their sincere guidance and valuable suggestions. Especially, I would like to thank Prof. Tomofumi Tada for his comments on the electronic structure of my sample. I could not have discussed the result of DFT calculation deeply without his suggestion.

I would also like to thank Prof. Takayuki Terai and Mr. Kenta Kakitani of the Department of Nuclear Engineering and Management, School of Engineering, The University of Tokyo (UTokyo), and Dr. Shunya Yamamoto and Dr. Tetsuya Yamaki of the National Institutes for the Quantum and Radiological Science and

Technology (QST) for their technical support and discussion related ion-beam irradiation experiments.

I would also like to thank Dr. Iwao Shimoyama and Dr. Daiju Matsumura of the Japan Atomic Energy Agency, and Prof. Akihiro Iwase of the Osaka Prefecture University for their technical support of the synchrotron radiation experiment at KEK-PF and SPring-8. I also want to thank Dr. Hiroyuki Okazaki, Dr. Akira Idesaki, Dr. Hiroshi Koshikawa, and Dr. Tomitsugu Taguchi of QST, Prof. Mao Wei and Mr. Sho Kato of UTokyo, and Dr. Tomohiro Kobayashi of RIKEN for their advice on electrochemical measurement, TEM observation, DFT calculation, and ion-beam irradiation. I would also like to Prof. Yosuke Kayanuma and Prof. Fujio Minami of the Nakamura research group of Tokyo Tech for their advice and support on the theory and experiment of the coherent control of optical phonons. I would like to thank Prof. Mamoru Yoshimoto, Prof. Hiroshi Funakubo, Prof. Hiroyuki Wada and Prof. Akifumi Matsuda for their guidance, suggestions, and arrangements for the preparation of my doctoral thesis.

I also wish to thank Prof. Kazuhiko Odaka, Prof. Masahiro Kitajima, and Prof. Seiji Sakoda for their continuous encouragement. It was under their guidance and advice that I finished an undergraduate course in the Department of Applied Physics, National Defense Academy, in 2013. It was also generous of them to teach me so much about academic life. I would also like to thank Dr. Takashi Matsumoto and Dr. Tatsuhiro Fujita, who I studied with at the Odaka research group.

I would also like to thank all members of the Nakamura research group of Tokyo Tech, the secretary, Ms. Aki Miyamoto, and students, Mr. Yuki Okuda, Mr. Rintaro Kase, Ms. Riho Tanaka, Mr. Takashi Kitashima, Mr. Yu Mishima, Mr. Kazuma Yoda, Mr. Yuto Sasase, Ms. Hana Matsumoto, Mr. Hiromu Matsumoto, Mr. Gordon Han Ying Li, Mr. Hiroyuki Tanabe, Mr. Yuya Furusho,

Mr. Tsukasa Maruhashi, Mr. Masaki Suda, Mr. Itsuki Takagi, and Ms. Ryoko Yagi, for their encouragement and warm hospitality. I am so happy and lucky to be one of the member in the research group.

I thank all my colleagues of the Ground Systems Research Center, ATLA, Ministry of Defense who support and help me during my doctoral course. Especially, I want to thank Dr. Hirotomo Nakajima for his technical advice on the MATLAB script.

Finally, immeasurable thanks are due to my parents, Takatoshi and Michiko. I could not complete my work if they had not provided me with a good educational environment and many opportunities for challenging myself. I would like to thank my grandparents, Yujiro and Akiko, who have always supported me ever since I was born. Especially, I would like to dedicate this thesis to my grandmother, who passed away just before I entered the doctoral course. I also thank my girlfriend, Akari, for her companionship and support.

Thanks to all this tremendous support, I was able to line my doctoral student life for 3 years safely while working in the government office as a researcher. I am happy to create great memories.

August 2020

Tetsuya Kimata

List of Published Articles

Parts of this thesis have been published in the following journal articles:

1. T. Kimata, K. Yoda, H. Matsumoto, H. Tanabe, F. Minami, Y. Kayanuma, K.G. Nakamura. *Coherent control of 40-THz optical phonons in diamond using femtosecond optical pulses.* Physical Review B **101**, 174301 (2020). [press release]
2. T. Kimata, K. Kakitani, S. Yamamoto, T. Yamaki, T. Terai, K.G. Nakamura. *Platinum nanoparticles on HOPG surface modified by 380 keV Ar^+ irradiation: TEM and Raman studies.* Radiation Effects and Defects in Solids **175**, 433 (2020).
3. H. Okazaki, K. Kakitani, T. Kimata, A. Idesaki, H. Koshikawa, D. Matsumura, S. Yamamoto, T. Yamaki. *Changes in electronic structure of carbon supports for Pt catalysts induced by vacancy formation due to Ar^+ irradiation.* The Journal of Chemical Physics **152**, 124708 (2020).
4. T. Kimata, K. Kakitani, S. Yamamoto, T. Yamaki, T. Terai, K.G. Nakamura. *Raman spectroscopy of Ar^+-irradiated graphite surfaces supporting platinum nanoparticles.* Nuclear Instruments and Methods in Physics Research Section B **444**, 6 (2019).
5. K. Kakitani, T. Kimata, T. Yamaki, S. Yamamoto, T. Taguchi, T. Kobayashi, W. Mao, T. Terai. *The interface between platinum nanoparticle catalysts*

and an Ar^+-irradiated carbon support. Surface and Coatings Technology **355**, 259 (2018).

6. K. Kakitani*, T. Kimata*, T. Yamaki, S. Yamamoto, D. Matsumura, T. Taguchi, T. Terai. *X-ray absorption study of platinum nanoparticle catalysts on an ion-irradiated carbon support.* Radiation Physics and Chemistry **153**, 152 (2018). [*equally contribution]
7. T. Kimata, S. Kato, T. Yamaki, S. Yamamoto, T. Kobayashi, T. Terai. *Platinum nanoparticles on the glassy carbon surface irradiated with argon ions.* Surface and Coatings Technology **306**, 123 (2016).

Parts of this thesis have been putted on the following preprint server:

1. T. Kimata, K. Kakitani, S. Yamamoto, I. Shimoyama, D. Matsumura, A. Iwase, W. Mao, T. Kobayashi, T. Yamaki, T. Terai. *Activity enhancement of platinum oxygen-reduction electrocatalysts using ion-beam induced defects.* ChemRxiv. Preprint. (2017).
   https://doi.org/10.26434/chemrxiv.5554159.v1.

Contents

Chapter 1

Introduction

1.1 Background

In this section, I review several studies on the use of lattice defects in carbon materials and describe the ion-beam techniques, which is a method of generating lattice defects.

1.1.1 Defects in carbon materials

Defects in matter cause the various charge and spin states according to the Fermi level, and generate the several electronic states; as a result, the interesting electrical, optical, and magnetic functions are obtained. Thus, many scientists have conducted research related to the lattice defects in the semiconductors, carbon-based materials, and other materials. The research of lattice defects based on theoretical approaches such as first-principle calculation has been reported because of the experimental difficulty of observing and evaluating defects in matter. Apart from these theoretical researches, the new functional materials using lattice defects have been studied. Recently, lattice defects in carbon materials such as diamond, graphene, and graphite, are of interest to researchers; carbon has seen use in diverse fields including materials science,

condensed-matter physics, and mechanical and electrical applications.

1.1.1.1 Pt cluster on defective graphite

One of the most important applications is the graphitic structure with vacancies and defects for the development of highly active electrocatalysts. The platinum (Pt) nanoparticles on carbon materials are excellent catalysts for various fuel cell reactions, Pt is widely used in both anode and cathode electrodes in the proton exchange membrane fuel cell (PEMFC); however, further activity improvements are still required.

Previously, researchers proposed that the surface modification of the carbon support by thermal, chemical, or plasma treatment enhanced the catalytic activity of the Pt nanoparticles [1]. In these treatments, the particle size and dispersibility of the Pt nanoparticles were controlled by introducing surface functional groups onto the carbon supports. On the other hand, the modification of carbon supports expecting interfacial interaction has been also proposed. The electronic structures of the Pt nanoparticles are modulated through the orbital hybridization between Pt and C [2–4], which is termed as "Pt−C bonding". The electronic property of a Pt cluster on the defective graphitic structure has been investigated theoretically by computer calculation based on density functional theory [5–7]. The formation of Pt−C bonding is increased by defect vacancies of the carbon support [5], and the defective carbon support enhances the ORR activity of the Pt nanoparticles [6]. However, the details of these interfacial structures and the mechanism of activity enhancement have not been experimentally elucidated due to the difficulty of controlling the interfacial structure. Although not the Pt nanoparticles on carbon support with defect vacancies, the Pt nanoparticles on boron carbide and sulfur-doped carbon support were evaluated experimentally for catalytic activity and electronic structure in previous studies [8, 9]. These studies commonly expect to improve the catalytic prop-

erties by the metal-support interaction which is Pt-carbon support interaction (Pt−C interaction) in these cases.

In order to confirm that defect vacancy in the carbon support enhances the ORR activity of Pt nanoparticles and to elucidate the mechanism of the activity enhancement, precise manipulation of the Pt/C interfacial structure is required in a real system.

1.1.1.2 NV center in diamond

The lattice defect in diamond has been also studied for the quantum devices and applications; the defect is called the nitrogen-vacancy center (NV center). An NV center is composed of substitutional nitrogen (N) and a vacancy (V) on adjacent lattice sites in diamond and is expected as a quantum bit and quantum sensor that can operate at room temperature [10–15]. The electron spin at NV centers can be manipulated by applying electric and magnetic fields or light, resulting in sharp resonances in the intensity and wavelength of the photoluminescence.

Recently, the device-development for high-sensitivity quantum sensing has launched. However, fundamental studies such as preparation of high-quality samples, characterization of physical properties, and control of quantum states continue to be carried out, and interesting studies are still being reported. On sample preparation, the fabrication methods by the irradiation of neutron [16], electron [17–19], and ion-beam [20, 21] are reported as a method for high-quality NV centers. Besides, nonlinear optical effects induced by NV centers and the method of coherent optical manipulation of individual nuclear spin in diamond with NV centers are reported quite recently [22,23]. Thus, even though device development has begun, study at the basic level is still at the frontier in the research field.

1.1.2 Ion-beam modification

The function of solid-state materials is closely related to its lattice defects, the control of lattice defects is one of the basic concepts for developing new functional materials. Ion irradiation is well-known as a versatile tool for manipulating the physical, chemical, and magnetic properties of the host materials due to irradiation effects [24]. The ion-beam can precisely control lattice defects in materials because the ion-beam has the parameters of energy, ion species, and fluence. The interaction between ion-beam and solid and the ion-beam modification of carbon materials are described below.

1.1.2.1 Interactions between ion-beam and solid

The interactions between ion-beam and solid for each energy range are described below [25, 26], and the schematics are shown in Fig. 1.1. The ion-beam deposition is known as one of the methods for thin-film formation, an ion-beam of the element to be deposited is used at energies of 1 to several hundred eV (Fig. 1.1 (a)). The sputtering of solid surface and the implantation into materials cause at several 100 eV to several 10 keV and at more than several 10 keV, respectively. The ion-beam sputtering is often used as a pretreatment for surface analysis to remove contamination of the sample surface. In ion-beam implantation, the novel gas ion beams (He, Ar, Xe, and Kr) and the other ion beams (*e.g.* transition metal elements) are often used for the introduction of defect vacancy (Fig. 1.1 (c)) and doping (Fig. 1.1 (d)), respectively.

I describe the sputtering and implantation which are effects of the keV order irradiation. Sputtering is a phenomenon in which a part of solid atoms with kinetic energy obtained by nuclear collision has a kinetic component opposite to the incident ion, which causes it to jump out of the solid surface (Fig. 1.1(b)). The ratio of the number of solid atoms emitted from the surface to the number of ions injected is called the sputtering yield [27]. The sputtering yield is not

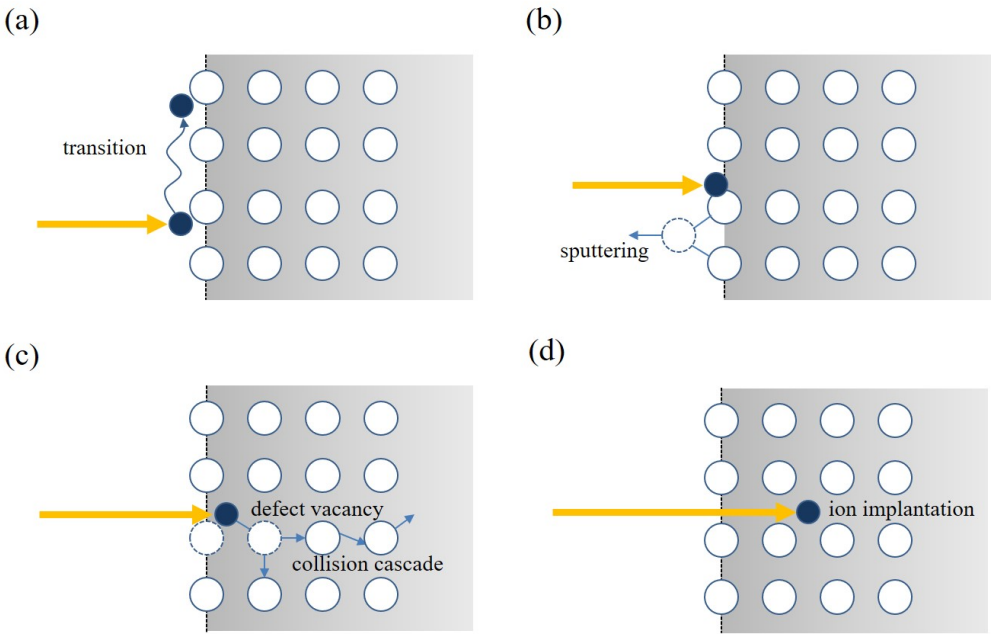

Fig. 1.1: Schematic of the interaction between ion-beam and solid surface: (a) deposition (b) sputtering (c) implantation (defect introduction) (d) implantation (doping).

only dependent on the incident energy of the ions, but also strongly depends on the combination of ion spices and solid types. When the kinetic energy of the ions exceeds a few 100 eV, the sputtering yield is greater than 1, resulting in the shaving of solids. Up to a certain level of ion-energy, energy conversion to the nucleus occurs near the surface layer of the solid, and sputtering is likely to occur; the higher the ion-energy, the higher the sputtering yield. As the energy of the ions increases, there is less energy transfer with the atoms close to the surface layer, resulting in a disturbance of the atomic positions deep in the solid where the incident energy is smaller. Sputtering occurs if solid atoms with energy from the collision jump out from the surface, but the number of atoms traveling to the surface decreases as the ion-energy increases. That is, above a certain energy, the sputtering yield decreases as the energy of the incident ions increases.

In the case of ion implantation into a solid, the penetrating ion loses energy due to the interaction with the solid atom. The energy that an ion loses per

unit length is called stopping power or linear energy transfer (LET). Among the stopping power, the power due to elastic collisions is the nuclear stopping power, S_n, and the power due to inelastic collisions is electronic stopping power, S_e. The LET is obtained as the sum of nuclear stopping power and electronic stopping power,

$$\frac{dE}{dx} = S_n + S_e. \tag{1.1}$$

In general, nuclear stopping power is dominant over electronic stopping power only in the case of low-energy ion irradiation, while electronic stopping power is more dominant at higher energies. As an example, the LET and each stopping power of graphite with a density of 2.2 g/cm^3 irradiated with keV-ordered Ar ion are calculated by the stopping and range of ions in matter (SRIM) code [28] and shown in Fig. 1.2. It can be seen that the electronic stopping power is more than nuclear stopping power at above approximately 100 keV in this condition.

The atoms ejected from the host materials by low-energy ion-beam irradiation, which means sputtering, recover the defective structure by filling the vacancies; the low-energy ion-beam irradiation is not suitable for the formation of defect vacancy. Since much of the energy of the incident particles is lost due to electronic excitation on the high-energy ion-beam irradiation, high-density defects can be introduced into the region until the ion-stopping depth. Therefore, ion-energy whose electronic stopping power is higher than the nuclear stopping power may be useful for introducing lattice defects into the host material.

1.1.2.2 Ion-beam modification of carbon materials

Ion-beam irradiation is also well known as a modification tool for carbon materials. One of the characteristics of carbon materials is that they exhibit widely different properties depending on their physical structure and chemical bonding forms. Another feature is that it is difficult to add impurities to the carbon alone. Graphite is known as a special case; certain elements such as fluorine

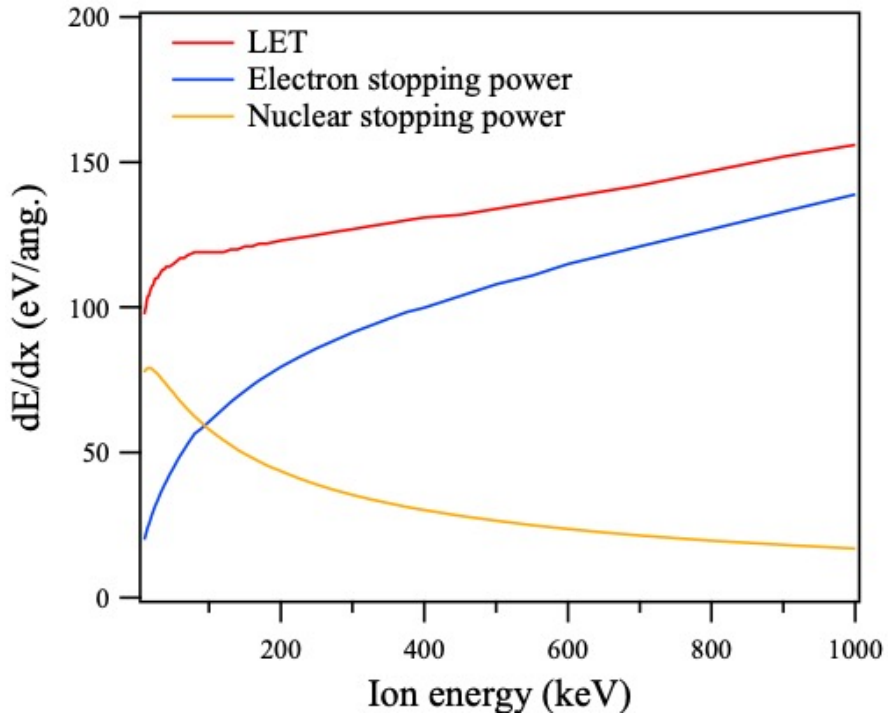

Fig. 1.2: The LET, electronic stopping power, and nuclear stopping power versus ion energy simulated by using the SRIM code when the graphite (density: 2.2 g/cm^3) is irradiated with Ar ions.

can be added by intercalation. The carbon surface is expected to be highly functional and multifunctional by manipulating the structure and adding impurities. Therefore, many studies using ion-beam irradiation have been carried out [29]. The ion irradiation in graphite has been extensively studied in connection with the research such as ion implantation and graphite intercalation compounds, the graphite surface has been modified by particles irradiation using various ion species and kinetic energy [30–33]. Also, upon implantation of ions into a transparent natural diamond, the diamond becomes colored and the surface exhibits a concomitant electrical conductivity. The electrical conductivity is thought to be caused by the breakdown of the diamond structure. The ion-beam irradiation into a glassy carbon has also been studied. Glassy carbon is a sintered form of graphite with a density of about 1.5 g/cm^2, which is lower than that of graphite. However, it is used as electrode material in electrochemistry (model electrode) and high-temperature crucible because of its inertness, electrical conductivity, thermal stability, and impermeability. It has been reported that ion-implantation improves the wear resistance [24], wettability [34], and electrochemical properties [35] of glassy carbon. An estimate of the defect density introduced into the glassy carbon by ion implantation has also been reported [36, 37].

1.2 Objective

As mentioned above, lattice defects in carbon materials create various functionalities. Since ion-beam is a powerful tool for modifying carbon materials, ion-beam technology is expected to greatly promote the development of functional carbon materials.

In this thesis, I focus the Pt nanoparticles on defective carbon supports as introduced in the previous section. Although it has been theoretically suggested that Pt clusters on graphite structures with vacancy exhibit high oxygen reduction reaction (ORR) activity, the electronic state, interfacial structure, and

functionality have not been clarified in real systems due to the difficulty of manipulating the defective structure experimentally. In order to improve the ORR activity of the Pt nanoparticles, I proposed to use ion-beam irradiation to introduce lattice defects into the carbon support. In fact, the Pt nanoparticles on Ar^+-irradiated carbon supports were found to be more active than those on non-irradiated one.

Therefore, the goal of this thesis is to clarify the influence of ion-beam irradiation on the defect and electronic structure of the carbon materials with Pt nanoparticles (Fig. 1.3). In order to achieve this goal, I will elucidate the following issues by spectroscopic and computational methods.

1. To clarify the influence of ion-beam irradiation on the electronic structure of Pt/C interface.
2. To clarify the defect structure on HOPG surfaces irradiated with ion beams.
3. To confirm the decrease in the d-band center of Pt due to the defect structure in graphite.
4. To make prospects for revealing the defective structure and electronic state of carbon materials with ultrafast dynamics.

1.3 Outline

The organization of this thesis is as follows (Fig. 1.4).

Chapter 2 examines the catalytic activity of the Pt nanoparticles on the Ar^+-irradiated glassy carbon substrates. The ORR activity of the Pt nanoparticles on Ar^+-irradiated glassy carbon substrates is measured by electrochemical method.

Chapter 3 discusses the electronic states of the Pt nanoparticles on the Ar^+-irradiated glassy carbon and HOPG surfaces. Firstly, the sample preparation of the Pt nanoparticles on the Ar^+-irradiated carbon substrates is described.

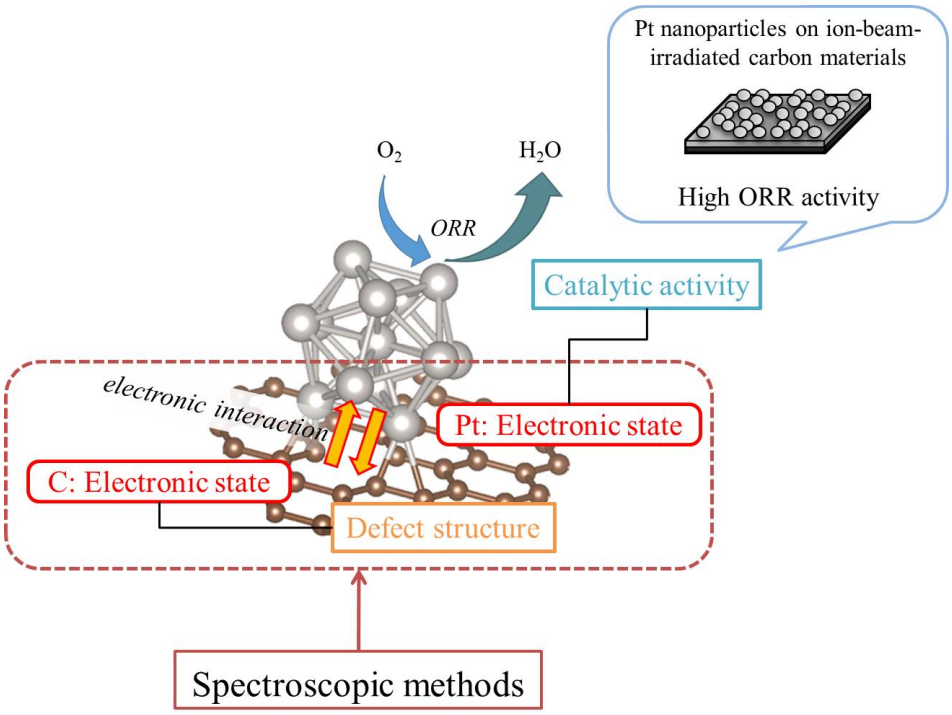

Fig. 1.3: Objective of this thesis.

The X-ray spectroscopy is performed for the prepared samples to clarify the electronic states.

In Chapter 4, the Ar^+-irradiated HOPG with Pt nanoparticles is investigated by Raman spectroscopy. The characteristic peaks of Raman spectra reveal the defect structure of irradiated HOPG surfaces. The number of point defects at the Pt/C interface is estimated by using the phonon correlation length which is obtained by the intensity ratio of G and D peaks.

The theoretical calculations for the Pt cluster on defective graphite structures are discussed in Chapter 5. The Pt_{13} cluster on the graphite structure with defect-vacancies is modeled to investigate the influence of the defective structure in carbon support on the electronic state of Pt atoms. The catalytic activity is predicted using the d-band centers obtained from the density of the state of Pt.

Chapter 6 discusses the ultrafast dynamics and coherent control of optical

phonons. These are fundamental studies to elucidate the influence of the lattice defects in carbon materials on the ultrafast dynamics. The coherent control of optical phonons in diamond by femtosecond optical pulses is treated theoretically and experimentally.

Chapter 7 presents the conclusion of this thesis.

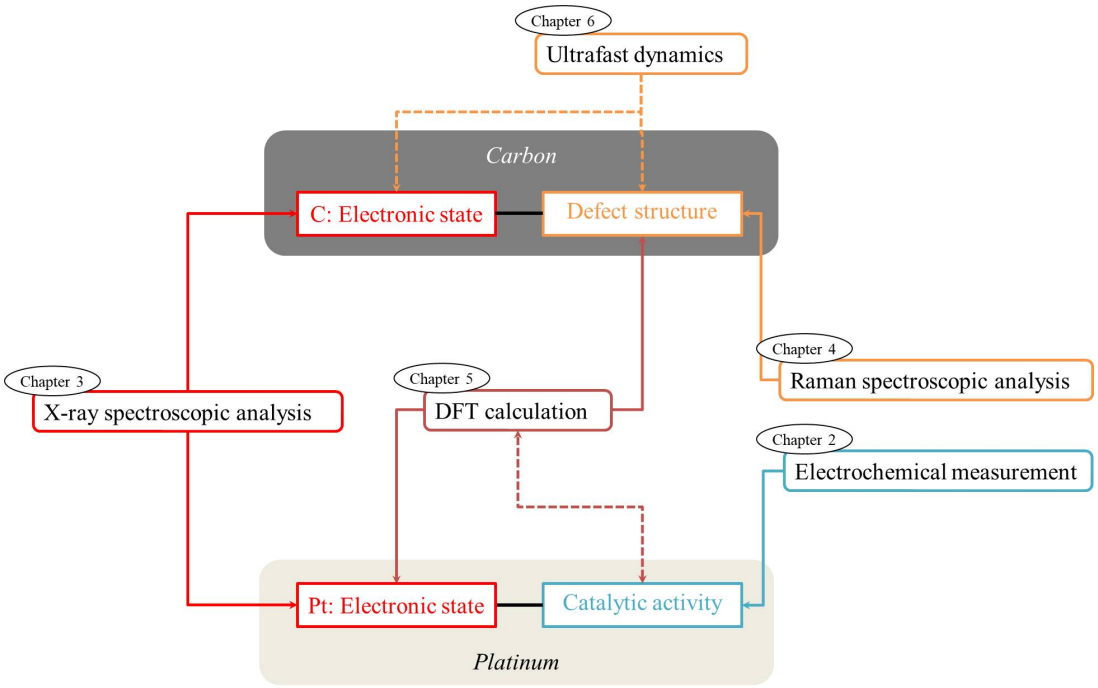

Fig. 1.4: Flowchart of this thesis.

References

[1] X. Yu, S. Ye. *Recent advances in activity and durability enhancement of Pt/C catalytic cathode in PEMFC: Part II: Degradation mechanism and durability enhancement of carbon supported platinum catalyst.* J. Power Sources **172**,145 (2007).

[2] G. Gupta, D. A. Slanac, P. Kumar, J. D. Wiggings-Camacho, J. Kim, R. Ryoo, K. J. Stevenson, K. P. Johnston. *Highly stable Pt/ordered graphitic mesoporous carbon electrocatalysts for oxygen reduction.* J. Phys. Chem. C **114**, 10796 (2010).

[3] E. Yoo, T. Okata, T. Akita, M. Kohyama, J. Nakamura, I. Honma. *Enhanced electrocatalytic activity of Pt subnanoclusters on graphene nanosheet surface.* Nano Lett. **9**, 2255 (2009).

[4] T. Kondo, Y. Iwasaki, Y. Honma, Y. Takagi, S. Okada, J. Nakamura. *Formation of nonbonding π electronic states of graphite due to Pt−C hybridization.* Phys. Rev. B **80**, 233408 (2009).

[5] I. Fampiou, A. Ramasubramaniam. *Binding of Pt Nanoclusters to Point Defects in Graphene: Adsorption, Morphology, and Electronic Structure.* J. Phys. Chem. C **116**, 6543 (2012).

[6] D.-H. Lim, J. Wilcox. *DFT-Based Study on Oxygen Adsorption on Defective Graphene-Supported Pt Nanoparticles.* J. Phys. Chem. C **115**, 22742 (2011).

[7] D.-H. Lim, J. Wilcox. *Mechanisms of the Oxygen Reduction Reaction on Defective Graphene-Supported Pt Nanoparticles from First-Principles.* J. Phys. Chem. C **116**, 3653 (2012).

[8] C. Jackson, G.T. Smith, D.W. Inwood, A.S.Leach, P.S. Whalley, M. Callisti, T. Polcar, A.E. Russell, P. Levecque, D. Kramer. *Electronic metal-support interaction enhanced oxygen reduction activity and stability of boron carbide supported platinum.* Nat. Commun. **8**, 15802 (2017).

[9] Q.-Q. Yan, D.-X. Wu, S.-Q. Chu, Z.-Q. Chen, Y. Lin, M.-X. Chen, J. Zhang, X.-J. Wu, H.-W. Liang. *Reversing the charge transfer between platinum and sulfur-doped carbon support for electrocatalytic hydrogen evolution*. Nat. Commun. **10**, 4977 (2019).

[10] H. Bernien, B. Hensen, W. Pfaff, G. Koolstra, M.S. Blok, L. Robledo, T.H. Taminiau, M. Markham, D.J. Twitchen, L. Childress, R. Hanson. *Heralded entanglement between solid-state qubits separated by three metres*. Nature **497**, 86 (2013).

[11] X. Zhu, S. Saito, A. Kemp, K. Kakuyanagi, S. Karimoto, H. Nakano, W.J. Munro, Y. Tokura, M.S. Everitt, K. Nemoto, M. Kasu, N. Mizuochi, K. Semba. *Coherent coupling of a superconducting flux qubit to an electron spin ensemble in diamond*. Nature **478**, 221 (2011).

[12] F. Dolde, I. Jakobi, B. Naydenov, N. Zhao, S. Pezzagna, C. Trautmann, J. Meijer, P. Neumann, F. Jelezko, J. Wrachtrup. *Room-temperature entanglement between single defect spins in diamond*. Nat. Phys. **9**, 139 (2013).

[13] N. Mizuochi, T. Makino, H. Kato, D. Takeuchi, M. Ogura, H. Okushi, M. Nothaft, P. Neumann, A. Gali, F. Jelezko, J. Wrachtrup, S. Yamasaki. *Electrically driven single-photon source at room temperature in diamond*. Nat. Photon. **6**, 299 (2012).

[14] A. Lohrmann, S. Pezzagna, I. Dobrinets, P. Spinicelli, V. Jacques, J.-F. Roch, J. Meijer, A. M. Zaitsev. *Diamond based light-emitting diode for visible single-photon emission at room temperature*. Appl. Phys. Lett. **99**, 251106 (2011).

[15] V.M. Acosta, E. Bauch, M. Ledbetter, C. Santori, K.M. Fu, P. Barclay, R.G. Beausoleil, H. Linget, J.-F. Roch, F. Treussart, S. Chemerisov, W. Gawlik, D. Budker. *Diamonds with a high density of nitrogen-vacancy centers for magnetometry applications*. Phys. Rev. B **80**, 115202 (2009).

[16] T. Astner, J. Gugler, A. Angerer, S. Wald, S. Putz, N.J. Mauser, M. Trupke, H. Sumiya, S. Onoda, J. Isoya, J. Schmiedmayer, P. Mohn, J. Majer. *Solid-state electron spin lifetime limited by phononic vacuum modes*. Nat. Mater. **17**, 313 (2018).

[17] A. Angerer, K. Streltsov, T. Astner, S. Putz, H. Sumiya, S. Onoda, J. Isoya, W.J. Munro, K. Nemoto, J. Schmiedmayer, J. Majer. *Superradiant emission from colour centres in diamond*. Nat. Phys. **14**, 1168 (2018).

[18] J. Jeske, D.W.M. Lau, X. Vidal, L.P. McGuinness, P. Reineck, B.C. Johnson, M.W. Doherty, J.C. McCallum, S. Onoda, F. Jelezko, T. Ohshima, T. Volz, J.H. Cole, B.C. Gibson,

A.D. Greentree. *Stimulated emission from nitrogen-vacancy centres in diamond.* Nat. Commun. **8**, 14000 (2017).

[19] M. Pfender, P. Wang, H. Sumiya, S. Onoda, W. Yang, D.B.R. Dasari, P. Neumann, X.-Y. Pan, J. Isoya, R.-B. Liu, J. Wrachtrup. *High-resolution spectroscopy of single nuclear spins via sequential weak measurements.* Nat. Commun. **10**, 594 (2019).

[20] T. Yamamoto, C. Müller, L.P. McGuinness, T. Teraji, B. Naydenov, S. Onoda, T. Ohshima, J. Wrachtrup, F. Jelezko, J. Isoya. *Strongly coupled diamond spin qubits by molecular nitrogen implantation.* Phys. Rev. B **88**, 201201(R) (2013).

[21] M. Haruyama, S. Onoda, T. Higuchi, W. Kada, A. Chiba, Y. Hirano, T. Teraji, R. Igarashi, S. Kawai, H. Kawarada, Y. Ishii, R. Fukuda, T. Tanii, J. Isoya, T. Ohshima, O. Hanaizumi. *Triple nitrogen-vacancy centre fabrication by $C_5N_4H_n$ ion implantation.* Nat. Commun. **10**, 2664 (2019).

[22] M. Motojima, T. Suzuki, H. Shigekawa, Y. Kainuma, T. An, M. Hase. *Giant nonlinear optical effects induced by nitrogen-vacancy centers in diamond crystals.* Opt. Express **27**, 32218 (2019).

[23] M.L. Goldman, T.L. Patti, D. Levonian, S.F. Yelin, M.D. Lukin. *Optical Control of a Single Nuclear Spin in the Solid State.* Phys. Rev. Lett. **124**, 153203 (2020).

[24] M. Iwaki, K. Takahashi, K. Yoshiida, Y. Okabe. *Improvement of wear properties of glassy carbon surface layer modified by ion implantation.* Nucl. Instrum. Meth. Phys. Res. B **39**, 700 (1989).

[25] Fuminori Fujimoto, Kenichiro Komaki: *Ion-beam Ko-gaku (in Japanese, Ion-beam Engineering)* Uchida Rokakuho Publishing (1995).

[26] Ion-beam Ouyou Gijutsu Iinkai: *Ion-beam Gijutsu No Kaihatsu (in Japanese, Development of Ion-beam Technology)* CMC (2001).

[27] Y. Yamamura, N. Matsunami, N. Itoh. *Theoretical studies on an empirical formula for sputtering yield at normal incidence.* Rad. Eff. **71**, 65 (1983).

[28] J.F. Ziegler, J.P. Biersack, U. Littmack, The Stopping Range of Ions in Solids, Pergamon Press, New York, 1985.

[29] M. Iwaki: *Ion-beam Shosya Niyoru Tansozai No Hyomen Kaisitsu (in Japanese, Surface modification of carbon materials by ion beam irradiation).* J. IEE Japan **118**, 690 (1998).

[30] B. S. Elman, M. Shayegan, M. S. Dresselhaus, H. Mazurek, and G. Dresselhaus. *Structural characterization of ion-implanted graphite.* Phys. Rev. B **25**, 4142 (1982).

[31] M. Kitajima, K. Aoki, M. Okada. *Observation of shape change in the Raman spectrum of graphite exposed to deuterium glow.* J. Nucl. Mater. **149**, 269 (1987).

[32] S. Mathew, B. Joseph, B.R. Sekhar, B.N. Dev. *X-ray photoelectron and Raman spectroscopic studies of MeV proton irradiated graphite.* Nucl. Instrum. Meth. Phys. Res. B **266**, 3241 (2008).

[33] K. Nakamura, M. Kitajima. *Real-time Raman measurement of graphite under Ar^+ irradiation.* Appl. Phys. Lett. **59**, 1550 (1991).

[34] M. Iwaki, M. Matsunaga, K. Terashima, H. Watanabe. *Tribology and Wettability of Na-ion Implanted Glassy Carbon.* 1998 International Conference on Ion Implantation Technology. Proceedings. 1026 (1999).

[35] K. Takahashi, M. Iwaki, H. Watanabe. *Effect of target temperature during nitrogen ion implantation on electrochemical properties of ion-implanted glassy carbon.* J. Electroanal. Chem. **396**, 541 (1995).

[36] S. Prawer, F. Ninio, I. Blanchonette. *Raman spectroscopic investigation of ion-beam-irradiated glassy carbon.* J. Appl. Phys. **68**, 2361 (1990).

[37] S. Prawer, C.J. Rossouw. *Structural investigation of helium ion-beam-irradiated glassy carbon.* J. Appl. Phys. **63**, 4435 (1988).

Chapter 2

Catalytic activity of the Pt nanoparticles for fuel cell applications

2.1 Introduction

The proton exchange membrane fuel cell (PEMFC) is a promising device that provides a highly efficient and clean source of energy. Many studies on related materials have been performed toward its widespread use [1,2]. Pt nanoparticles on a carbon material are excellent catalysts for various fuel cell reactions such as the hydrogen oxidation reaction, oxygen reduction reaction (ORR) [3], and methanol oxidation reaction; therefore, Pt is widely used in both anode and cathode electrodes in the PEMFC. The potential loss at the cathode, which is caused by relatively sluggish kinetics of the ORR, is a critical issue to be solved for further improvement of the PEMFC performance [4, 5].

In this chapter, we carry out electrochemical measurements of the Pt nanoparticles on the glassy carbon substrate irradiated with Ar^+ and then demonstrate that the Ar^+ irradiation improves their ORR activity.

2.2 Estimation methods for oxygen-reduction catalyst

2.2.1 Cyclic voltammetry

Electrochemical measurement is a means of investigating the electrical properties of electrodes and solutions by controlling the potential or current applied to the electrodes [6,7]. Cyclic voltammetry (CV) is one of the potentiodynamic electrochemical measurements, and measures the response of the current by varying the potential over time. In CV, a potentiostat is used to repeatedly change the potential within a certain range at a constant potential scan rate (mV/s) and the current associated with the electrode surface reaction is measured according to the potential change. CV is widely used for the characterization of electrodes and clarification of oxidation-reduction processes, as well as for the evaluation of catalytic layers in fuel cells.

The principle of CV is expressed by the Nernst equation,

$$E = E^{\circ} + \ln \frac{{a_R}^x}{{a_O}^y}, \tag{2.1}$$

where E and E° are the half-cell reduction potential and standard half-cell reduction potential, respectively. a is the chemical activity for the relevant species, where a_R is the activity of the reduced form and a_O is the activity of the oxidized form. When the potential E is manipulated, the equilibrium of the oxygen reduction reaction moves according to this equation, and change to a new equilibrium state. Electrochemical measurements that control the potential, such as CV, observe current fluctuations that follow the Nernst equation in the redox reaction.

The CV measurements are conducted by using potentiostat, electrodes, and solution. A potentiostat is a device to control the potential. A standard CV experiment employs three electrodes: working electrode, reference electrode, and counter electrode. The working electrode is the electrode that causes the oxygen reduction reaction. In this study, the working electrode is Pt nanoparticles

on Ar^+-irradiated glassy carbon substrates. The reference electrode is the electrode that has a stable and well-known electrode potential. Standard hydrogen electrode (SHE), silver chloride electrode (Ag/AgCl electrodes), and saturated calomel electrode (SCE) are commonly used as a reference electrode. In this study, KCl-saturated Ag/AgCl reference electrodes are used and converted to the value of the reversible hydrogen electrode (RHE). The counter electrode, along with the working electrode, provides a circuit over which current is applied. The potential of the counter electrode is usually not measured and is adjusted so as to balance the reaction occurring at the working electrode. In this study, a commonly used Pt wire is used as a counter electrode.

The method for evaluating the electrochemical active surface area (ECSA) of Pt by CV is described below. The response of Pt electrode in sulfuric acid and perchloric acid is well known, and the voltammogram is drawn as shown in Fig. 2.1. The vertical axis of the figure is the current value, and the reduction and oxidation currents are denoted by negative and positive values, respectively.

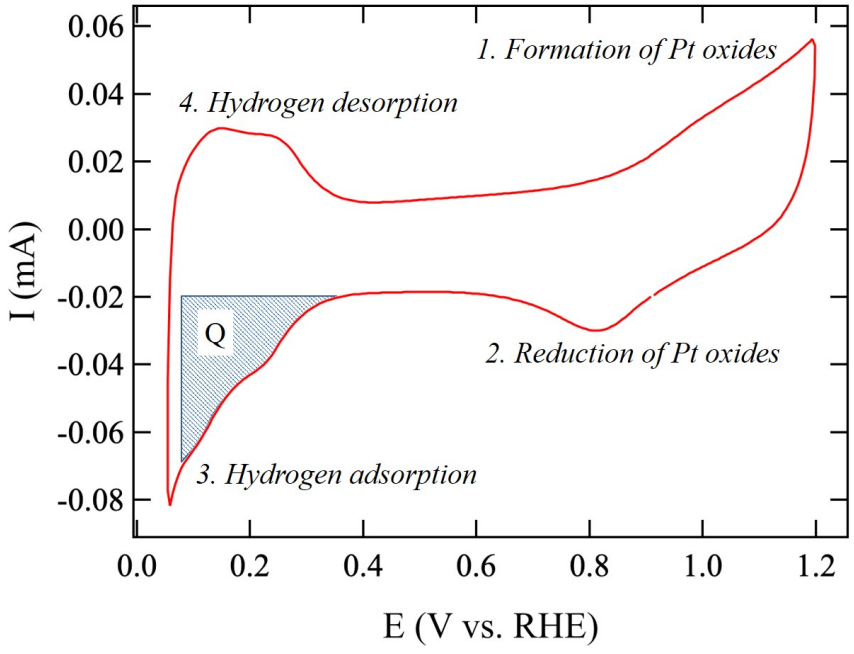

Fig. 2.1: Cyclic voltamogram for Pt nanoparticles on carbon substrate (solution: N_2-saturated 0.1 M $HClO_4$, scan range: 0.05∼1.20 V vs. RHE, scan rate: 50 mV/s, temperature: 25°C).

Each of the peaks in Fig. 2.1 is formed by the following process.

1. Pt+H_2O→Pt-O_x+2H^++2e^-

   When the potential is scanned in a positive direction, oxidation begins on the Pt surface from about 0.9 V.

2. Pt-O_x+2H^++2e^-→Pt+H_2O / $\frac{1}{2}O_2$+H_2O+2e^-→2OH^-

   A peak is observed around 0.8 V (sweep direction from 1.20 V to 0.05 V). This is due to the reduction reaction between the oxide film formed in process 1 and the dissolved oxygen.

3. Pt+H^++e^-→Pt-H

   As the potential is swept in a negative direction, a peak attributable to hydrogen adsorption is observed at around 0.2 V.

4. Pt-H→Pt+H^++e^-

   Corresponding to the peak in process 3, a hydrogen desorption peak is observed around 0.2 V (sweep direction from 0.05 V to 1.20 V).

The ECSA of Pt can be determined from the hydrogen adsorption/desorption peaks in the voltammogram (Fig. 2.1 process 3 and 4). The horizontal axis of the voltammogram is the potential, but since the potential sweep rate is constant, it can be converted into a time scale. Since the vertical axis is the current value (A/s), the area subtracting the background from the curve corresponds to the amount of charge. The blue shaded part Q in Fig. 2.1 represents the amount of charge transferred by the adsorption of hydrogen ions. Since the amount of hydrogen adsorption per unit area on Pt surface is known to be 210 μC/cm^2 [8], the ECSA of the electrode is calculated from

$$S\mathrm{cm}^2 = \frac{\mathrm{QmC}}{210\mu\mathrm{C/cm}^2}, \tag{2.2}$$

where Q is the charge amount.

2.2.2 Rotating disk electrode method

In the rotating disk electrode (RDE) method, the disk electrode is rotated to generate a vortex, which creates convection that draws the solution toward the electrode. Since the thickness of the diffusion layer remains constant while remaining thin, the diffusion speed will be constant if the rotation speed is sufficiently high. Therefore, the diffusion rate of the reactants and products can be controlled by the rotation speed of the electrode.

A voltammetric method where the current at a working electrode is measured while the potential between the working electrode and a reference electrode is swept linearly in time is called linear sweep voltammetry (LSV) [9]. Figure 2.2 shows the linear sweep voltammogram of Pt electrode in O_2-saturated 0.1 M $HClO_4$ at the rotating speed of1600 rpm. The presence of oxygen produces a negative current, that is, an oxygen reduction current. The current increases with decreasing potential and reaches a constant value at a sufficiently low po-

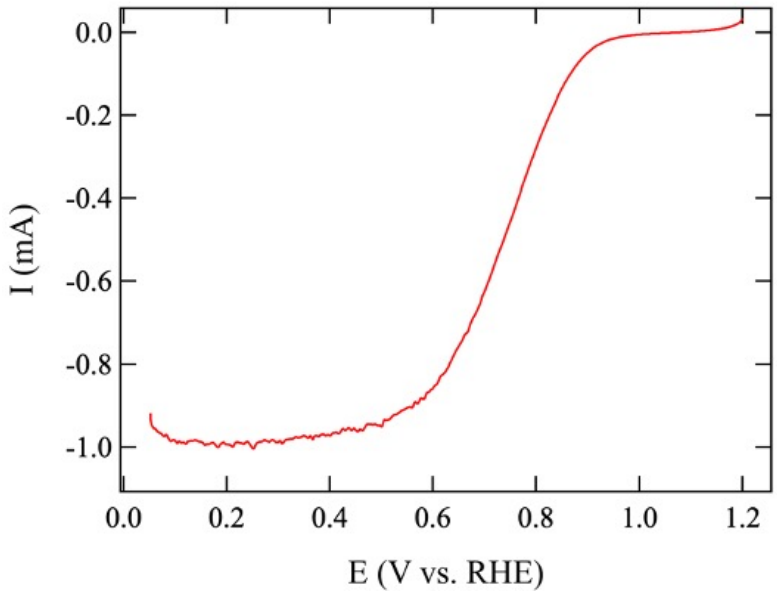

Fig. 2.2: Liner sweep voltammogram for Pt nanoparticles on carbon substrate (solution: O_2-saturated 0.1 M $HClO_4$, scan range: 0.05∼1.20 V vs. RHE, scan rate: 20 mV/s, temperature: 25°C, rotating speed: 1600 rpm).

tential. This current is called diffusion-limiting current.

In order to evaluate the catalytic activity, the kinetic current I_k is derived by removing the effect of diffusion from the measured current value I [10]. The kinetic parameters can be analyzed on the basis of the Koutecky-Levich equation [11]. The Koutecky-Levich equation models the measured electric current at an electrode from an electrochemical reaction in relation to the kinetic activity and the mass transport of reactants, and represented by

$$\frac{1}{I} = \frac{1}{I_k} + \frac{1}{I_l}, \tag{2.3}$$

where I is the measured current, I_k and I_l are the kinetic and diffusion-limiting currents, respectively. Therefore, the kinetic current I_k is obtained by

$$I_k = \frac{I \cdot I_l}{I_l - I}. \tag{2.4}$$

Since this is the total activity of the Pt sample involved in the reaction in the measurement, the measurement current density, i_k, which is the activity per reaction area, is derived from

$$i_k = \frac{I_k}{\mathrm{ECSA}}. \tag{2.5}$$

The measurement current density i_k corresponds to a specific activity (SA). In this study, the catalytic activity of prepared samples is compared using the obtained SA.

2.3 Experimental setup

2.3.1 Sample preparation

Unpolished 1-mm-thick glassy carbon substrates were obtained from Tokai Carbon Co., Ltd., Japan, and cut into 1 cm$\times$1 cm samples. Ar^+ irradiation was performed at an energy of 380 keV and the fluences between 1.0×10^{14} and 1.0×10^{16} ions/cm^2 using the ion implanter. The irradiated glassy carbon substrates were heated at 400°C in an N_2 atmosphere for 1 h in order to remove

water-related contamination. Pt nanoparticles were then deposited on this substrate by rf magnetron sputtering at room temperature. The sputtering time and plasma output were 60 s and 20 W, respectively, for all samples. The details of the sample preparation method and characterization are described in Chapter 3.

2.3.2 Electrochemical measurement

All the electrochemical measurements using the RDE were performed using an HZ-5000 Potentiostat (Hokuto Denko Corp., Japan), a three-electrode cell with a KCl-saturated Ag/AgCl reference electrode, and a Pt wire counter electrode. We used the experimental system from a previous study [12], as shown in Fig. 2.3 . The CV measurements were performed in an N_2-saturated 0.1 M $HClO_4$ electrolyte. The electrodes were cycled in the potential range between 0.05 and 1.20 V (vs. RHE) at a scan rate of 50 mV/s after electrochemical cleaning [13]. Subsequently, the LSV measurements using RDE were performed in the same potential range in an O_2-saturated 0.1 M $HClO_4$ at a scan rate of 20 mV/s with rotation speeds of 400, 900, 1600, and 2500 rpm [14].

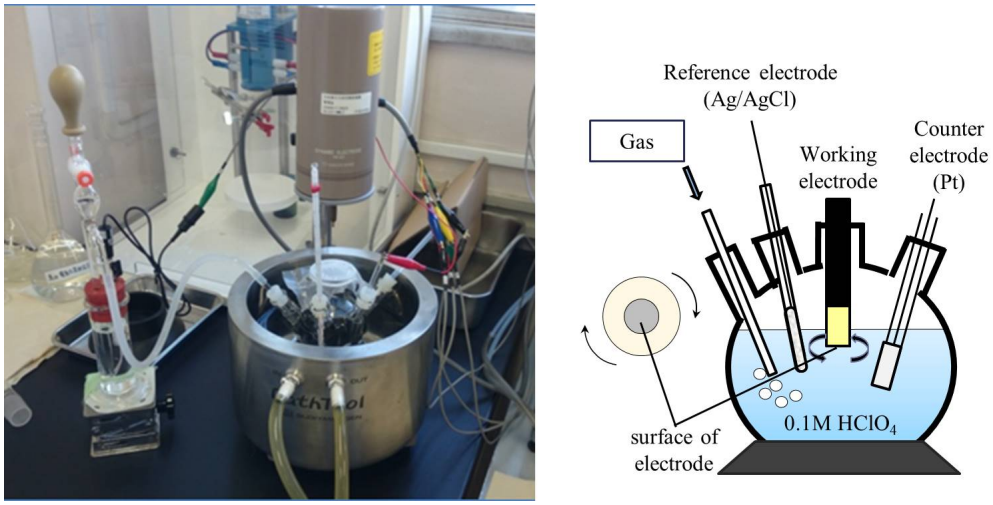

Fig. 2.3: Experimental system of electrochemical measurements.

2.4 Results and discussion

2.4.1 Electrochemical surface area

The ORR activity of the Pt nanoparticles on the Ar^+-irradiated glassy carbon substrates was measured by the RDE method. We used the specific activity (SA), which is defined as the activity standardized by the ECSA, of Pt within the sample. The SAs of the samples were determined by calculating i_k, the mass-transport-corrected kinetic current density. The ECSA of the electrode was calculated from the hydrogen adsorption region during the CV using a conversion factor of 210 μC/cm^2 [8]. The CV curves were compared between the Pt nanoparticles on the Ar^+-irradiated and non-irradiated glassy carbon substrates to examine how the Ar^+ irradiation affects the ECSA and the electric double layer of the samples. Figure 2.4 shows the CV curves of the Pt nanoparticles on the glassy carbon substrates in an N_2-purged 0.1 M $HClO_4$ solution.

Table 2.1 shows the estimated ECSA values. The ECSA values were esti-

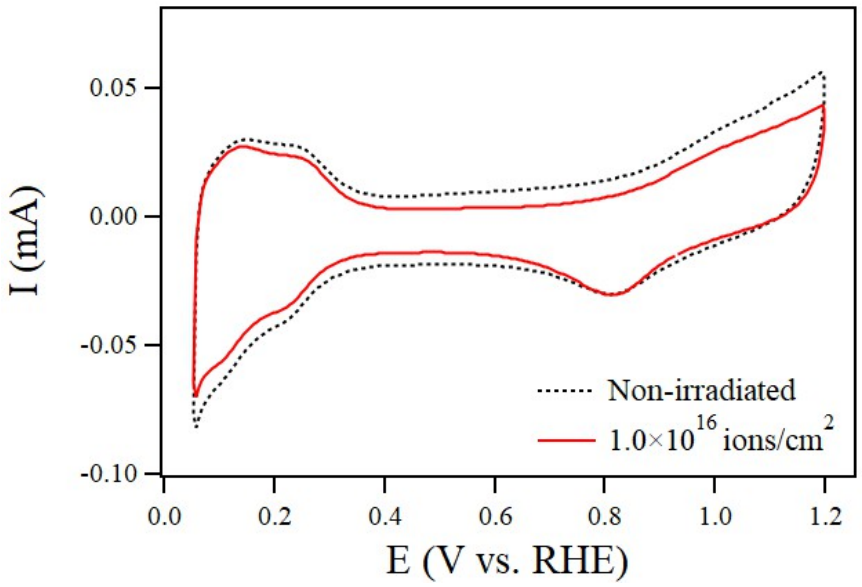

Fig. 2.4: Pt nanoparticles on the glassy carbon substrates irradiated with Ar ions as oxygen reduction catalysts. CV curves for Pt nanoparticles on the Ar^+-irradiated glassy carbon substrates in an N_2-saturated 0.1 M $HClO_4$ solution at a scan rate of 50 mV/s. This figure is obtained by modifying Fig. 1 (a) of the preprint, T. Kimata et al., ChemRxiv. Preprint. (2017).

mated to be 0.59 cm^2 and 0.57 cm^2 on the non-irradiated glassy carbon substrate and on the substrate irradiated at the highest fluence (1.0×10^{16} ions/cm^2), respectively. The ECSA and electric double layer of the samples did not change consistently as a function of the fluence. This can reasonably be explained by considering the change in the substrate roughness due to Ar^+ sputtering [15].

Table 2.1: Hydrogen adsorption charge Q and estimated ECSA

sample	Q (mC)	ECSA (cm^2)
Non-irradiated	0.124	0.59
1.0×10^{14} (ions/cm^2)	0.130	0.62
1.0×10^{15} (ions/cm^2)	0.130	0.62
1.0×10^{16} (ions/cm^2)	0.120	0.57

2.4.2 Oxygen reduction reaction activity

Figure 2.5 shows the LSV curves for the same samples in an O_2-saturated 0.1 M $HClO_4$ solution at a rotation rate of 1600 rpm. The ORR for all the samples was diffusion-controlled when the potential was less than 0.6 V/RHE and was under mixed diffusion-kinetics control in the potential region between 0.6 and 0.9 V/RHE.

Figure 2.6 shows the ORR activity of the Pt nanoparticles on the glassy carbon substrates irradiated with Ar^+ at different fluences and on the non-irradiated substrate. Figure 2.6 provides the enlarged view of the LSV curves in the range of 0.8 to 1.0 V/RHE for the Pt nanoparticles on the glassy carbon substrates irradiated with Ar^+ at fluences of 1.0×10^{14}, 1.0×10^{15}, and 1.0×10^{16} ions/cm^2 and on the non-irradiated glassy carbon substrate. Clearly, the ORR current of the Pt nanoparticles on the irradiated substrates began flowing at a more positive potential than their non-irradiated counterpart, and the onset potential was higher as the fluence increased.

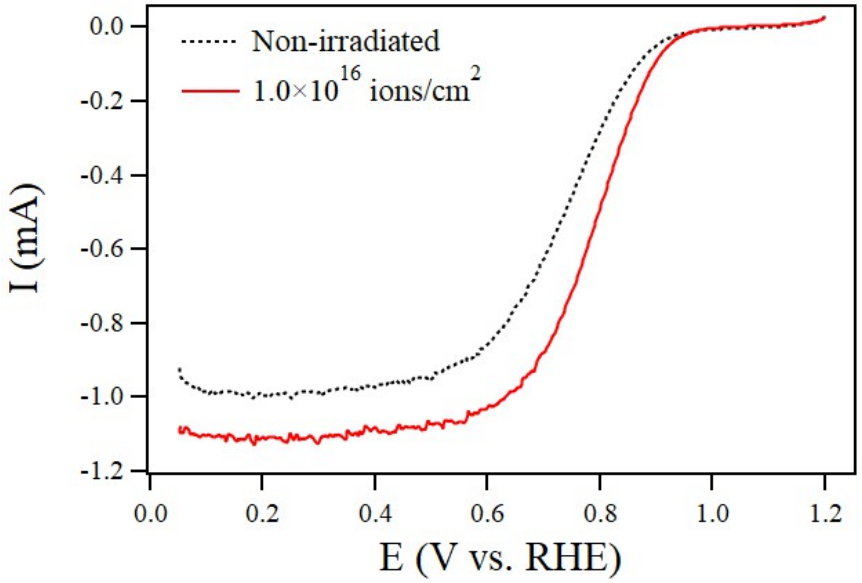

Fig. 2.5: Pt nanoparticles on the glassy carbon substrates irradiated with Ar ions as oxygen reduction catalysts. ORR polarization curves for Pt nanoparticles on the Ar^{+}-irradiated glassy carbon substrates in an O_2-saturated 0.1 M $HClO_4$ solution at a sweep rate of 20 mV/s and rotation rate of 1600 rpm. This figure is obtained by modifying Fig. 1 (b) of the preprint, T. Kimata et al., ChemRxiv. Preprint. (2017).

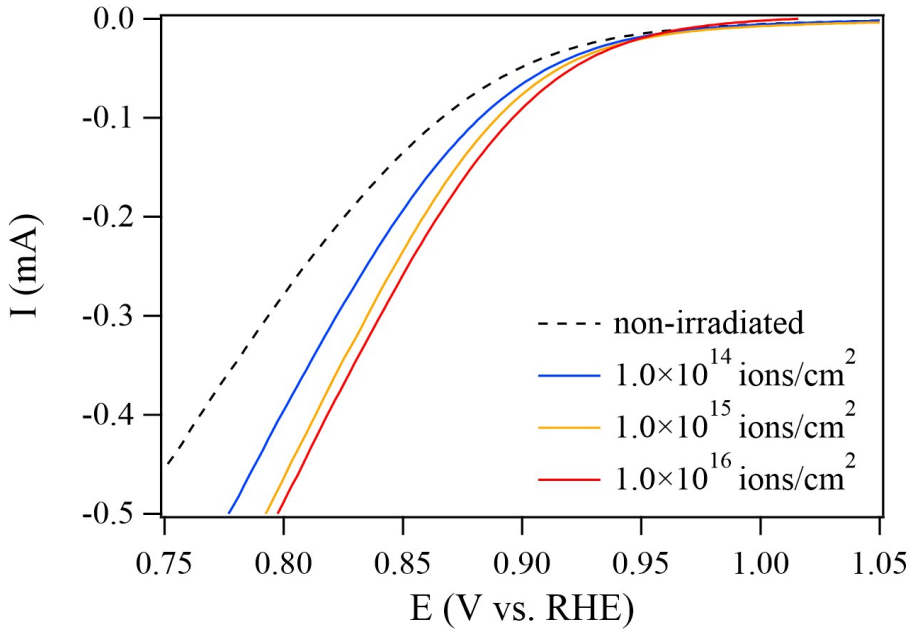

Fig. 2.6: ORR performance of all the samples. Enlarged view of the ORR polarization curves for all the samples. This figure is obtained by modifying Fig. 2 (a) of the preprint, T. Kimata et al., ChemRxiv. Preprint. (2017).

The LSV curves were recorded at four different rotation speeds, and the Koutecky-Levich plots for the ORR were straight lines. Thus, the kinetic current was derived from Koutecky-Levich theory [11], and i_k, obtained using ECSA, was represented as the Tafel slope in Figure 2.7 (left). The i_k at 0.90 and 0.85 V/RHE are shown in Table2.2. The i_k at 0.90 V/RHE were 0.115, 0.137, and 0.174 mA/cm^2 for the Pt nanoparticles on the substrates irradiated at 1.0×10^{14}, 1.0×10^{15}, and 1.0×10^{16} ions/cm^2, respectively. In other words, the SA became higher with an increase in the Ar^+ fluence and, at 1.0×10^{16} ions/cm^2, reached a maximum of twice that on the non-irradiated substrate (0.087 mA/cm^2). Strikingly, at 0.85 V/RHE, the maximum magnitude of the enhancement was $\sim$2.2 (Fig. 2.7 (right)). These results demonstrate the enhancement of the ORR activity by the Ar^+ pre-irradiation of the glassy carbon. Therefore, the Pt$-$C bonding behavior at the interface is of great interest for obtaining an insight into the origin of the higher activity.

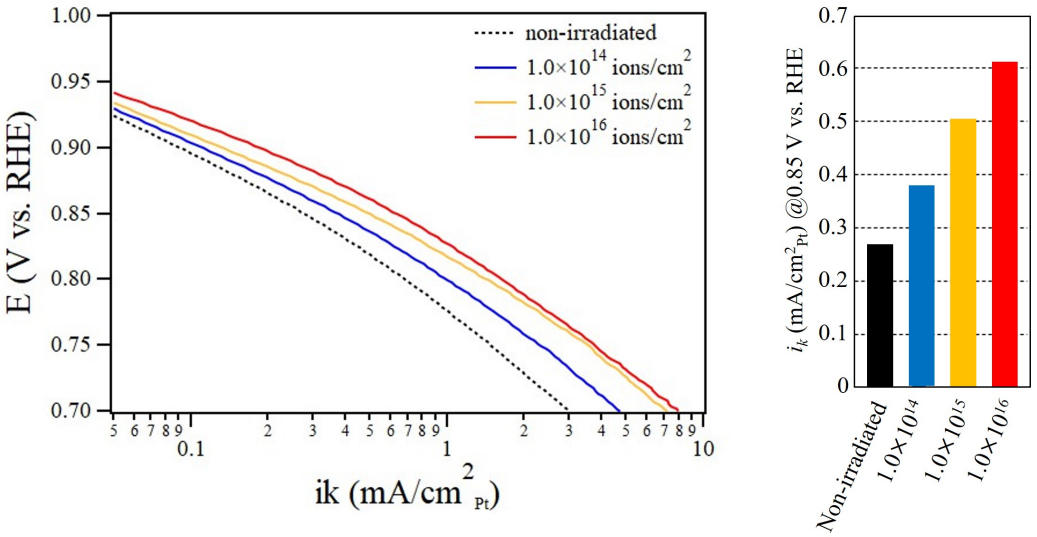

Fig. 2.7: ORR performance of all the samples. Tafel slopes derived from the mass-transport correction of the corresponding RDE data. Current densities are normalized to the ECSA of platinum within the samples. Current densities of all the samples at 0.85 V (right). This figure is obtained by modifying Fig. 2 (b) of the preprint, T. Kimata et al., ChemRxiv. Preprint. (2017).

Table 2.2: The i_k at 0.90 and 0.85 V/RHE

sample	0.90 V	0.85 V
Non-irradiated	0.0874	0.267
1.0×10^{14} (ions/cm^2)	0.115	0.387
1.0×10^{15} (ions/cm^2)	0.137	0.509
1.0×10^{16} (ions/cm^2)	0.174	0.597

2.5 Summary

In Chapter 2, the ORR activity of the Pt nanoparticles on the Ar^+-irradiated glassy carbon substrates increased proportionally to the Ar^+ fluence and, at 1.0×10^{16} ions/cm^2, reached a maximum of 2.2 times that on the non-irradiated one. This activity enhancement would be attributed to the Pt-carbon support interaction at the interface between Pt nanoparticles and glassy carbon substrates.

References

[1] C. Y. Wang. *Fundamental Models for Fuel Cell Engineering*. Chem. Rev. **104**, 4727 (2004).

[2] R. Borup, J. Meyers, B. Pivovar, Y. S. Kim, R. Mukundan, N. Garland, D. Myers, M. Wilson, F. Garzon, D. Wood, P. Zelenay, K. More, K. Stroh, T. Zawodzinski, J. Boncella, J. E. McGrath, M. Inaba, K. Miyatake, M. Hori, K. Ota, Z. Ogumi, S. Miyata, A. Nishikata, Z. Siroma, Y. Uchimoto, K. Yasuda, K. I. Kimijima, N. Iwashita. *Scientific Aspects of Polymer Electrolyte Fuel Cell Durability and Degradation*. Chem. Rev. **107**, 3904 (2007).

[3] N. M. Marković, T. J. Schmidt, V. Stamenkovic, P. N. Ross. *Oxygen Reduction Reaction on Pt and Pt Bimetallic Surfaces: A Selective Review*. Fuel Cells **1**, 105 (2001).

[4] M. K. Debe. *Electrocatalyst approaches and challenges for automotive fuel cells*. Nature **486**, 43 (2012).

[5] D. Strmcnik, M. Escudero-Escribano, K. Kodama, V. R. Stamenkovic, A. Cuesta, N. M. Marković. *Enhanced electrocatalysis of the oxygen reduction reaction based on patterning of platinum surfaces with cyanide*. Nat. Chem. **2**, 880 (2010).

[6] Denkikagakukai: Denkikagakusokutei Manyuaru Kiso-hen *(in Japanese, Electrochemical Measurement Manual: Basic)* Maruzen (2002).

[7] M. Inaba: Bunkyoku kyokusen·saikurikkuborutanmetory(1) *(in Japanese, polarization curve·cyclic voltammetry (1))*. Electrochemistry **77**, 79 (2009).

[8] S. A. Sheppard, S. A. Campbell, J. R. Smith, G. W. Lloyd, T. R. Ralph, F. C. Walsh. *Electrochemical and microscopic characterisation of platinum-coated perfluorosulfonic acid (Nafion 117) materials*. Analyst **123**, 1923 (1998).

[9] T.M. Nahir, R.A. Clark, E.F. Bowden. *Linear-Sweep Voltammetry of Irreversible Electron Transfer in Surface-Confined Species Using the Marcus Theory*. Anal. Chem. **66**, 2595 (1994).

[10] T. Ioroi, K. Yasuda: Bunkyoku kyokusen·saikurikkuborutanmetory(2) *(in Japanese, polarization curve·cyclic voltammetry (2))*. Electrochemistry **77**, 263 (2009).

[11] A.J. Bard, L.R. Faulkner. *Electrochemical Methods: Fundamental and Applications*. (Wiley, 2001).

[12] T. Hakoda, S. Yamamoto, K. Kawaguchi, T. Yamaki, T. Kobayashi, M. Yoshikawa. *Oxygen reduction activity of N-doped carbon-based films prepared by pulsed laser deposition.* Appl. Surf. Sci. **257**, 1556 (2010).

[13] Fuel Cell Commercialization Conference of Japan (FCCJ), Proposals of the development targets, research and development challenges and evaluation methods concerning PEFCs, http://fccj.jp/pdf/23_01_kt.pdf.

[14] K. J. J. Mayrhofer, D. Strmcnik, B. B. Blizanac, V. Stamenkovic, M. Arenz, N. M. Markovic. *Measurement of oxygen reduction activities via the rotating disc electrode method: From Pt model surfaces to carbon-supported high surface area catalysts.* Electrochim. Acta **53**, 3181 (2008).

[15] R. Behrisch, P. Sigmund, M. T. Robinson, H. H. Andersen, H. L. Bay, H. E. Roosendaal. *Sputtering by Particle Bombardment I*, (Springer, 1981).

Chapter 3

X-ray spectroscopy of the Pt nanoparticles on irradiated carbon substrate

3.1 Introduction

In this chapter, I describe the sample preparation method and X-ray spectroscopic analysis of the Pt nanoparticles on ion-beam irradiated carbon substrates. X-ray absorption spectroscopy (XAS) and X-ray photoelectron spectroscopy (XPS) are performed for the prepared samples. The influence of irradiated carbon substrate on the electronic structure and chemical state of the Pt nanoparticles and carbon substrate is discussed.

3.1.1 X-ray absorption spectroscopy

XAS is well known as a strong tool for the investigation of electronic structure and local structure in matter [1]. A specific structure obtained in XAS is the X-ray absorption fine structure (XAFS). By analyzing the XAFS, information can be acquired on the local structure and on the unoccupied local electronic state. Since the energy of the X-ray absorption edge is different for each element, XAS can obtain information for each target element. The most basic method of XAFS measurement is the transmission mode. The X-ray intensity before and

after irradiation into the sample is measured using an ionization chamber, and the absorbance is determined by

$$\mu t = \ln\left(\frac{I_0}{I_t}\right), \tag{3.1}$$

where μ and t are the absorbance and thickness of the sample, respectively. The I_0 and I_t are the X-ray intensity before and after irradiation into the sample. As an example, the XAFS spectrum of Pt foil is shown in Fig. 3.1.

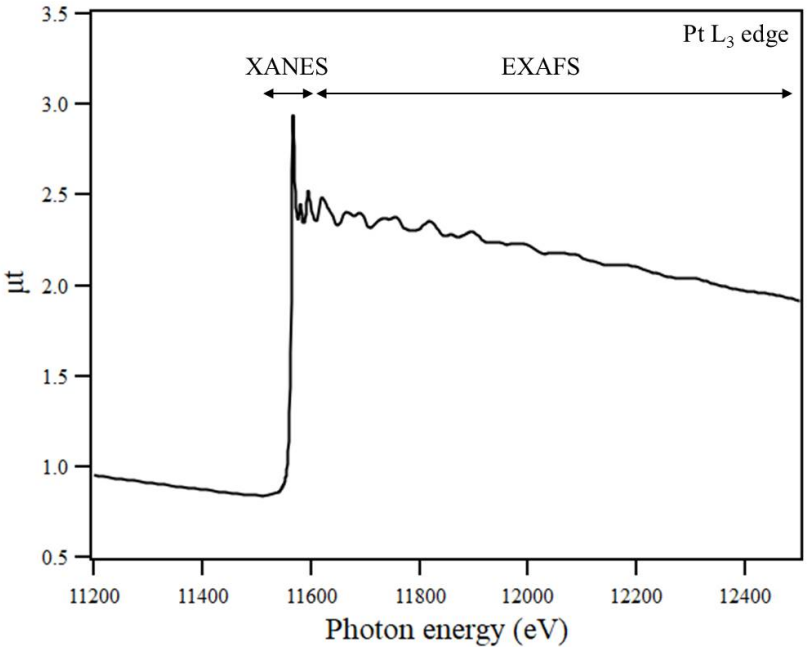

Fig. 3.1: XAS spectrum of Pt L_3-edge for Pt foil.

When an assembly of atoms is irradiated by X rays, it will absorb part of the incoming photons. At a certain energy, a sharp rise in the absorption will be observed. This sharp rise in absorption is called the absorption edge, and the edge seen in Fig. 3.1 is the Pt L_3 edge. The structure around absorption edge is X-ray absorption near edge structure (XANES). XANES contains information about the electronic state of the X-ray absorbing atom and the local structure surrounding it. Extended X-ray absorption fine structure (EXAFS) is an oscillatory structure that appears above the X-ray absorption edge and extends typically up to $\sim$1000 eV; the elemental species, coordination number,

and bond length around the absorbing atoms can be investigated by analyzing EXAFS.

In addition, the experiment is usually performed at synchrotron radiation facilities, which provide intense and tunable X-ray beams.

3.1.2 X-ray photoelectron spectroscopy

In X-ray photoelectron spectroscopy (XPS), the surface of samples is irradiated with soft X rays in a vacuum chamber and the energy of photoelectrons emitted from the surface is measured. The energy of photoelectrons emitted in a vacuum is lower than that of irradiated X-rays by the binding energy of the electrons on the atomic orbits in the sample. The binding energy of the electron $E_{binding}$ is obtained by

$$E_{binding} = E_{photon} - E_{kinetic} - \phi, \tag{3.2}$$

where E_{photon} is the energy of the X-ray photons being used, $E_{kinetic}$ is the kinetic energy of the electron as measured by the energy analyzer and ϕ is the work function dependent on both the XPS spectrometer and the target material. The Al Kα or Mg Kα X-rays are commonly used as the source of incident X-ray. The ϕ is an adjustable instrumental correction factor that accounts for the few eV of kinetic energy given up by the photoelectron as it becomes absorbed by the instrument's detector. Furthermore, the elements and its proportions can be identified.

The binding energy is unique to each element and is known to vary by a few eV depending on the chemical state of the atom. This variation is called a chemical shift, and the amount of variation is determined by the bonding with neighboring atoms and the degree of electronegativity. Therefore, it is possible to analyze the chemical state by accurately obtaining the bonding energy. Since the peak area of each element is proportional to its amount, the concentration

can also be determined quantitatively. XPS is used as a tool for surface analysis because of the measurement range from the surface to a few nm depth.

3.2 Sample preparation

At first, glassy carbon is used as carbon substrate. Unpolished 1-mm-thick glassy carbon substrates were obtained from Tokai Carbon Co., Ltd., Japan, and cut into 1 cm$\times$1 cm samples. Ar^+ irradiation is performed at an energy of 380 keV and the fluences between 1.0×10^{14} and 1.0×10^{16} ions/cm^2 using the ion implanter. The irradiated glassy carbon substrates are heated at 400°C in an N_2 atmosphere for 1 h in order to remove water-related contamination. Pt nanoparticles are then deposited on this substrate by radio-frequency (rf) magnetron sputtering at room temperature. The sputtering time and the plasma output are 60 s and 20 W, respectively, for all the samples.

The ion-beam irradiation and the preparation and characterization of Pt nanoparticles are described below.

3.2.1 Ion-beam irradiation

Ion-beam irradiation was performed by the ion implanter at the Takasaki Ion Accelerators for Advanced Radiation Application (TIARA) facility of the Takasaki Advanced Radiation Research Institute (TARRI), National Institutes for Quantum and Radiological Science and Technology (QST), Japan (Fig. 3.2) [2].

The role of ion beam irradiation in this study is to introduce the lattice defects into the carbon substrate. Therefore, Ar^+ irradiation was chosen because it is not necessary to consider the interaction between the implantation element and the host materials. The 380 keV which is the maximum energy of the ion implanter was adopted.

Fig. 3.2: Ion implanter at the TIARA facility.

In principle, the fluence is obtained by integrating the beam current at the sample position. In this study, the beam current values were measured using a Faraday cup.

Using the current values obtained by using the Faraday cup, the beam flux χ is calculated by

$$\chi(ions/s/cm^2) = \frac{100 \times 10^{-9}(A)}{1(valence)} \cdot \frac{1}{1.6 \times 10^{-19}} \cdot \frac{1}{1(cm^2)} = 6.25 \times 10^{11} \tag{3.3}$$

where current, valence, and irradiation area are set to 100 nA, 1, and 1 cm^2, respectively. Therefore, when the sample is irradiated at the fluence of 1.0×10^{15} ions/cm^2, the irradiation time is obtained by

$$t(s) = \frac{1.0 \times 10^{15}}{6.25 \times 10^{11}} = 1600(s). \tag{3.4}$$

Next, the LET of 380 keV Ar^+ irradiated on the glassy carbon substrate is simulated using the SRIM and transport of ion in matter (TRIM) codes [3]. The density of glassy carbon used in the simulation was 1.51 g/cm^3.

Figure 3.3 shows the result of the simulation. As shown in Fig. 3.3 (a), the LET of Ar^+-irradiated into glassy carbon was similar to that into graphite. The vacancies increased slowly from the glassy carbon surface to about 400 nm

depth, indicating that the displacement near the surface was not significantly large (Fig. 3.3 (b)). In this chapter, the modification of the sample surface is controlled by the fluence of 380 keV Ar^+ irradiation.

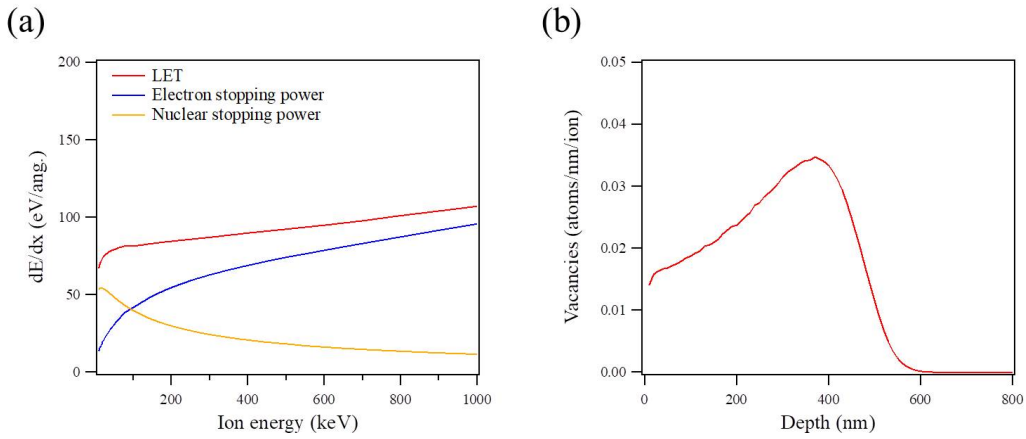

Fig. 3.3: (a) LET when the glassy carbon substrate is irradiated with Ar^+. (b) Vacancy when the glassy carbon substrate is irradiated with 380 keV Ar^+.

3.2.2 Preparation of Pt nanoparticles

The rf magnetron sputtering method was used for the preparation of Pt nanoparticles. The sputtering method is a technique for forming nanoparticles and thin films; high energy particles impinge on the target material which is the base material for nanoparticles or thin films, dislodging the atoms of the target material and depositing them on the substrate. The rf magnetron sputtering method is a sputtering method in which high-frequency waves are applied between electrodes to increase the density of the plasma by utilizing magnets placed directly under the target. In addition to the ease of preparation of nanoparticles, the sputtering method has been recognized as a model catalyst preparation method due to the advantage of being able to adhere to the substrate without coating with an ionomer.

The appearance of the rf magnetron sputtering system used in this study is shown in Fig. 3.4 (a) and the sample holder is shown in Fig. 3.4 (b). The

plasma output, frequency, and sputtering time were 20 W, 13.56 MHz, and 60 s, respectively.

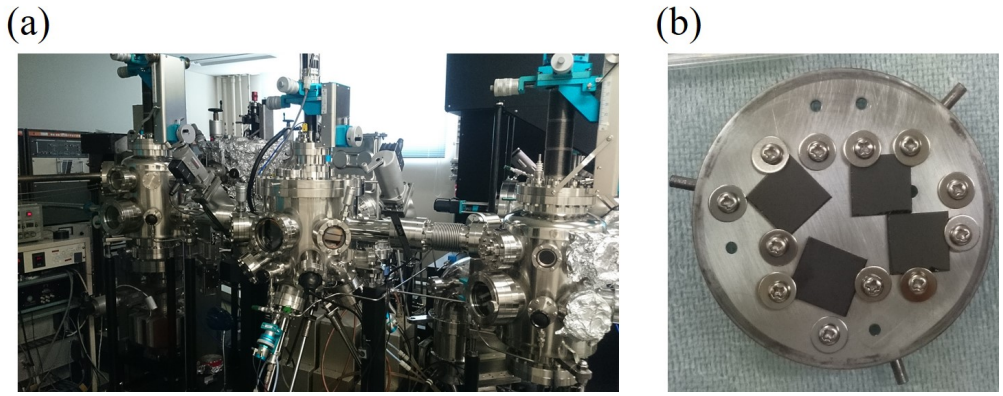

Fig. 3.4: The (a) appearance of the rf magnetron sputtering system and (b) sample holder.

3.2.3 Characterization

The Pt nanoparticles on the irradiated glassy carbon substrate were characterized by field-emission scanning electron microscopy (FE-SEM), and the Pt nanoparticles on a pristine substrate were analyzed by Rutherford backscattering spectrometry (RBS) [4]. An RBS spectrum was obtained using the single-ended accelerator at TIARA. The areal concentration of the deposited Pt atoms was estimated by using SIMNRA, a simulation program for RBS spectra [5]. The Pt nanoparticles were directly observed using an FE-SEM (JSM-6700F, JEOL Ltd., Japan); the result was compared to that from observations by transmission electron microscopy (TEM) (JEM-2100F, JEOL Ltd., Japan). Figure 3.5 shows the (a) FE-SEM and (b) TEM used in this study.

3.2.3.1 Rutherford backscattering spectrometry

An RBS spectrum was obtained using 2 MeV He^+ from the single-ended accelerator with normal incidence and a scattering angle of 165° (Fig. 3.6).

Figure 3.7 shows the RBS spectrum from the Pt nanoparticles on a pristine

(a) (b)

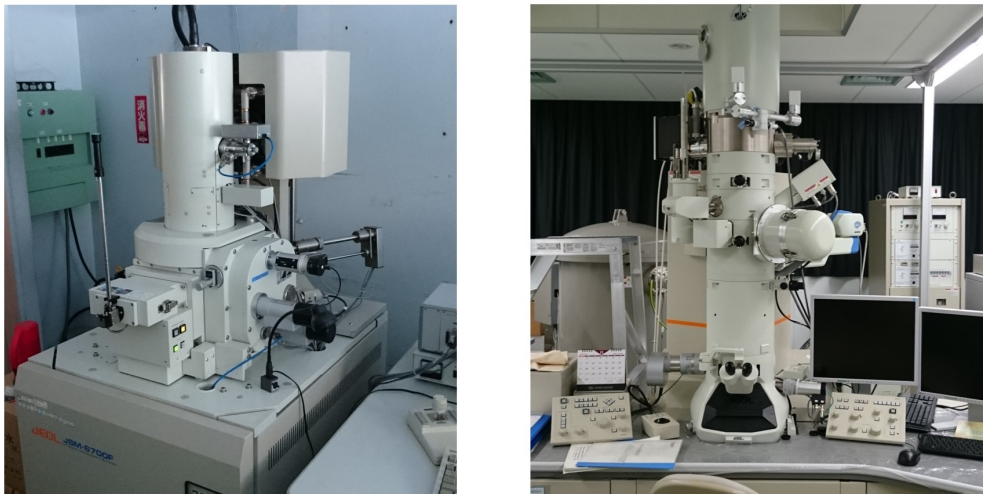

Fig. 3.5: The appearance of (a) FE-SEM and (b) TEM.

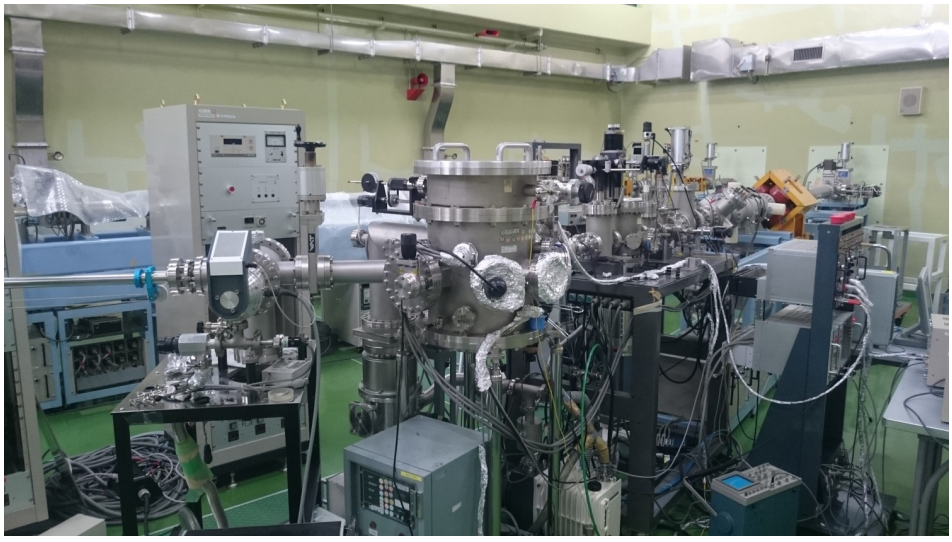

Fig. 3.6: The single-ended accelerator at TIARA.

glassy carbon substrate. Whereas an intense peak at the highest energy corresponds to the Pt nanoparticles, in contrast, the carbon in the glassy carbon substrate exhibited a continuous spectrum on the low energy side. The carbon peak emerged from the vicinity of 0.51 MeV corresponding to a k-factor of 0.253 [6], likely confirming the partial exposure of the glassy carbon surface or incomplete coverage with Pt nanoparticles. According to the analysis of the RBS spectrum using the SIMNRA software, the areal atomic concentration of the deposited Pt was 1.76×10^{16} atoms/cm^2. Therefore, if the Pt atoms were assumed to form a single crystal, their areal mass concentration and effective thickness could be calculated using the atomic weight (195.1 g/mol) and the mass density (21.45 g/cm^3) of Pt; the results were 5.70×10^{-6} g/cm^2 and 2.66 nm, respectively. In principle, these quantitative data would be invariant between the pristine and Ar^+-irradiated glassy carbon substrates because they naturally correspond to the net amount of Pt species arriving at the surface of the substrate during the sputtering.

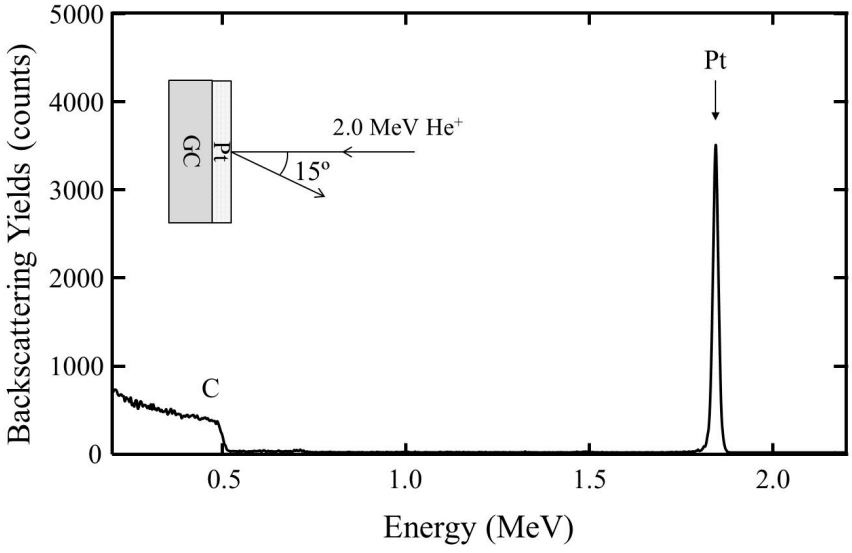

Fig. 3.7: RBS spectrum of the Pt nanoparticle layer on the non-irradiated glassy carbon substrate, measured with 2.0 MeV He^+ at 165°. This figure is obtained by modifying Fig. 2 of the paper, T. Kimata et al., Surf. Coat. Technol. 306, 123 (2016).

3.2.3.2 Microscopic Observation

The Pt nanoparticles on the irradiated glassy carbon substrate were investigated by using FE-SEM. The obtained images represented many isolated bright spots with diameters of 5-10nm may be corresponding to the deposited Pt nanoparticles (Fig. 3.8 (a)). However, their average diameter could not be precisely estimated because the bare, unpolished substrate originally had a rather rough surface and mostly exhibited the identical images.

Instead, a TEM image of the Pt nanoparticles was acquired to examine their size and distribution. Specimen preparation was performed by sputter deposition directly on a TEM grid under the same conditions. Actually, the number density of the deposited nanoparticles was too high to individually see them in the bright-field image; therefore, the dark-field image was obtained as shown in Fig. 3.8 (b). The Pt nanoparticles were clearly observed as black circles throughout the entire image. Their average diameter was about 5 nm, which is comparable to that of the Pt nanoparticles which were prepared by the similar sputtering method [7].

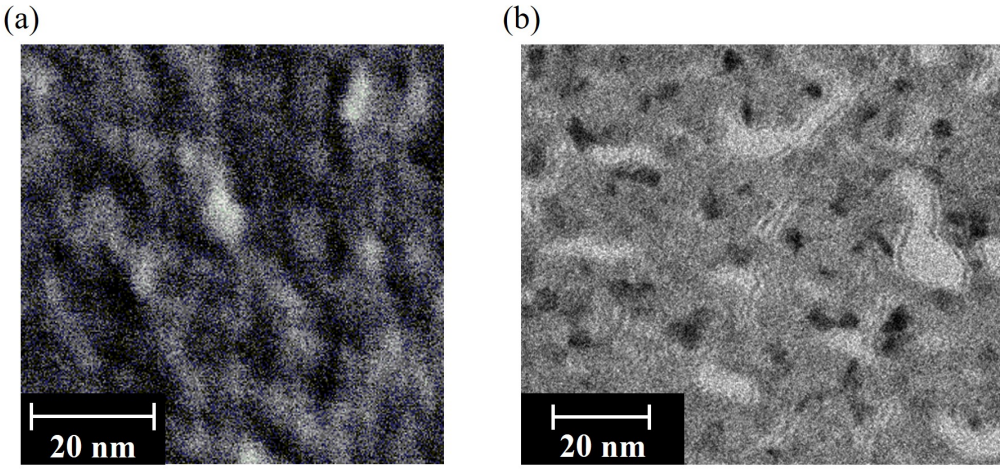

Fig. 3.8: (a) The FE-SEM image of the deposited Pt nanoparticles on a glassy carbon substrate, and (b) the TEM image of the deposited Pt nanoparticles on a grid mesh for electron microscopy. The figure (b) is obtained from Fig. 3 of the paper, T. Kimata et al., Surf. Coat. Technol. 306, 123 (2016).

The 5-nm diameter Pt nanoparticle weighed 1.40×10^{-18} g, assuming that it was perfectly spherical. The number of Pt nanoparticles per unit area was calculated to be 4.06×10^{12} particles/cm^2. If the 5-nm nanoparticles of this number were arranged on the 1-cm^2 glassy carbon surface, the coverage would be nearly 80%. In a practical sense, however, the surface roughness of the original unpolished glassy carbon substrate is significant (a few micrometers, according to the manufacturer [8]), and the actual coverage value would be much lower than the above-predicted one. Thus, almost all of the deposited Pt nanoparticles would be in contact with the glassy carbon surface.

3.3 XAFS and XPS studies of the Pt nanoparticles on irradiated glassy carbon substrate

3.3.1 XAFS measurement

The interfacial structure between the Pt nanoparticles and glassy carbon substrate was investigated by XAFS measurements [9]. The XAFS measurements of the Pt M_3-edge were carried out on the BL-27A of the Photon Factory in the High Energy Accelerator Research Organization (KEK-PF) [10] in the total electron yield (TEY) mode to conduct surface-sensitive measurements in an ultrahigh vacuum chamber at room temperature with a base pressure of about 1.0×10^{-7} Pa. The beamline is shown in Fig. 3.9. The spectra were processed with normalization and background subtraction using the program IFEFFIT [11]. The XAFS spectra of the Pt L_3-edge were obtained at the BL14B1 of SPring-8 [12] in the transmission mode at room temperature (Fig. 3.10). The XANES data at the Pt M_3-edge and the EXAFS data at the Pt L_3-edge were analyzed to investigate the electronic structure of the Pt 5d band and the local bonding structure around the Pt atoms, respectively. For the XANES analysis, the X-ray absorption at the Pt M_3-edge was investigated because the Pt nanopar-

ticles were deposited only on the surface of the samples and lower X-ray energy is suitable for the surface analysis.

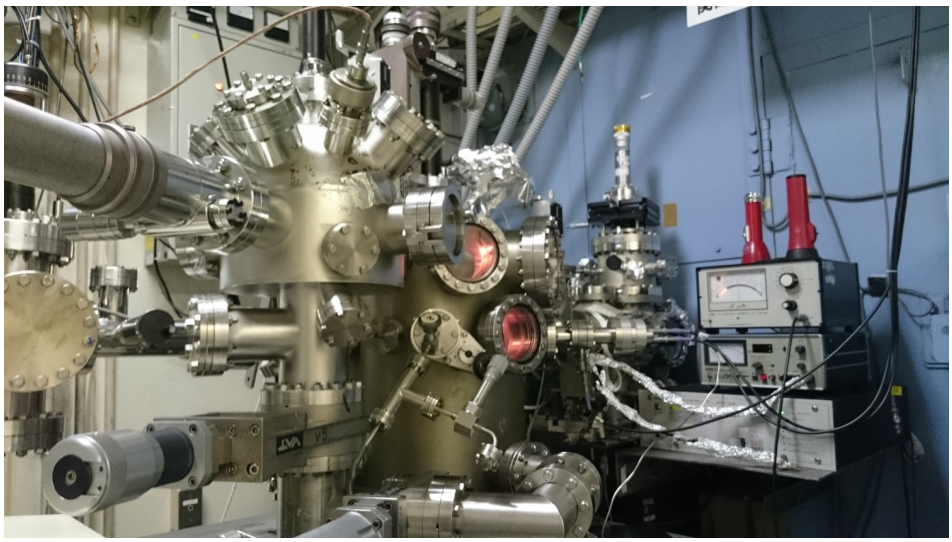

Fig. 3.9: The measurement chamber of the BL-27A of the KEK-PF.

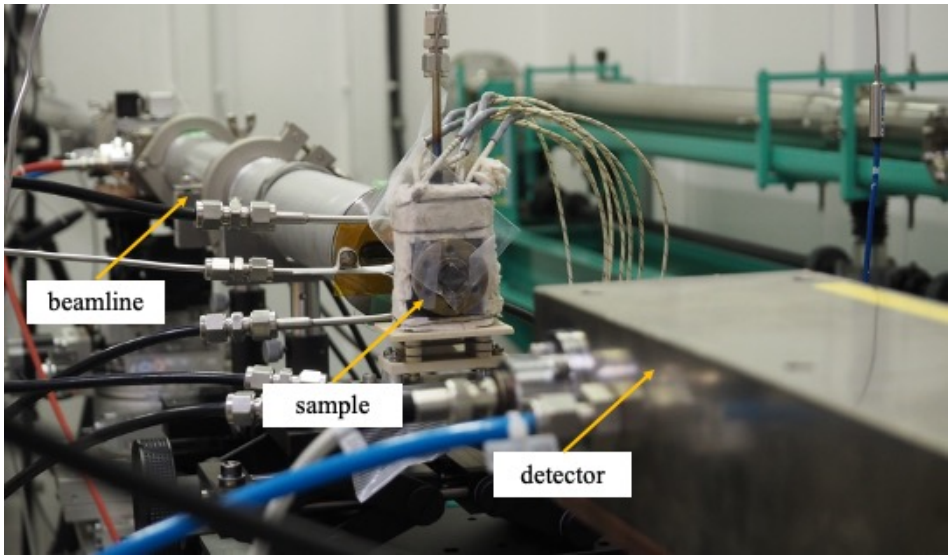

Fig. 3.10: The measurement port of the BL14B1 of SPring-8.

3.3.1.1 Pt M_3-edge XANES spectra

Pt M_3-edge XANES spectra were measured in the TEY mode to examine the changes in the electronic structure of the Pt 5d band. They are shown in Figure 3.11 after normalization and background subtraction. The whiteline in-

tensity of the Pt nanoparticles was reduced on the Ar^+-irradiated substrates, and this reduction became significant as the irradiation fluence increased. These results indicate that the density of the unoccupied Pt 5d states decreased on the glassy carbon substrates irradiated with Ar^+ due to the suppression of Pt oxidation [13]. In some papers about the relationship between the oxidation and ORR activity, the oxygen-containing surface layer caused slower kinetics [14,15], because desorption of O and OH would be the rate-limiting steps for the ORR at high potentials on the Pt nanoparticles [16]. Thus, we consider that the improvement of the ORR activity by the Ar^+ irradiation resulted from the suppressed oxidation.

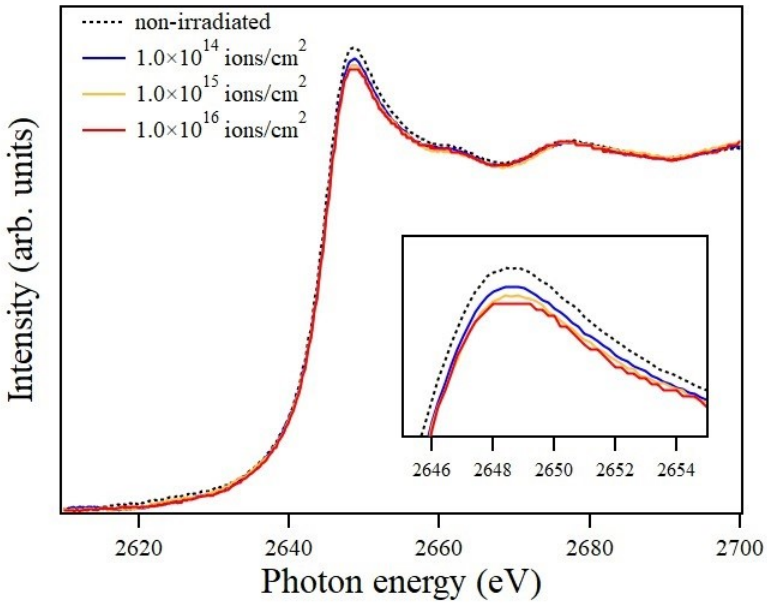

Fig. 3.11: XAFS spectra of Pt nanoparticles on the Ar^+-irradiated glassy carbon substrates. The normalized XAFS spectra of the Pt M_3-edge measured in the TEY mode using the BL-27A of the KEK-PF. The inset shows an enlarged view of the whiteline peaks. This figure is obtained by modifying Fig. 3 (a) of the preprint, T. Kimata et al., ChemRxiv. Preprint. (2017).

3.3.1.2 Pt L_3-edge EXAFS spectra

Pt L_3-edge XAFS spectra were measured in the transmission mode for the analysis of EXAFS. In order to increase the density of Pt in samples, the samples for the Pt L_3-edge XAFS measurements were prepared as shown in Figure 3.12.

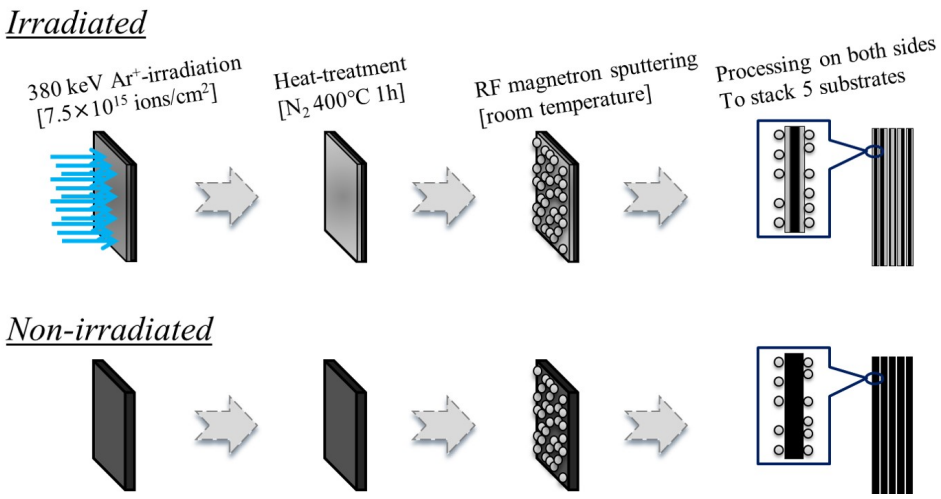

Fig. 3.12: Sample preparation schematic for the Pt L_3-edge XAFS measurements at SPring-8. The glassy carbon substrates were irradiated with 380 keV Ar^+ at the fluence of 7.5×10^{15} ions/cm^2, and heated at 400°C in an N_2 atmosphere for 1 h. Pt nenoparticles were then deposited on the surface by rf magnetron sputtering for 60 s. This processing were treated both side of glassy carbon substrates, 5 substrates were stacked. This figure is obtained by modifying Fig. S6 of the preprint, T. Kimata et al., ChemRxiv. Preprint (2017).

The analysis of the EXAFS data can support the interpretation in the previous paragraph from the perspective of the local bonding structure. Figure 3.13 shows the Pt L_3-edge XAFS spectra in the transmission mode. The whiteline intensity was lower, which is similar to Fig. 3.11.

The radial distribution function was obtained from the EXAFS oscillation in Figure 3.13, as shown in Fig. 3.14. Fourier transformation for the EXAFS spectra and a fitting procedure were performed in the R-space with Δk = 3.0−9.5 Å^{-1} and ΔR = 1.3−3.3 Å, respectively. The backward amplitude and phase shift required for the least-squares fitting of the Fourier transformed EXAFS spectra were obtained from the FEFF 6 program [17]. Figure 3.14 (a)

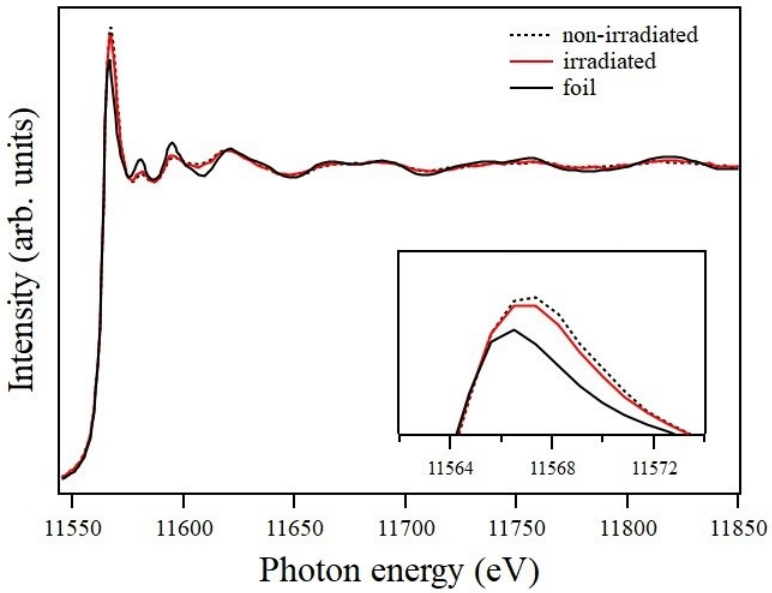

Fig. 3.13: XAFS spectra of Pt nanoparticles on the Ar^+-irradiated glassy carbon substrates. The normalized XAFS spectra of the Pt L_3-edge measured in the transmission mode at the BL14B1 of SPring-8. This figure is obtained by modifying Fig. 3 (b) of the paper, T. Kimata et al., ChemRxiv. Preprint. (2017).

shows k^2-weighted EXAFS spectra of the Pt-foil and the Pt nanoparticles on the glassy carbon substrate irradiated with Ar^+ at a fluence of 7.5×10^{15} ions/cm^2 and on the non-irradiated substrate. Figure 3.14 (b) was obtained by Fourier transformation of the EXAFS spectra (3.0$<k<$9.5 Å^{-1}, k^2). Least-squares fitting with Pt$-$Pt and Pt$-$O nearest-neighbor coordination shells in the R space (1.3$<R<$3.3 Å) was treated (Figure 3.14 (c) and 3.14 (d)).

The detailed EXAFS parameters, such as the coordination number, bond length, and Debye-Waller factor, are listed in Table 3.1. In the Fourier transformation of the Pt foil, the coordination number was set to 12 as a reference. The Pt nanoparticles on the irradiated substrate exhibited a lower Pt$-$O coordination number than those on the non-irradiated substrate. The Pt$-$Pt bond length of the Pt nanoparticles on the irradiated substrate was shorter than on the non-irradiated substrate, even after errors were considered.

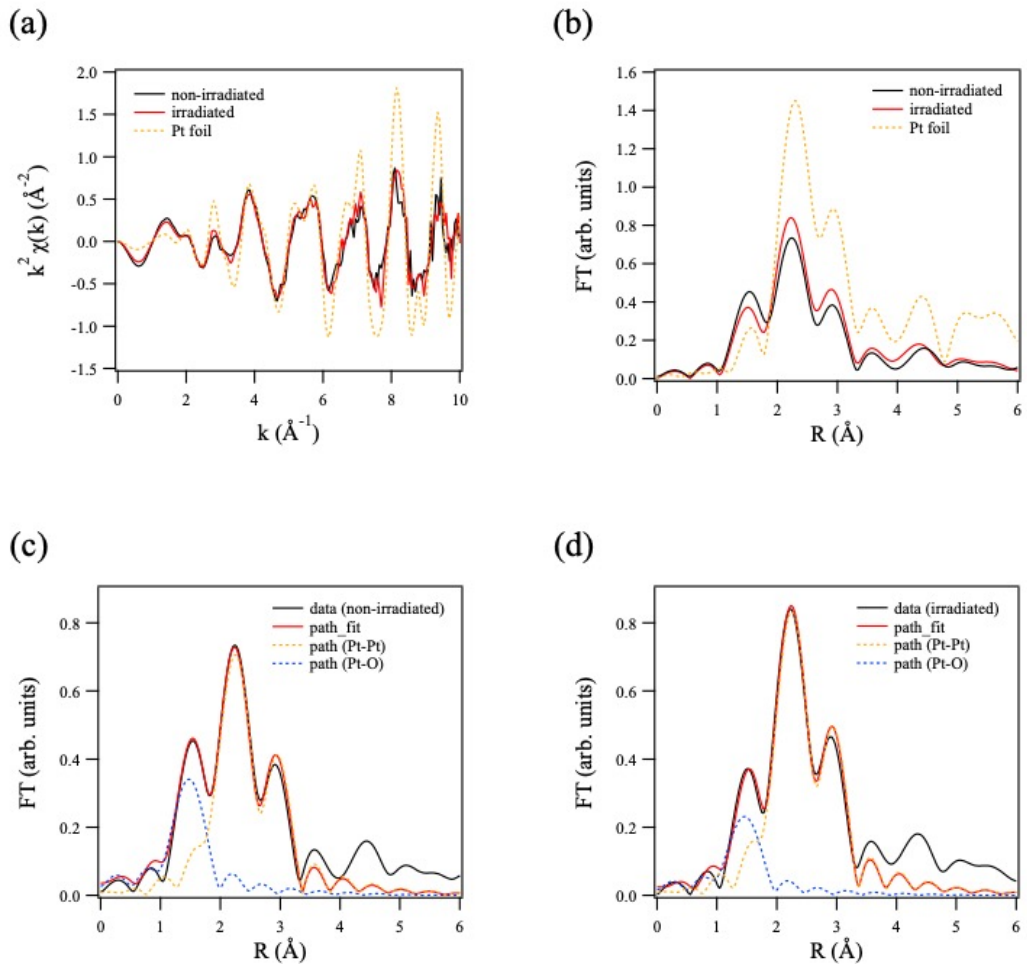

Fig. 3.14: (a) k^2-weighted EXAFS spectra, (b-d) Fourier transform of the EXAFS spectra. These figures are obtained by modifying Fig. S2 of the preprint, T. Kimata et al., ChemRxiv. Preprint. (2017).

Table 3.1: The structural parameters obtained from the analysis of the Pt L_3-edge EXAFS spectra. This table is obtained from Table. S3 of the preprint, T. Kimata et al., ChemRxiv. Preprint. (2017).

sample	path	Coordination Number	Bond length (Å)	D-W factor (Å^2)	R-factor (%)
Pt-foil	Pt-Pt	12	2.7572±0.0063	0.0031	0.0025
Non-irradiated	Pt-Pt	10.293	2.7508±0.0026	0.0088	0.0083
	Pt-O	2.041	1.9231±0.0085	0.0009	
Irradiated	Pt-Pt	10.799	2.7437±0.0031	0.0076	0.0098
	Pt-O	1.289	1.9093±0.0175	0.0003	

This table indicates the following two important characteristics: (i) the Pt nanoparticles on the irradiated substrate exhibited a lower Pt−O coordination number than those on the non-irradiated glassy carbon surface and (ii) the slight shortening of the Pt−Pt bond length was caused by the Ar^+ irradiation. Regarding the second characteristic, the shortened Pt−Pt bond length was reported to weaken the bond strength between O and Pt [18]. Therefore, these two findings from the EXAFS analysis are consistent with the suppressed oxidation discussed above. The shorter Pt−Pt bond length would originate from the structure of the Pt/glassy carbon interface involving the Pt−C bonding.

As an additional experiment, the EXAFS measurements were also carried out for smaller Pt nanoparticles, hoping that the interfacial effect would be more pronounced [19]. The sputtering time for Pt deposition was reduced to 10 s. Similar to the results of 60 s deposition, the Pt−Pt coordination number was higher and the Pt−Pt bond length was shorter in the Pt nanoparticles on the Ar^+-irradiated glassy carbon substrate.

3.3.2 XPS measurement

The chemical state of the Pt nanoparticles on Ar^+-irradiated glassy carbon substrates was investigated by XPS measurements [4]. XPS measurements were performed using PHI 5000 Versa Probe (ULVAC-PHI, Inc., Japan) with an Al Kα (1486.6 eV) X-ray as the light source (Fig. 3.15). High-resolution Pt 4f and C 1s spectra were taken with a pass energy of 23.5 eV with a 0.1 eV step and averaged for 20 and 40 scans, respectively. A 2 keV Ar-ion sputtering gun was used for the cleaning surface. The sputtering duration was set to 5 s, which corresponded to a sputter depth of less than 1 nm and, therefore, would negligibly be short.

The Pt nanoparticles on the Ar^+-irradiated glassy carbon substrates were analyzed by Pt 4f and C 1s XPS spectra. Figure 3.16 shows a Pt 4f spectrum for

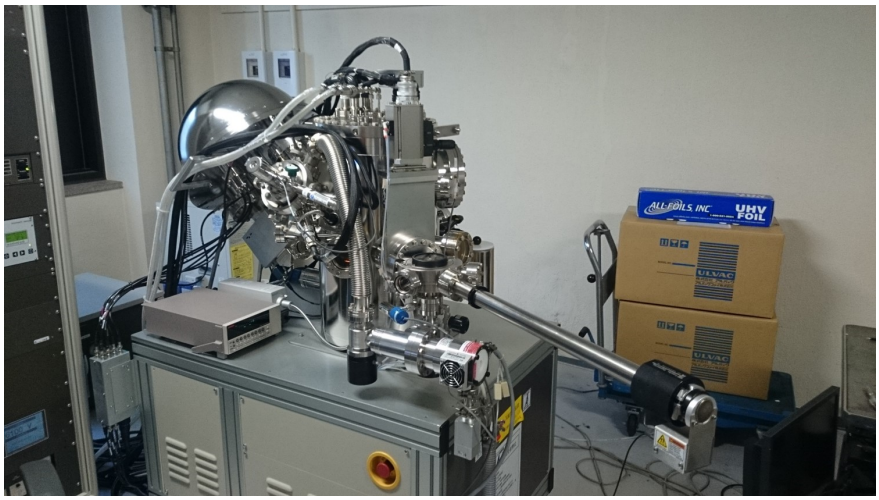

Fig. 3.15: The PHI 5000 Versa Probe used in the XPS measurements.

the Pt nanoparticles on the Ar^+-irradiated glassy carbon surface, compared to the spectra for the Pt nanoparticles on the non-irradiated one and a Pt foil as the standard sample. These spectra are displayed after conditioning the rawdata through the removal of background, normalization of intensity, and alignment.

Generally, a Pt 4f spectrum has two peaks because the energy level of a Pt 4f orbital is split into the $4f_{7/2}$ and $4f_{5/2}$; the high-intensity Pt $4f_{7/2}$ peak was used for the spectrum analysis. With or without the Ar^+ irradiation, the Pt $4f_{7/2}$ peak was observed at a binding energy of 71.0 eV, and its main component would be metallic Pt (0) [20–22]. It should be noted here that the Pt $4f_{7/2}$ peak in the spectra of the Pt nanoparticles on glassy carbon substrates were broader on the high energy side than that in Pt foil. The higher oxidation states of Pt, such as Pt (IV) (PtO_2), appeared in this energy range [20, 22]. On the other hand, the Pt-carbon support interactions were also found to give rise to a similar Pt $4f_{7/2}$ signal; Gupta *et al.* identified the interaction between the Pt nanoparticles and the graphitic mesoporous carbon by the peak shift to 72.1 eV [23]. These suggest that two possibilities for the observed broadening have to be considered in our case; it is either the oxidation state of Pt or the Pt−C bonding. Indeed, the XAFS of Pt M_3- and L_3-edges does not directly distinguish between oxidation

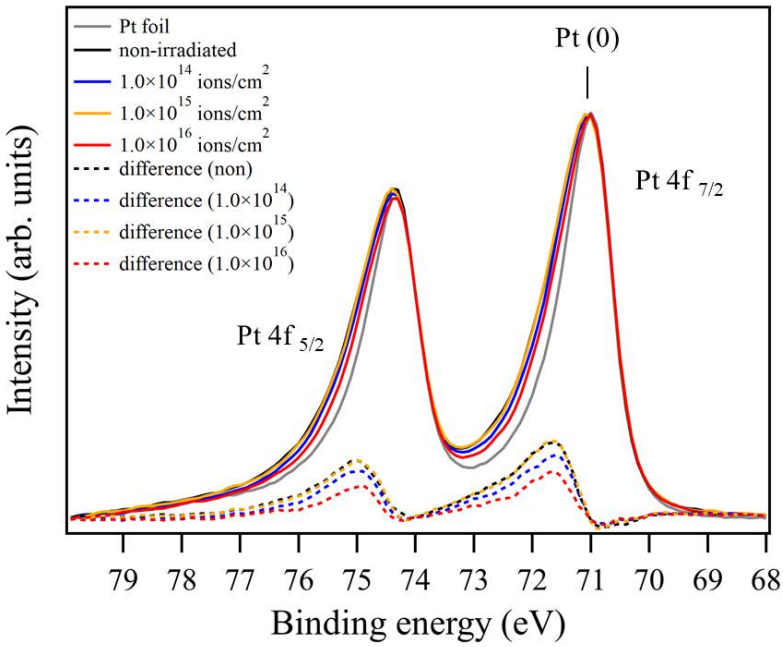

Fig. 3.16: Pt 4f XPS spectra of the Pt nanoparticles on the glassy carbon substrate pre-irradiated by 380 keV Ar^+ at a fluence of 1.0×10^{14}, 1.0×10^{15} and 1.0×10^{16} ions/cm^2, the Pt nanoparticles on the non-irradiated glassy carbon substrate, and the standard Pt foil. The dash lines are difference spectra between the prepared samples and the Pt foil. This figure is obtained by modifying Fig. 4 of the paper, T. Kimata et al., Surf. Coat. Technol. 306, 123 (2016).

state of Pt and Pt−C interactions. As described below, the analysis of the C 1s spectra would clarify the origin of the present finding, that is, the oxidation of Pt or interfacial interactions.

Figure 3.17 shows the C 1s spectrum for the Pt nanoparticles on the glassy carbon surface irradiated at 1.0×10^{14}, 1.0×10^{15} and 1.0×10^{16} ions/cm^2 compared to the result for the Pt nanoparticles on the non-irradiated one.

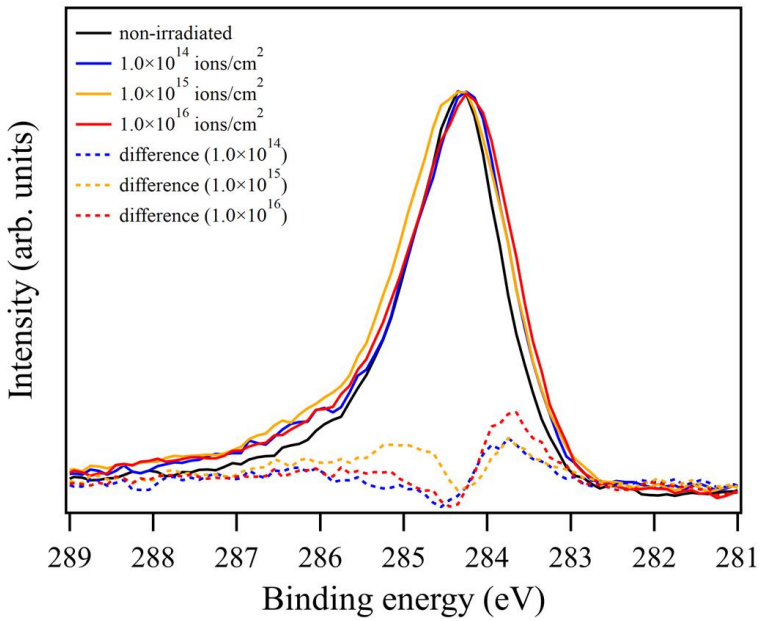

Fig. 3.17: C 1s XPS spectra of the Pt nanoparticles on the glassy carbon substrate pre-irradiated by 380 keV Ar^+ at a fluence of 1.0×10^{14}, 1.0×10^{15} and 1.0×10^{16} ions/cm^2, and the Pt nanoparticles on the non-irradiated one. The dash lines are difference spectra between the irradiated and non-irradiated samples. This figure is obtained by modifying Fig. 5 of the paper, T. Kimata et al., Surf. Coat. Technol. 306, 123 (2016).

The main component of the peak at 284.3 eV was the C 1s peak of graphite in the glassy carbon [24]. Spectra of the Pt nanoparticles on irradiated glassy carbon substrates exhibited a wider peak than that on non-irradiated one; most interestingly, a small bump on the low binding energy side was seen in the spectra of the Pt nanoparticles on irradiated glassy carbon substrates. As indicated by the difference spectra between the irradiated and non-irradiated samples (Fig. 3.17), this would be attributed to the Pt−C binding interactions (283.6 eV [25])

at the interface between the Pt nanoparticle and the glassy carbon substrates.

As a result, the broadening of the Pt $4f_{7/2}$ peak for the spectrum of the non-irradiated sample in Fig. 3.16 can be attributed to the oxidation of Pt, the Pt $4f_{7/2}$ peak for spectra of irradiated samples would indicate to suppress oxidation of Pt. This result is consistent with the XAFS results. The bombardment with 380 keV Ar^+ modified the glassy carbon surface, and would boost the formation of the Pt−C interactions with charge transfer from Pt to C at the Pt-carbon support interface.

3.4 Changes in electronic structure of carbon supports for Pt nanoparticles by ion-beam irradiation

The electronic structure of carbon support near the interface between the Pt nanoparticles and the carbon support is investigated by surface sensitive XAS measurements at the C K-edge in order to elucidate the influence of the introduction of vacancies on the carbon support on the Pt−C interaction [26].

3.4.1 Experimental setup

Highly ordered pyrolytic graphite (HOPG) substrates with a size of 1×1 cm^2 and a thickness of 1 mm were obtained from ALLIANCE Biosystems Co., Ltd., and used for the carbon support. HOPG was used for the substrates to elucidate the changes in the electronic structure upon dissolving orbital components (σ and π bonds), as mentioned below. Ar^+ irradiation was performed at 380 keV and a fluence of 1.0×10^{14} ions/cm^2 using the ion implanter at TIARA. Pt nanoparticles were deposited on the irradiated and non-irradiated HOPG substrates by radio frequency magnetron sputtering for 20 s at room temperature. The sizes of the Pt nanoparticles were estimated by TEM and found to be 3.0 nm and 2.7 nm for the irradiated HOPG and the non-irradiated HOPG, respectively.

The XANES spectra were measured using the BL-8 at the SR center in Ritsumeikan University. For well-known systems, XANES measurements using E-vector polarized light can probe the charge orientations of different excited electronic structures [27,28]. For HOPG, the C−C σ^* and C−C π^* components in the XANES spectra can be resolved by selecting the E-vector direction. In our measurements, we used linear polarized light with the E-vector and exposed the sample at 90° and 30° from the vertical direction of the sample plane [26]. The XANES spectra with incident angles of 30° are used in this thesis. The base pressure of the measurement chamber was less than 2.0×10^{-8} Pa. In order to perform the sensitive surface measurements, we applied a retarding potential of 150 V to the detector.

3.4.2 Results and discussion

Figure 3.18 (a) shows the XANES spectra of irradiated and non-irradiated HOPG substrates with incident angles of 30°, normalized by the intensity at 300 eV. For the non-irradiated HOPG (black line), four main peaks can be observed: π^* (at ∼285 eV), C−H* or C=O* (∼288 eV), σ^* (291.5 eV), and σ_1 (292.5 eV). These peaks have been identified in previous research [28, 29]. All peaks were observed to broaden when measuring irradiated HOPG, probably due to degeneration of crystallinity after the introduction of vacancies.

The XANES spectra of HOPG after Pt deposition (Pt/HOPG) and irradiated HOPG after Pt deposition (Pt/irradiated HOPG) were also measured, as shown in Fig. 3.18 (b). The π^* peak was observed to shift toward lower energy by ∼0.2 eV compared to the π^* peak for the both HOPGs before Pt deposition. This shift indicates that the electronic structure due to the π^* orbitals changed due to Pt−C bonding at the interface. In addition, we also observed a peak at ∼284 eV in the spectra of the Pt-deposited samples.

Since the peak at ∼284 eV in the Pt-deposited HOPG was more intense than

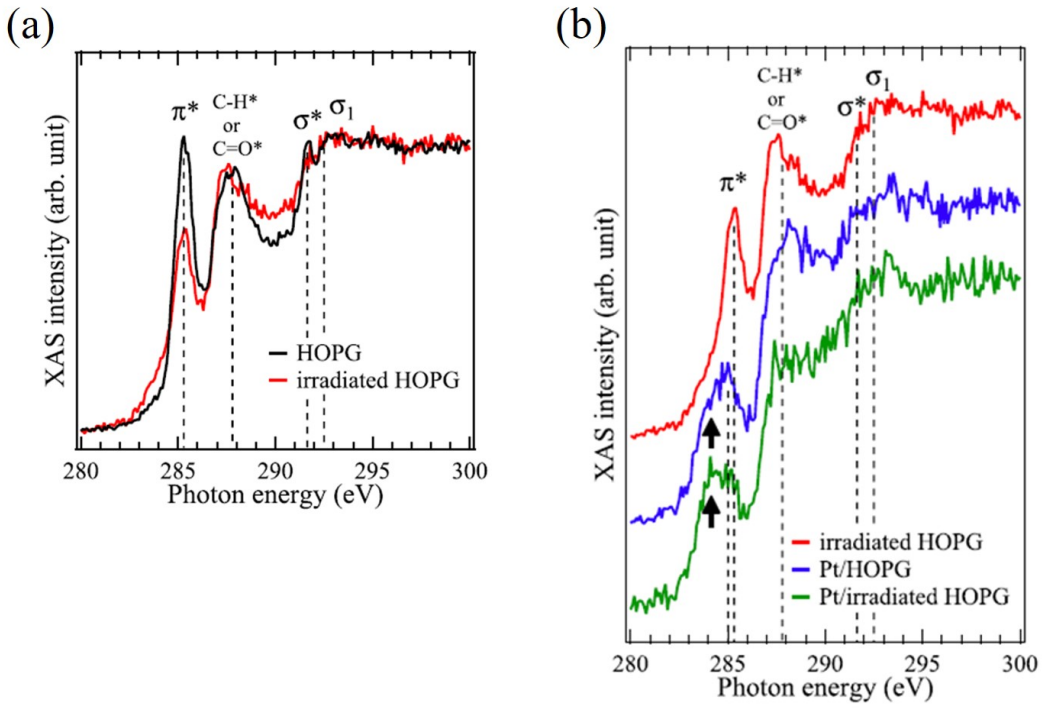

Fig. 3.18: (a) XANES spectra of the C K-edge for non-irradiated HOPG and Ar^+-irradiated HOPG, measured at 30°. (b) XANES spectra of Ar^+-irradiated HOPG, Pt/non-irradiated HOPG, and Pt/Ar^+-irradiated HOPG measured at 30°. Each spectrum is shown shifted in the y-axis direction. These figures are obtained by modifying Fig. 1, 2 of the paper, H. Okazaki et al., J. Chem. Phys. 152, 124708 (2020).

seen for the HOPG without Pt deposition, this peak must have been caused by new electronic structures due to Pt−C bonding at the interface. In previous XANES research, nanographite grown on Pt substrates has shown a similar peak at 283.8 eV, which originated from the edge states [30]. However, the new electronic structure in our XANES spectra was likely due to Pt−C bonding, as this peak increased in intensity in the Pt-deposited HOPGs.

In order to estimate the quantitative changes in the peak intensities due to vacancy introduction, we performed curve fitting of the obtained spectra using the gaussian function and the error function [29], as shown in Fig. 3.19.

We used five gaussian functions (denoted A-E) in the HOPG spectra. Peak A corresponded to the π^* component and was located at ∼285 eV. Peak B consiste

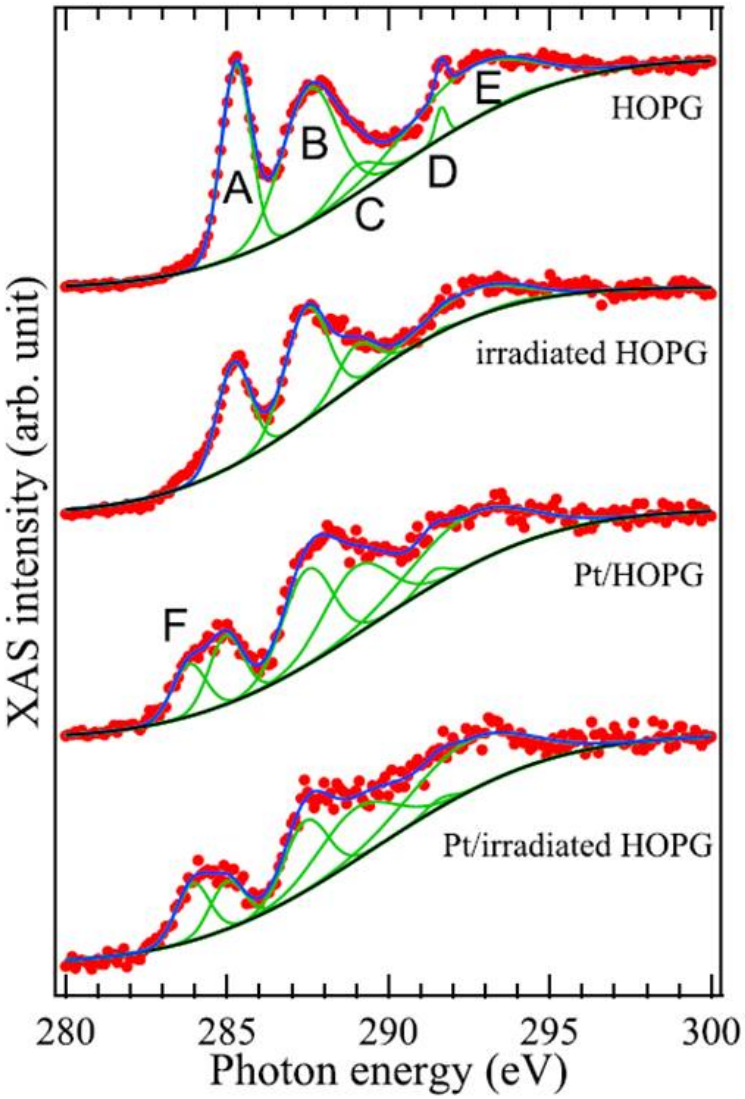

Fig. 3.19: Peak fitting results for all XANES spectra. The red dots, blue line, and green lines indicate the experimental data, the fitting results, and the fitting peak components, respectively. This figure is obtained from Fig. 3 of the paper, H. Okazaki et al., J. Chem. Phys. 152, 124708 (2020).

of the adsorbate component (C$-$H*, C=O*, and so on), located at $\sim$288 eV. Peaks C and E were fixed at 289.0 (π_2) and 292.5 eV (σ_1), as reported in a previous study [28]. Peak D at $\sim$291.5 eV was considered to be due to σ^* [31, 32]. Since this peak was easily broadened and reduced by ion irradiation and Pt deposition, it was likely to be sensitive to crystallinity. The XANES spectra were fitted using the five peaks, as shown in the upper two spectra of Fig.

3.19. After Pt deposition, peak F was added as a new structure due to the Pt−C bonding at around 284 eV. We could then fit the XANES spectra using these six peaks, as shown in the lower two spectra of Fig. 3.19. For the Pt/irradiated HOPG, the intensity ratio of peak F to peak A increased compared to Pt/HOPG. Vacancy introduction increased the intensity ratio by about 57% (the ratio of the new state for Pt/irradiated HOPG compared to Pt/HOPG was 1.198/0.761, where the values were normalized by the area of the fitting function of peak A).

This suggests that the electronic structure originating from Pt−C bonding changed due to the introduction of vacancies into the graphite. An XPS study reported that the core levels of Pt and carbon changed after the introduction of vacancies in glassy carbon substrates [15], with the change in the electronic structure by the introduction of vacancies into the glassy carbon substrate probably leading to suppression of oxidization. The increase in peak F can be considered to indicate improved ORR activity because the increase is related to a change in the Pt−C bonding.

3.5 Summary

The sample preparation method and X-ray spectroscopic analysis of the Pt nanoparticles on Ar^+-irradiated carbon substrates were described in Chapter 3.

The Pt nanoparticles on Ar^+-irradiated carbon substrates were prepared by ion-implanter and rf magnetron sputtering, and then characterized by RBS, FE-SEM, and TEM. The Pt nanoparticles prepared by rf magnetron sputtering for 60 s were about 5-10 nm, and would be in contact with the carbon substrates. The XAFS measurements of Pt M_3- and L_3-edges for the Pt nanoparticles on irradiated glassy carbon substrates clarified that the Ar^+ irradiation led to the suppression of the Pt oxidation. In addition, XPS measurements indicated that the modification of glassy carbon surface by 380 keV Ar^+ irradiation would boost the formation of the Pt−C interactions with charge transfer from Pt to C

at the interface between the Pt nanoparticles and Ar^+-irradiated glassy carbon surface. The C K-edge XANES measurements found a new structure due to the Pt−C bonding on the spectrum of the Pt nanoparticles on Ar^+-irradiated HOPG. These results indicated that the electronic structure originating from Pt−C interactions with charge transfer from Pt to C changed due to the introduction of vacancies into the carbon substrates.

References

[1] Nihon XAFS Kenkyukai: XAFS no Kiso to Oyo *(in Japanese, Fundamentals and Applications of XAFS)* Kodansha (2017).

[2] Y. Saitoh, S. Tajima, I. Takada, K. Mizuhashi, S. Uno, K. Ohkoshi, Y. Ishii, T. Kamiya, K. Yotumoto, R. Tanaka, E. Iwamoto. *TIARA electrostatic accelerators for multiple ion beam application.* Nucl. Instrum. Meth. Phys. Res. B **89**, 23 (1994).

[3] J.F. Ziegler, J.P. Biersack, U. Littmack, The Stopping Range of Ions in Solids, Pergamon Press, NewYork, 1985.

[4] T. Kimata, S. Kato, T. Yamaki, S. Yamamoto, T. Kobayashi, T. Terai. *Platinum nanoparticles on the glassy carbon surface irradiated with argon ions.* Surf. Coat. Technol. **306**, 123 (2016).

[5] M. Mayer, SIMNRA User's Guide, 1997.

[6] J.R. Tesmer,M. Nastasi, Handbook of Modern Ion Beam Materials Analysis, Materials Research Society, Pittsburgh, 1995.

[7] S. Hirano, J. Kim, S. Srinivasan. *High performance proton exchange membrane fuel cells with sputter-deposited Pt layer electrodes.* Electrochim. Acta **42**, 1587 (1997).

[8] Glassy carbon, Tokai Carbon Co., Ltd.,
（http://www.tokaicarbon.co.jp/en/products/fine_carbon/gc.html）

[9] T. Kimata, K. Kakitani, S. Yamamoto, I. Shimoyama, D. Matsumura, A. Iwase, W. Mao, T. Kobayashi, T. Yamaki, T. Terai. *Activity enhancement of platinum oxygen-reduction electrocatalysts using ion-beam induced defects.* ChemRxiv. Preprint. (2017).

[10] H. Konishi, A. Yokoya, H. Shiwaku, H. Motohashi, T. Makita, Y. Kashihara, S. Hashimoto, T. Harami, T. A. Sasaki, H. Maeta, H. Ohno, H. Maezawa, S. Asaoka, N. Kanaya, K. Ito, N. Usami, K. Kobayashi. *Synchrotron radiation beamline to study radioactive materials at the Photon Factory.* Nucl. Instrum. Meth. Phys. Res. A **372**, 322 (1996).

[11] B. Ravel, M. Newville. *ATHENA, ARTEMIS, HEPHAESTUS: data analysis for X-ray absorption spectroscopy using IFEFFIT*. J. Synchrotron Radiat. **12**, 537 (2005).

[12] W. Utsumi, K. Funakoshi, Y. Katayama, M. Yamakata, T. Okada, O. Shimomura. *High-pressure science with a multi-anvil apparatus at SPring-8*. J. Phys. Condens. Matter. **14**, 10497 (2002).

[13] Y. Yazawa, H. Yoshida, T. Hattori. *The support effect on platinum catalyst under oxidizing atmosphere: improvement in the oxidation-resistance of platinum by the electrophilic property of support materials*. Appl. Catal. A Gen. **237**, 139 (2002).

[14] J. Zhang, K. Sasaki, E. Sutter, R. R. Adzic. *Stabilization of Platinum Oxygen-Reduction Electrocatalysts Using Gold Clusters*. Science **315**, 220 (2007).

[15] D.-S. Kim, C. Kim, J.-K. Kim, J.-H. Kim, H.-H. Kim, H. Lee, Y.-T. Kim. *Enhanced electrocatalytic performance due to anomalous compressive strain and superior electron retention properties of highly porous Pt nanoparticles*. J. Catal. **291**, 69 (2012).

[16] J. X. Wang, J. Zhang, R. R. Adzic. *Double-Trap Kinetic Equation for the Oxygen Reduction Reaction on Pt(111) in Acidic Media*. J. Phys. Chem. A **111**, 12702 (2007).

[17] J. J. Rehr, R. C. Albers. *Theoretical approaches to x-ray absorption fine structure*. Rev. Mod. Phys. **72**, 621 (2000).

[18] P. Strasser, S. Koh, T. Anniyev, J. Greeley, K. More, C. Yu, Z. Liu, S. Kaya, D. Nordlund, H. Ogasawara, M. F. Toney, A. Nilsson. *Lattice-strain control of the activity in dealloyed core shell fuel cell catalysts*. Nat. Chem. **2**, 454 (2010).

[19] K. Kakitani, T. Kimata, T. Yamaki, S. Yamamoto, D. Matsumura, T. Taguchi, T. Terai. *X-ray absorption study on platinum nanoparticles on an ion-irradiated carbon support*. Radiat. Phys. Chem. **153**, 152 (2018).

[20] Z. Liu, X.Y. Ling, B. Guo, L. Hong, J.Y. Lee. *Pt and PtRu nanoparticles deposited on single-wall carbon nanotubes for methanol electro-oxidation*. J. Power Sources **167**, 272 (2007).

[21] S. Hüfner, G.K. Wertheim. *Core-line asymmetries in the x-ray-photoemission spectra of metals*. Phys. Rev. B **11**, 678 (1975).

[22] J. Knecht, G. Stork. *X-ray photoelectron spectroscopic examination of the Thallium oxide electrode*. Fresenius' Z. Anal. Chem. **289**, 206 (1978).

[23] G. Gupta, D.A. Slanac, P. Kumar, J.D. Wiggings-Camacho, J. Kim, R. Ryoo, K.J. Stevenson, K.P. Johnston. *Highly stable Pt/ordered graphitic mesoporous carbon electrocatalysts for oxygen reduction*. J. Phys. Chem. C **114**, 10796 (2010).

[24] J.F. Evans, T. Kuwana. *Electrocatalysis of proton-coupled electron-transfer reactions at glassy carbon Eleectrodes*. J. Am. Chem. Soc. **107**, 1845 (1985).

[25] Z. Paál. *XPS of carbon on Pt-black and EUROPT-1. Is methylcyclopentane ring opening a 'coke sensitive' reaction?*. J. Mol. Catal. **94**, 225 (1994).

[26] H. Okazaki, K. Kakitani, T. Kimata, A. Idesaki, H. Koshikawa, D. Matsumura, S. Yamamoto, T. Yamaki. *Changes in electronic structure of carbon supports for Pt catalysts induced by vacancy formation due to Ar^+ irradiation*. J. Chem. Phys. **152**, 124708 (2020).

[27] A. Nilsson. *Applications of core level spectroscopy to adsorbates*. J. Electron Spectrosc. Relat. Phenom. **126**, 3 (2002).

[28] A. Nikitin, L.-Å. Näslund, Z. Zhang, A. Nilsson. *$C-H$ bond formation at the graphite surface studied with core level spectroscopy*. Surf. Sci. **602**, 2575 (2008).

[29] J. Stöhr. NEXAFS Spectroscopy (Springer-Verlag, Berlin, 1992).

[30] S. Entani, S. Ikeda, M. Kiguchi, K. Saiki, G. Yoshikawa, I. Nakai, H. Kondoh, T. Ohta. *Growth of nanographite on Pt(111) and its edge state*. Appl. Phys. Lett. **88**, 153126 (2006).

[31] P. A. Brühwiler, A. J. Maxwell, C. Puglia, A. Nilsson, S. Andersson, N. Mårtensson. *π^* and σ^* excitons in C 1s absorption of graphite*. Phys. Rev. Lett. **74**, 614 (1995).

[32] Y. Ma, P. Skytt, N. Wassdahl, P. Glans, J. Guo, J. Nordgren. *Core excitons and vibronic coupling in diamond and graphite*. Phys. Rev. Lett. **71**, 3725 (1993).

Chapter 4

Raman spectroscopic analysis of irradiated graphite surface with Pt nanoparticles

4.1 Introduction

The Pt nanoparticles on Ar^+-irradiated glassy carbon and HOPG substrate were investigated using XAFS and XPS measurements, the results indicated the presence of Pt−C interaction at the interface between Pt nanoparticles and Ar^+-irradiated carbon supports, in Chapter 3. In Chapter 4, the surface structure of the carbon support irradiated with Ar^+ is investigated using Raman spectroscopy.

Although the studies of Raman spectroscopy for the defective graphite/graphene or the carbon nanocubes supporting Pt nanoparticles were reported previously [1–4], the ion-beam-irradiated graphite supporting Pt nanoparticles have not been investigated by Raman spectroscopy. Pt nanoparticles deposited on a HOPG surface have been used as a model catalyst [5, 6], e.g. a study on the influence of nitrogen-doped carbon support on the catalytic activity of Pt nanoparticles [7], and were also used in Chapter 3.

Herein, we deposited Pt nanoparticles on both Ar^+-irradiated and pristine HOPG, using rf magnetron sputtering, and then investigated the influence of

the ion-beam irradiation and Pt deposition on the surface structure of carbon supports by Raman spectroscopy. The number of defects interacting with Pt nanoparticle is also estimated by the phonon correlation length obtained from Raman peaks.

4.1.1 Raman spectroscopy

Raman spectroscopic analysis is well known as a strong tool for investigation of defective structure in condensed matter. When a sample is exposed to monochromatic light in the visible region, the sample absorbs light and a major portion of the light gets transmitted through the sample, however, a minute part of the light is scattered by the sample in all the directions. If the scattered light has the frequency same as the incident light, the scattering is called Rayleigh scattering ($\nu_s = \nu_i$, where ν_s and ν_i are wavenumbers of scattered and incident lights, respectively.). It has also been observed the scattered light of frequencies different from the incident frequency. This is called Raman scattering ($\nu_s \neq \nu_i$).

Fig. 4.1 shows the schematic diagram of the energy transitions involved in Rayleigh scattering and Raman scattering. In Rayleigh scattering, the scattered light has the same wavenumber with the incident light ($\nu_s = \nu_i$). The optical process of Rayleigh scattering is represented as shown in Fig. 4.1 (a). In Raman scattering, on the other hand, the incident light interacts with phonons in the system, resulting in the energy being shifted down or up. When the wavenumber of scattered light is lower than that of incident light ($\nu_s < \nu_i$), the stokes line is observed. If it is higher ($\nu_s > \nu_i$), the anti-stokes line is observed. These scattering processes are thought of in terms of wavenumber of the incident light and vibrational transition, ν_v, as shown in Fig. 4.1 (b,c). The stokes scattering gives a wavenumber of $\nu_i - \nu_v$, while $\nu_i + \nu_v$ is given for anti-stokes scattering.

The frequency and intensity values of a Raman line are helped to identify a particular structure and to determine the concentration of a structure in a sample,

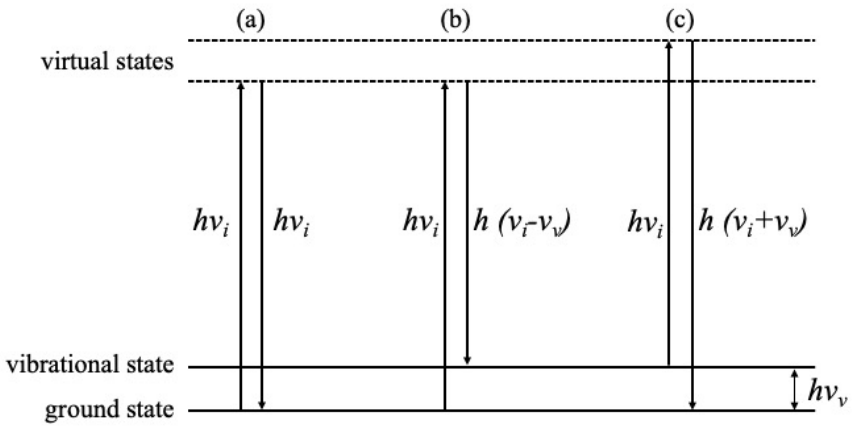

Fig. 4.1: Schematic diagram of the energy transitions involved in (a) Rayleigh scattering, (b) stokes scattering, and (c) anti-stokes scattering. ν_i and ν_v are the wavenumber of incident light and vibrational transition, respectively.

respectively. Thus, Raman spectroscopy can be used to perform both quantitative and qualitative analysis of a sample.

A general Raman spectrometer configuration is briefly described. Figure 4.2 shows the schematic of the Raman spectrometer. The Raman spectrometer consists of a light source, a filter to remove Rayleigh scattered light, a diffraction grating to decompose Raman scattered light into a spectrum, and a CCD detector. The laser beam from the light source is guided to the sample and irradiated to excite it. The scattered light from the sample is introduced through a filter into the monochromator with only the scattered Raman light, and the spectrum is recorded by the detector.

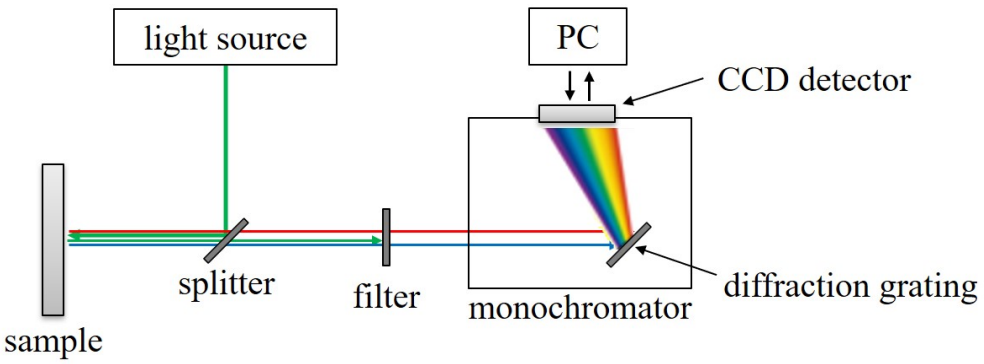

Fig. 4.2: The schematic of Raman spectrometer.

4.1.2 Raman spectrum of the irradiated glassy carbon substrate

At first, the glassy carbon substrates irradiated with the same conditions described in Chapter 3, were investigated using Raman spectroscopy [8].

Figure 4.3 shows Raman spectra of the glassy carbon substrates irradiated with 380 keV Ar^+ at the different fluences, and then heated at 400 °C, and that of the pristine glassy carbon substrate. The pristine glassy carbon substrate exhibited two peaks at around 1590 and 1350 cm^{-1}. The peak at 1590cm^{-1} can be identified as the E_{2g} mode of the graphite structure, which is called the G peak. The 1350 cm^{-1} peak should be attributed to a disordered mode of graphite (A_{1g} mode) [9], which is called the D peak. As the ion fluence increased, the irradiated glassy carbon surfaces represented the following general trends: a broadening of each peak and, especially at higher fluences, a downward shift of the G peak. Both of these suggest the destruction of the graphitic structures in the glassy carbon surface during the Ar^+ irradiation [10].

The G-peak shift and the relative intensity of the D to G peaks (defined as I_D/I_G) were used to investigate the structure of the Ar^+-irradiated glassy carbon surface. In the fluence range of 1.0×10^{13} and 1.0×10^{14} ions/cm^2, the position of the G peak remained at approximately 1590 cm^{-1}; on the other hand, it gradually moved down to 1540 cm^{-1} above a fluence level of 1.0×10^{14} ions/cm^2 [11]. The G peak shift accompanying an increase in the defect density saturated at 1540 cm^{-1} [10].

Tuinstra and Knight have reported that the I_D/I_G ratio was inversely proportional to the in-plane crystallite size for disordered graphite in any carbon sample [12, 13]. In addition, Nakamura *et al.* reported that the in-plane crystallite size for disordered graphite corresponds to the phonon correlation length [14, 15]. In Chapter 4, the interface structure between Pt nanoparticles and defective carbon substrate is investigated by Raman spectroscopy using HOPG as carbon support.

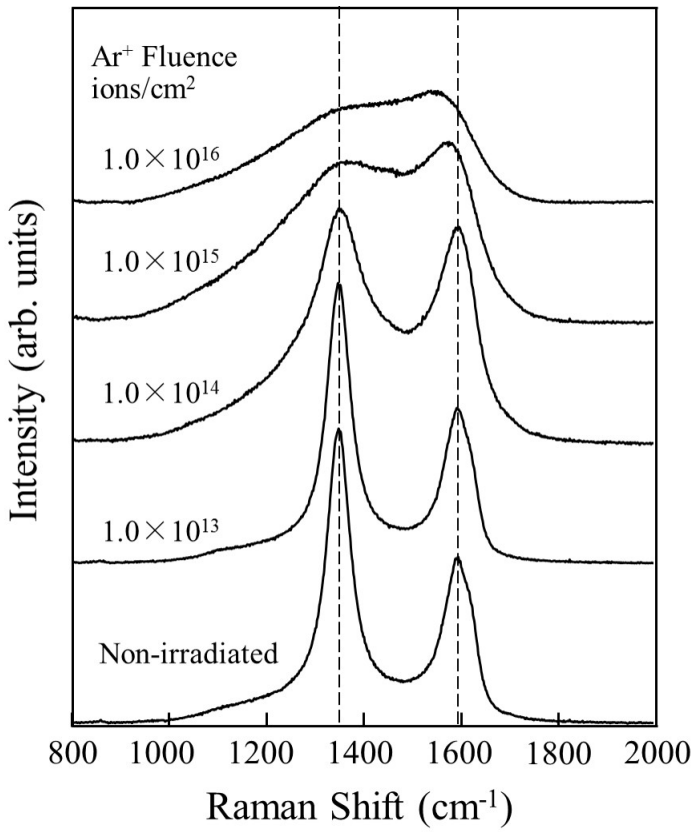

Fig. 4.3: Raman spectra of glassy carbon substrate irradiated at room temperature with 380 keV Ar^+ and then heated at 400°C in an N_2 atmosphere for 1 h. This figure is obtained from Fig. 1 of the paper, T. Kimata et al., Surf. Coat. Technol. 306, 123 (2016).

4.2 Sample preparation

4.2.1 Ion-beam irradiation and Pt deposition

An HOPG (Grade SPI-II, SPI Supplies, West Chester, PA) with dimensions of $10\times10\times1$ mm^3 was used in this chapter. Clean thin specimens were obtained from this bulk material using an adhesive tape technique. Ar^+-irradiation was performed at an energy of 380 keV and fluences between 1.0×10^{12} and 1.0×10^{14} ions/cm^2, using the ion implanter at the TIARA. These fluence values were estimated by taking the product of the ion beam current density and the irradiation time. The current density was set at 10 nA/cm^2 in order to prepare a sample with a lower fluence than that in Chapter 3. Pt nanoparticles were subsequently deposited on the HOPG surfaces by an rf magnetron sputtering method in a sample preparation chamber (base pressure $< 6\times10^{-5}$ Pa), using Ar as the sputtering gas at a pressure of 0.18 Pa. The plasma output, frequency, and sputtering time were 20 W, 13.56 MHz, and 60 s, respectively.

Figure 4.4 shows the depth profile of the defect density calculated using the TRIM code [16] for 380 keV Ar^+ in graphite with an irradiation angle normal to the c-face. A graphite density of 2.2 g/cm^3 was applied during these calculations. The defect density was determined to be approximately 0.2 atoms/Å/ion at 10 nm and this value gradually increased to a depth of 250 nm. The TRIM code was unable to calculate the defect density at the surface (that is, at 0 nm).

The optical absorption coefficient of graphite at 532 nm was calculated to be 0.032 nm^{-1} based on the equation

$$\alpha = 4\pi \times \frac{k}{532}, \tag{4.1}$$

where k=1.3 is the extinction coefficient of graphite [17]. Therefore, Raman scattering by the sample was affected by both the surface and the interior of the sample. Variations in sensitivity with depth in the back-scattering configuration were evaluated using the normalized optical penetration factor exp(-αx)

(where x is the depth from the upper surface), as shown in Fig. 4.4. The sensitivity varies in this manner because both the excitation and scattered light are absorbed by the sample. The depth to which the sample could be probed by Raman spectroscopy was estimated to be $1/2\alpha$, which in this case was 16 nm.

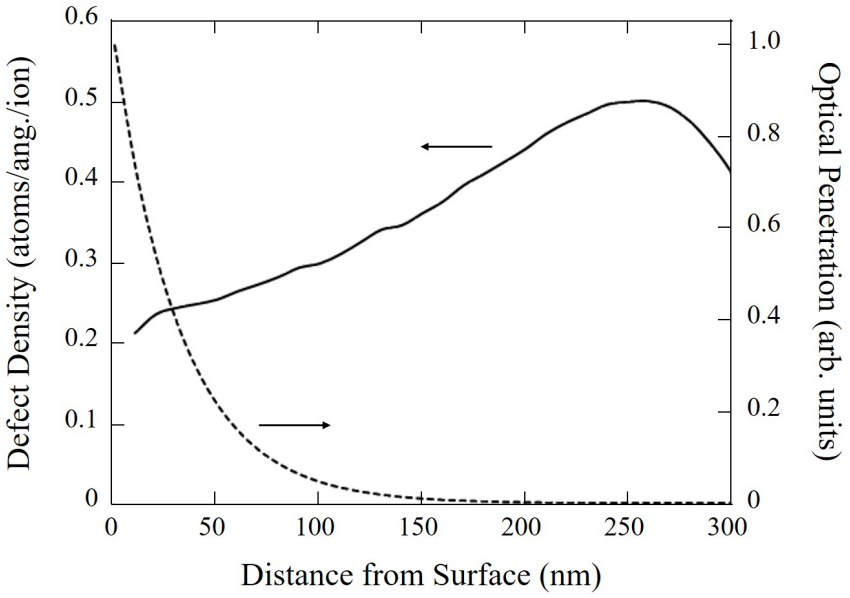

Fig. 4.4: The defect distribution depth profile following 380 keV Ar^+ irradiation of graphite as determined by TRIM calculations. The broken line represents the normalized optical penetration factor exp(-αx) for 532 nm light in graphite. This figure is obtained from Fig. 1 of the paper, T. Kimata et al., Nucl. Instrum. Meth. Phys. Res. B 444, 6 (2019).

4.2.2 Characterization of nanoparticle size

In order to evaluate the particle size, Pt nanoparticles on the non-irradiated HOPG and irradiated ones (fluence: 1.0×10^{12} and 5.0×10^{13} ions/cm^2) were observed using TEM [18]. The specimens for TEM observations were prepared by rubbing the Pt/HOPG sample surfaces with TEM grid meshes. TEM experiments were operated using JEM-2010F (JEOL Co., Ltd, Japan) at an accelerating voltage of 200 keV.

Figure 4.5 (a), (b) and (c) show the TEM images of the Pt nanoparticles on non-irradiated HOPG and irradiated HOPG at the fluence of 1.0×10^{12} and

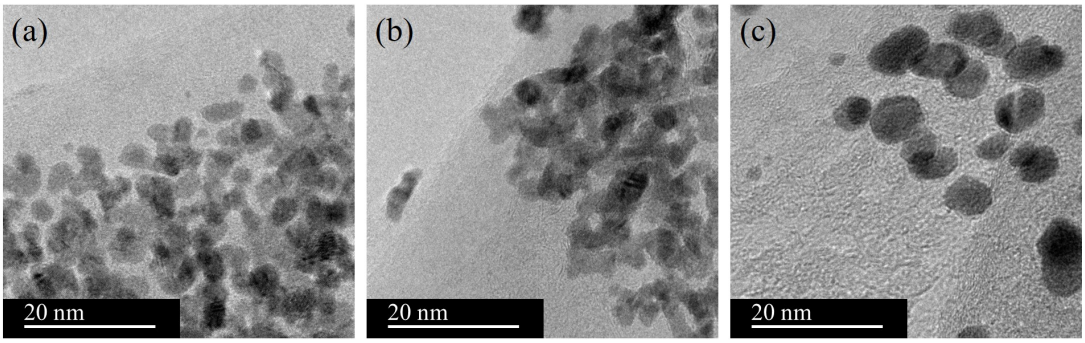

Fig. 4.5: TEM images of the Pt nanoparticles on (a) pristine HOPG surface and HOPG surface irradiated with Ar ions at the fluences of (b) 1.0×10^{12} and (c) 5.0×10^{13} ions/cm^2. These figures are obtained from Fig. 1 of the paper, T. Kimata et al., Radiat. Eff. Deff. Sol. 175, 433 (2020).

5.0×10^{13} ions/cm^2, respectively. The darker objects correspond to the Pt nanoparticles. In these TEM images, some Pt nanoparticles were agglomerated because the nanoparticles on the HOPG were collected by rubbing the surface with a TEM grid mesh.

The histograms of measured sizes of Pt nanoparticles were shown in Fig. 4.6. The mean particle size on the non-irradiated HOPG was 2.85 nm, while mean particle sizes on HOPG irradiated at the fluences of 1.0×10^{12} and 5.0×10^{13} ions/cm^2 were 3.11 and 6.02 nm, respectively. The size was different between the three samples in spite of the same condition of Pt deposition method. Previously, we performed cross-sectional TEM for the Pt nanoparticles on glassy carbon substrates which were non-irradiated and irradiated with Ar^+ at the fluence of 7.5×10^{15} ions/cm^2 [19]. The mean particle size of the non-irradiated and irradiated samples were 3.8 and 5.1 nm, respectively. The tendency for nanoparticle size to increase with pre-irradiation was consistent between HOPG and glassy carbon. Therefore, we found that the irradiation-induced defects in the graphitic structure promoted the growth of the Pt nanoparticles, resulting in their larger size.

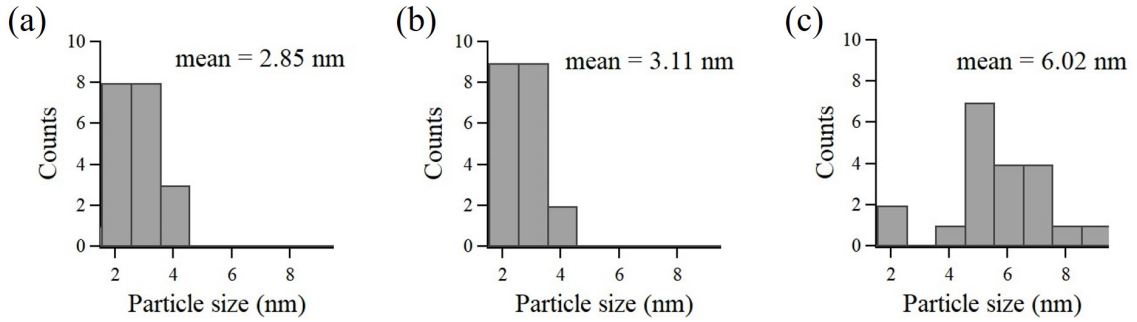

Fig. 4.6: Pt nanoparticle size distributions in the samples of (a) non-irradiated HOPG and HOPG irradiated with Ar ions at the fluences of (b) 1.0×10^{12} and (c) 5.0×10^{13} ions/cm^2. These figures are obtained from Fig. 2 of the paper, T. Kimata et al., Radiat. Eff. Deff. Sol. 175, 433 (2020).

4.3 Raman spectroscopic analysis

4.3.1 Experimental setup

Raman spectroscopic analysis of the pristine and pre-irradiated HOPG surfaces before and after the Pt deposition was performed using a LabRAM HR Evolution Raman spectrometer (HORIBA, Ltd., Japan) over the wavenumber range of 500-3500 cm^{-1} at a resolution of 1.60 cm^{-1}. Figure 4.7 shows the Raman spectrometer. Incident radiation at 532 nm was provided using a single-mode green laser (Showa Optronics JUNO J050GS-16, Japan), at a power level below 5 mW, applied to a sample area with a diameter of approximately 15 μm. Raman spectra were obtained with a back-scattering configuration by accumulating the signal during a 5 minutes exposure, and analyzed by fitting all peaks to a Lorentzian profile after subtracting constant background.

4.3.2 Results and discussion

Fig. 4.8 (a) shows the Raman spectra of the non-irradiated HOPG and the HOPG irradiated with Ar ions at the fluence of 1.0×10^{12}, 5.0×10^{12}, 1.0×10^{13} and 5.0×10^{13} ions/cm^2.

The first-order G band related to the in-plane stretching vibration of the C$-$C

(a) (b)

Fig. 4.7: (a) Raman spectrometer and (b) its inside.

bonds appeared at 1583.5 cm^{-1} in the spectrum of the non-irradiated HOPG. In the spectra of the irradiated HOPG, the defect-induced D and D' bands were observed at approximately 1350 cm^{-1} and 1620 cm^{-1}, respectively, due to the phonon wave vector is $q \neq 0$ [20]. The second-order 2D band, the overtone of the D band, appeared in the range of 2500-2800 cm^{-1}. The 2D band is related to the two phonon lattice vibrations, but it is symmetry-allowed and, unlike the D band, does not indicate the presence of defects [21, 22]. The D' band also has a non-disorder induced overtone, the G" band; this is the Raman band at ≈3250 cm^{-1}. The Raman band at ≈2450 cm^{-1} is also a two-phonon band (G* mode) [23, 24]. The band at ≈2925 cm^{-1} has been assigned to the D+G mode, and is defect activated and hence will be present only in samples with sufficient defects [24, 25].

In the HOPG surface irradiated at higher fluence, the resulting spectrum shows a broader and higher D peak in comparison to G peak, flattened 2D peak, appeared D+G peak, and disappeared G* and G" peaks. This trend was similar with the graphite irradiated by neutron [26] and focused ion beam [27]. The Raman spectra of the graphite following Pt deposition are shown in Fig. 4.8 (b). The similar spectra with before Pt deposition were obtained.

The surface structure of irradiated HOPG and the interface structure between Pt nanoparticles and irradiated HOPG are investigated by D, D' and G peaks.

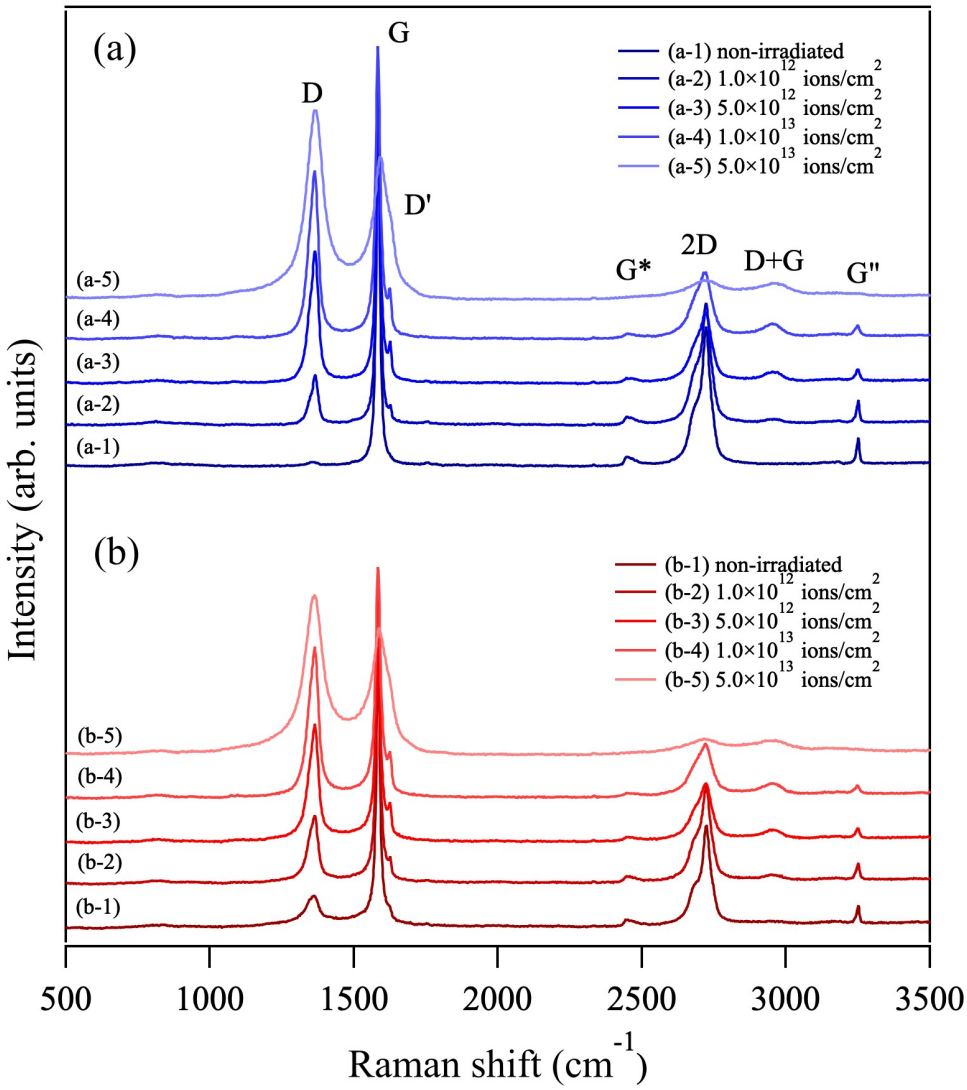

Fig. 4.8: Raman spectra of the non-irradiated HOPG and the HOPG irradiated at the fluence of 1.0×10^{12}, 5.0×10^{12}, 1.0×10^{13} and 5.0×10^{13} ions/cm^2 (a) without and (b) with Pt nanoparticles. This figure is obtained from Fig. 3 of the paper, T. Kimata et al., Radiat. Eff. Deff. Sol. 175, 433 (2020).

The results are described below.

4.3.2.1 Surface structure of irradiated graphite

All peaks of the spectra are fitted by a Lorentzian profile after subtracting constant background, and then are analyzed by the intensity ratio of D/D'; the peak intensity is the amplitude acquired by Lorentzian fitting. Figure 4.9 shows the D/D' intensity ratio against Ar^+ fluence. According to the study of Eckmann *et al.* [28], the D/D' intensity ratio indicates the nature of defects in graphitic structure; the D/D' $\simeq$13 is associated with sp^3 defects, then it decreases for vacancy-like defects ($\simeq$7) reaching a minimum of $\simeq$3.5 for dominant boundaries in graphite. The D/D' ratio of the Pt nanoparticles on the non-irradiated HOPG was approximately 3.2, indicating that the graphite structure is dominant. Between 1.0 $\times 10^{12}$ and 1.0×10^{13}, the D/D' ratio was 4.4 to 5.0, and vacancy-like defects would be generated on the HOPG surface. Furthermore, the D/D' ratio on the irradiation of 5.0×10^{13} ions/cm^2 reached approximately 8.8, indicating that not only vacancy-like defects but also sp^3 defects exist. The surface structure of HOPG modified by Ar^+-irradiation would affect the size of the Pt nanoparticles.

4.3.2.2 Interface structure between Pt nanoparticles and irradiated graphite

Figure 4.10 presents the Raman spectra of the pristine HOPG and the Pt nanoparticles on HOPG (Pt/HOPG). The spectrum of the pristine HOPG shows a sharp peak at 1583.5 cm^{-1} with a full width at half maximum (FWHM) of approximately 13.7 cm^{-1}, attributed to the G peak of the graphite due to the in-plane E_{2g} mode. In contrast, the spectrum from the HOPG with Pt nanoparticles exhibits two other peaks at 1356.9 and 1621.5 cm^{-1} in addition to a slightly broadened G peak. These peaks indicate the presence of defects in the sp^2 C lattice, and correspond to the D and D' peaks. The in-plane microcrystalline

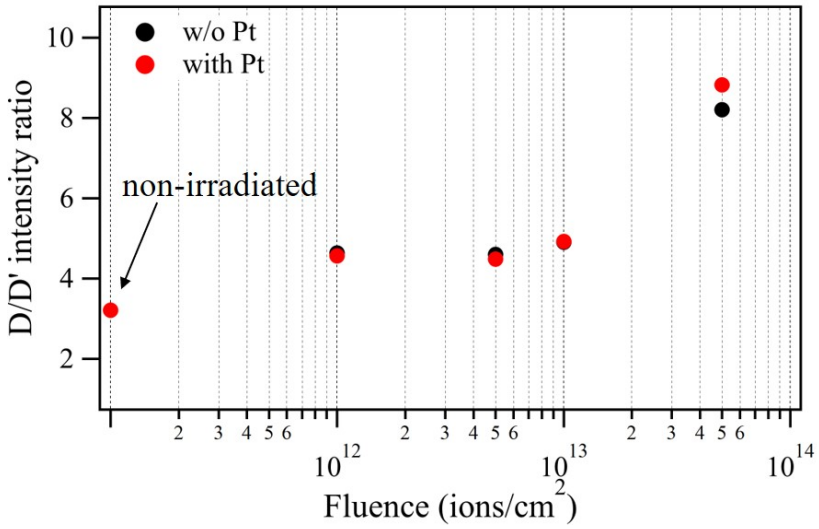

Fig. 4.9: D/D' intensity ratio plotted against Ar^+ fluence (black point: without Pt, red point: with Pt). This figure is obtained by modifying Fig. 4 of the paper, T. Kimata et al., Radiat. Eff. Deff. Sol. 175, 433 (2020).

size (L_a) is typically determined from the peak intensity ratio (R=I_D/I_G), such that

$$L_a = \frac{4.4}{R}(nm), \tag{4.2}$$

where I_G and I_D represent the intensities of the G and D peaks [12, 13], and previous studies have suggested that L_a corresponds to the phonon correlation length [14, 15]. This peak intensity was the area intensity acquired by Lorentzian fitting. The L_a value for the HOPG with Pt nanoparticles was estimated to be 11.2 nm. This result that the appearance of D peak in the Raman spectrum of HOPG with Pt nanoparticles, and the lack of a D peak in the spectrum of the pristine HOPG, suggested that the HOPG surface had been damaged by the Pt deposition.

Figure 4.11 shows the spectra at the wavenumber range of 1200-1750 cm^{-1} of the HOPG irradiated with Ar^+ at the fluences between 1.0×10^{12} and 1.0×10^{14} ions/cm^2 as obtained before and after Pt deposition. In these figures, red circles and black lines indicate the obtained data and curve-fitting lines, respectively. The Raman spectra of the samples excluding 1.0×10^{14} ions/cm^2 were fitted by

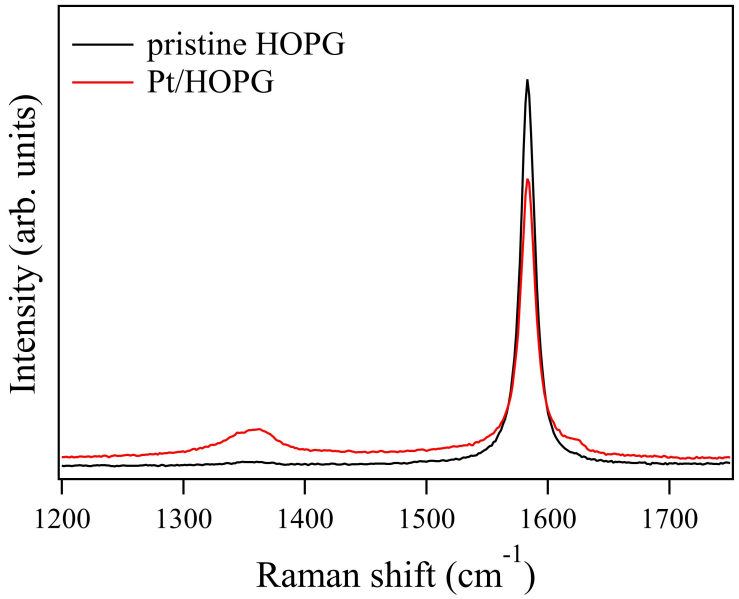

Fig. 4.10: The Raman spectra of the pristine HOPG and the Pt nanoparticles on HOPG (Pt/HOPG). This figure is obtained by modifying Fig. 2 of the paper, T. Kimata et al., Nucl. Instrum. Meth. Phys. Res. B 444, 6 (2019).

3 peaks (G, D and D' peaks), but that of the 1.0×10^{14} ions/cm^2 sample were fitted by G and D peaks because a D' peak was unremarkable in the spectra. The peak parameters obtained by curve fitting, including position and FWHM of G peak without and with Pt deposition, are summarized in Fig. 4.12.

Figure 4.12 (a) shows the G peak position plotted against Ar^+ fluence. The significant peak-shift by the Ar^+-irradiation and Pt deposition was not observed on the fluence of under 1.0×10^{13} ions/cm^2. On the fluence of over 5.0×10^{13} ions/cm^2, the blueshift of the G peaks by the Ar^+-irradiation and the redshift of the G peaks by the Pt deposition were observed. As can be seen from Fig. 4.12 (b), the higher fluence, the larger G-peak bandwidth.

The blue shift and red shift correspond to the approach and separation of the C−C distance, respectively; the blue shift and red shift are caused by compressive and tensile stresses respectively [29, 30], as shown in Fig. 4.13.

The blue shift of the G bands by the Ar^+-irradiation is considered to cor-

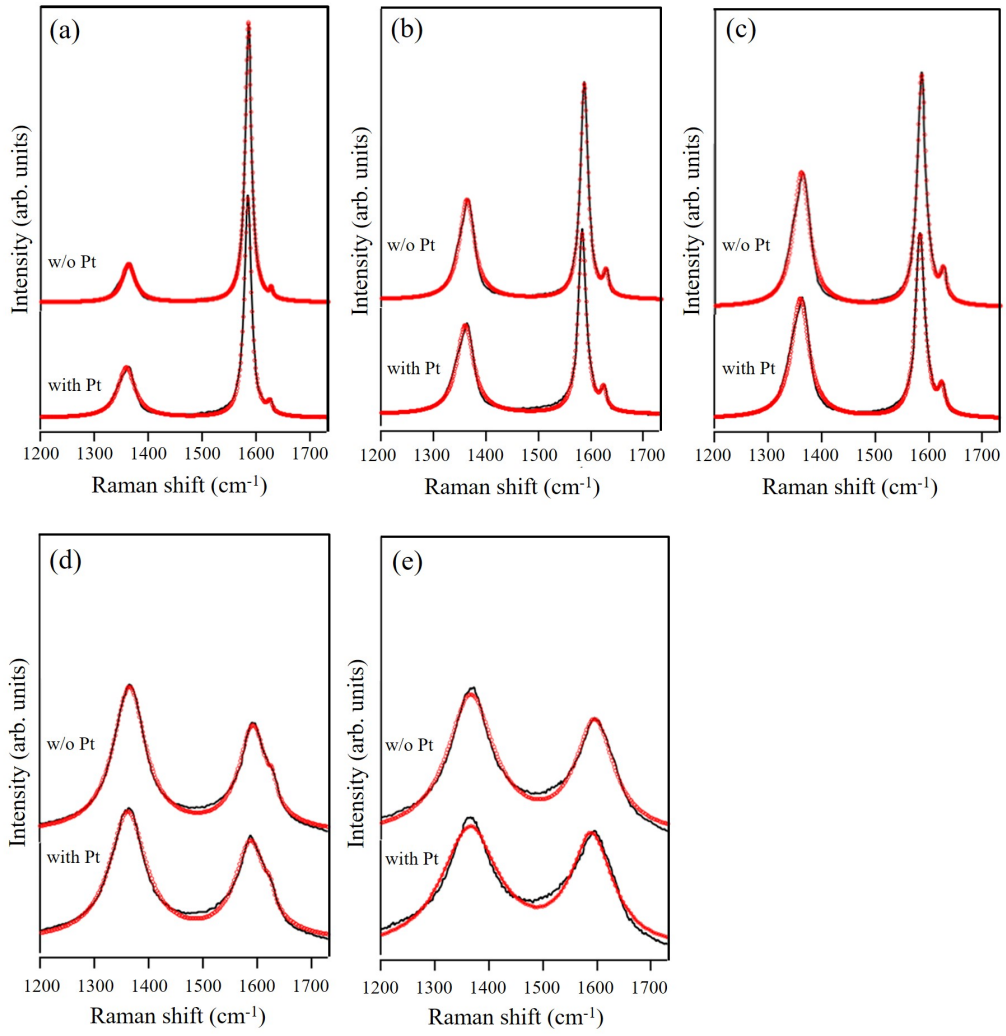

Fig. 4.11: The Raman spectra of the HOPG irradiated with Ar^+ at a fluence between 1.0×10^{12} and 1.0×10^{14} ions/cm^2 without and with Pt deposition. These figures are obtained by modifying Fig. 3 of the paper, T. Kimata et al., Nucl. Instrum. Meth. Phys. Res. B 444, 6 (2019).

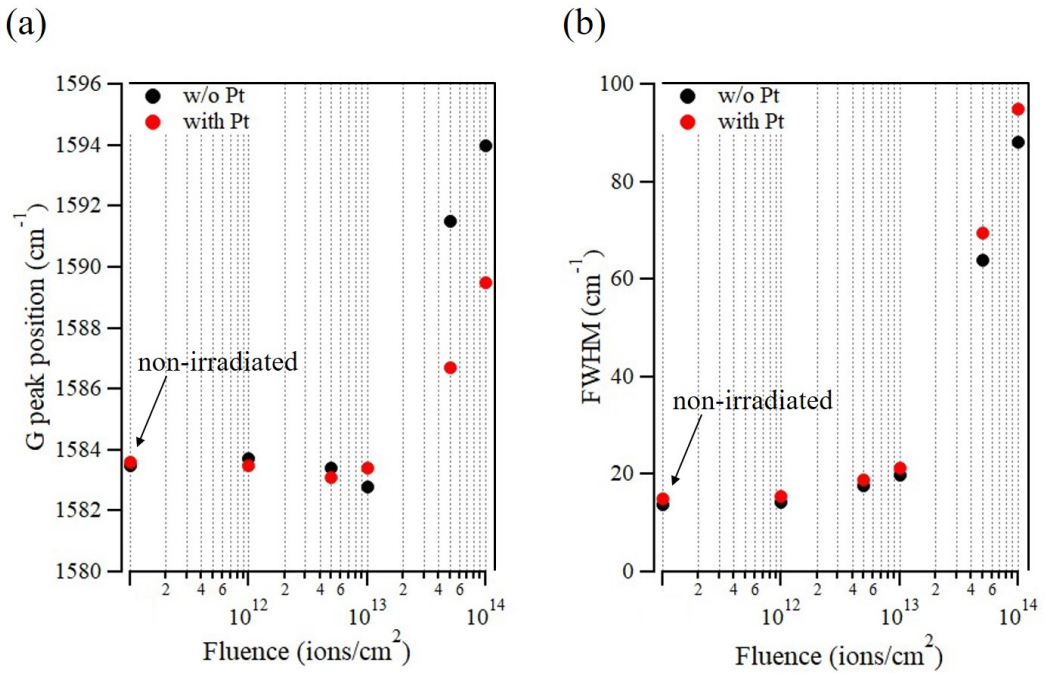

Fig. 4.12: The (a) position and (b) FWHM of the G peak plotted against Ar^+ fluence (black point: without Pt, red point: with Pt). These figures are obtained by modifying Fig. 4 of the paper, T. Kimata et al., Nucl. Instrum. Meth. Phys. Res. B 444, 6 (2019).

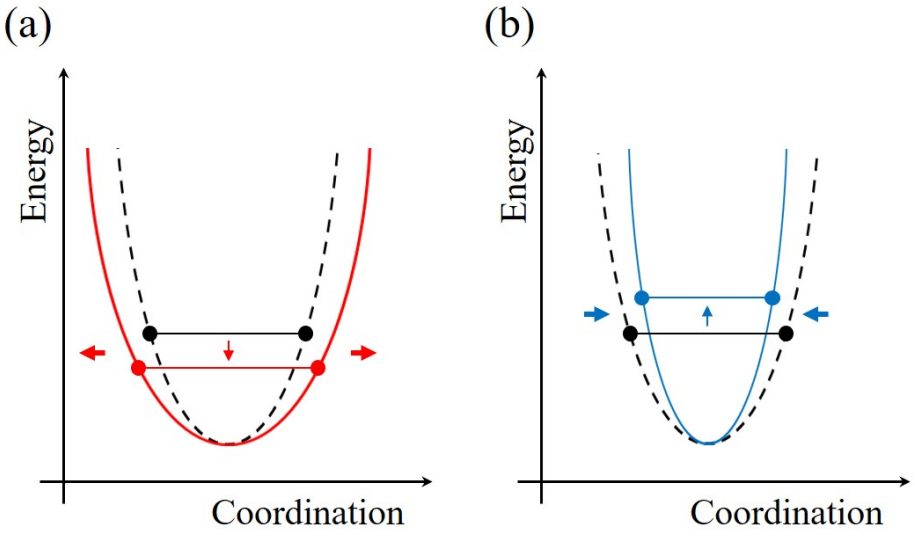

Fig. 4.13: The schematic of (a) redshift and (b) blueshift.

respond with the process from graphite to nanocrystalline graphite (Stage 1) suggested by Ferrari *et al.* [31, 32]. The blueshift of G peak is really the appearance of a D' peak, which merges in the G peak [31]. The appearance of D' peak occurs because the relaxation of the q=0 selection rule ($q \neq 0$) allows higher-frequency phonons, as phonons disperse upwards away from Γ [31]. On the other hand, a high-frequency shift with decreasing graphite layer has also been reported [33]. This shift may be attributed to the slightly stronger C−C bonding due to the weaker interaction between the graphite layers by vacancy introduction (because of slight softening of the C−C bonds as the graphene layer thickness increases [34]). As the structure becomes more disturbed, the lower the Raman shift of the G band and the wider its bandwidth [35, 36]. This trend of the Raman shift was consistent with the redshift of the G peaks by the Pt deposition, as can be seen from Fig. 4.12 (a), and the trend of the bandwidth was also consistent with that of FWHM (Fig. 4.12 (b)). The red shift after Pt deposition becomes more obvious with higher degree of HOPG modification, i.e. after exposure to higher ion fluence. The red shift of the G bands by the Pt deposition is considered to correspond with the process from nanocrystalline graphite to amorphous carbon (Stage 2) suggested by Ferrari *et al.* [31, 32]. Indeed, in Fig. 4.9, the HOPG irradiated at the fluence of 5.0×10^{13} ions/cm^2 with Pt nanoparticles also suggested the presence of sp^3 bonds.

Figure 4.14 (a, b) shows the value of the R and L_a. The R is a measure of the disorder caused by the lattice damage; the value increased at higher fluence, and was further increased by Pt deposition except for the sample of 5.0×10^{13} ions/cm^2. The increasing R directly denotes defectivity of the surface and subsurface region. Pt deposition had lower effect on defectivity of the HOPG surface with increasing Ar^+-irradiation on the substrate prior deposition of Pt. The same principle applies for L_a (Fig. 4.14 (b)), the Pt deposition had lower effect on L_a at higher fluence.

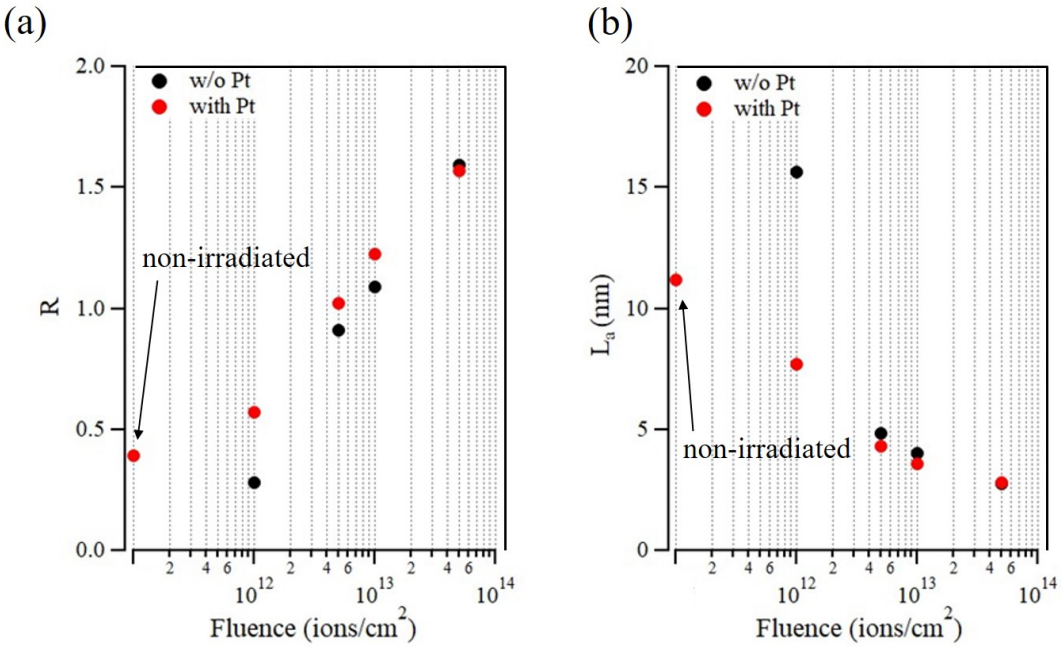

Fig. 4.14: The value of (a) R and (b) L_a (black point: without Pt, red point: with Pt). These figures are obtained by modifying Fig. 5 of the paper, T. Kimata et al., Nucl. Instrum. Meth. Phys. Res. B 444, 6 (2019).

We calculated the mean distance (L) between in-plane defects using the defect density data in Fig. 4.4 (0.2 atoms/Å/ion at a depth of 10 nm) based on the equation

$$L = \frac{1}{\sqrt{f \times N_d}}, \tag{4.3}$$

where N_d is the number of defects and f is the distance between the graphite layers (3.35 Å) [37, 38]. The value of N_d was estimated from the defect density and the fluence, and the L value obtained when employing a fluence of 1.0×10^{13} ions/cm^2 was 3.86 nm. This L value calculated using the data generated by the TRIM code (Fig. 4.4) is slightly shorter than the L_a value estimated from the Raman spectrum (4.04 nm). This result may suggest that the graphitic structure at a depth of 10 nm was more defective than at surface, however, the accuracy of these would be comparable. We additionally investigated the number of lattice defects under the Pt nanoparticles for modeling of the interface structure between Ar^+-irradiated HOPG surface and Pt nanoparticles on the theoretical

calculation. The L_a value of the sample treated with a fluence of 1.0×10^{13} ions/cm^2 and Pt deposition (3.59 nm) suggested that approximately three point defects were present at the interface between each 5 nm Pt nanoparticle and the Ar^+-irradiated HOPG.

4.4 Summary

In Chapter 4, Raman spectroscopy was used to study the structure of non-irradiated and Ar^+-irradiated HOPG before and after Pt deposition.

The D/D' ratio obtained from Raman spectra indicated that the vacancy-like defects existed on the HOPG surface with Ar^+-irradiation at the fluences below 1.0×10^{13} ions/cm^2, and sp^3 defects existed with irradiation more than 5.0×10^{13} ions/cm^2. The effect of Pt deposition induced damage was observed in Raman spectrum of the non-irradiated HOPG, and also observed slightly in that of the Ar^+-irradiated HOPG. Pt deposition showed more significant red shift of the G peak with increasing Ar^+ fluence, whereas it interestingly had an opposite effect on L_a. In addition, the obtained L_a estimated hat approximately three point defects were present at the interface structure between each 5 nm Pt nanoparticle and the HOPG irradiated with Ar^+ at the fluence of 1.0×10^{13} ions/cm^2.

References

[1] A. C. Ferrari. *Raman spectroscopy of graphene and graphite: Disorder, electron-phonon coupling, doping and nonadiabatic effects.* Solid State Comm. **143** (2007) 47.

[2] L. G. Cançado, A. Jorio, E. H. Martins Ferreira, F. Stavale, C. A. Achete, R. B. Capaz, M. V. O. Moutinho, A. Lombardo, T. S. Kulmala, A. C. Ferrari. *Quantifying defects in graphene via Raman spectroscopy at different excitation energies.* Nano Lett. **11** (2011) 3190.

[3] K. Ishioka, M. Hase, M. Kitajima, K. Ushida. *Ultrafast carrier and phonon dynamics in ion-irradiated graphite.* Appl. Phys. Lett. **78** (2001) 3965.

[4] F. Gao, F. Zhou, Y. Yao, Y. Zhang, L. Du, D. Geng, P. Wang. *Ordered assembly of platinum nanoparticles on carbon nanocubes and their application in the non-enzymatic sensing of glucose.* J. Electroanal. Chem. **803** (2017) 165.

[5] H. Uehara, Y. Uemura, T. Ogawa, K. Kono, R. Ueno, Y. Niwa, H. Nitani, H. Abe, S. Takakusagi, M. Nomura, Y. Iwasawa, K. Asakura. *In Situ back-side illumination fluorescence XAFS (BI-FXAFS) studies on platinum nanoparticles deposited on a HOPG surface as a model fuel cell: A new approach to the Pt-HOPG electrode/electrolyte interface.* Phys. Chem. Chem. Phys. **16** (2014) 13748.

[6] M.Y. Smirnov, A.V. Kalinkin, E.I. Vovk, P.A. Simonov, E.Y. Gerasimov, A.M. Sorokin, V.I. Bukhtiyarov. *Comparative XPS study of interaction of model and real Pt/C catalysts with NO_2.* Appl. Surf. Sci. **428** (2018) 972.

[7] Y. Zhou, R. Pasquarelli, T. Holme, J. Berry, D. Ginley, R. O'Hayre. *Improving PEM fuel cell catalyst activity and durability using nitrogen-doped carbon supports: observations from model Pt/HOPG systems.* J. Mater. Chem. **19** (2009) 7830.

[8] T. Kimata, S. Kato, T. Yamaki, S. Yamamoto, T. Kobayashi, T. Terai. *Platinum nanoparticles on the glassy carbon surface irradiated with argon ions.* Surf. Coat. Technol. **306** (2016) 123.

[9] A.C. Ferrari, J. Robertson. *Interpretation of Raman spectra of disordered and amorphous carbon.* Phys. Rev. B **61**, 14095 (2000).

[10] S. Prawer, F. Ninio, I. Blanchonette. *Raman spectroscopic investigation of ion- beam-irradiated glassy carbon.* J. Appl. Phys. **68**, 2361 (1990).

[11] D.G. McCulloch, S. Prawer, A. Hoffman. *Structural investigation of xenon-ion-beam-irradiated glassy carbon* Phys. Rev. B **50**, 5905 (1994).

[12] F. Tuinstra, J. L. Koenig. *Raman Spectrum of Graphite.* J. Chem. Phys. **53** (1970) 1126.

[13] D. S. Knight, W. B. White. *Characterization of diamond films by Raman spectroscopy.* J. Mater. Res. **4** (1989) 385.

[14] K. Nakamura, M. Fujitsuka, M. Kitajima. *Disorder-induced line broadening in first-order Raman scattering from graphite.* Phys. Rev. B **41**, 12260 (1990).

[15] K. Nakamura, M. Fujitsuka, M. Kitajima. *Finite size effect on Raman scattering of graphite microcrystals.* Chem. Phys. Lett. **172**, 205 (1990).

[16] J. F. Ziegler, J. P. Biersack, U. Littmack, The Stopping Range of Ions in Solids, Pergamon Press, NewYork, 1985.

[17] Y. Y. Wang, Z. H. Ni, Z. X. Shen, H. M. Wang, Y. H. Wu. *Interference enhancement of Raman signal of graphene.* Appl. Phys. Lett. **93** (2008) 043121.

[18] T. Kimata, K. Kakitani, S. Yamamoto, T. Yamaki, T. Terai, K.G. Nakamura. *Platinum nanoparticles on HOPG surface modified by 380 keV Ar^+ irradiation: TEM and Raman studies.* Radiat. Eff. Def. Sol. **175**, 433 (2020).

[19] K. Kakitani, T. Kimata, T. Yamaki, S. Yamamoto, T. Taguchi, T. Kobayashi, W. Mao, T. Terai. *The interface between platinum nanoparticle catalysts and an Ar^+-irradiated carbon support* Surf. Coat. Technol. **355** (2018) 259.

[20] A.C. Ferrari, D.M. Basko. *Raman spectroscopy as a versatile tool for studying the properties of graphene.* Nat. Nanotechnol. **8**, 235 (2013).

[21] M.A. Pimenta, G. Dresselhaus, M.S. Dresselhaus, L.G. Cançado, A. Jorio, R. Saito. *Studying disorder in graphite-based systems by Raman spectroscopy*. Phys. Chem. Chem. Phys. **9**, 1276 (2007).

[22] E. Lagzdina, D. Lingis, A. Plukis, R. Plukienė, M. Gaspariūnas, I. Matulaitienė, V. Kovalevskij, G. Niaura, V. Remeikis. *Structural investigation of RBMK nuclear graphite modified by $^{12}C^{+}$ ion implantation and thermal treatment.* Nucl. Instrum. Meth. Phys. Res. B **444**, 23 (2019).

[23] V. Zólyomi, J. Koltai, J. Kürti. *Resonance Raman spectroscopy of graphite and graphene.* Phys. Status Solidi B **248**, 2435 (2011).

[24] A. Kaniyoor, S. Ramaprabhu. *A Raman spectroscopic investigation of graphite oxide derived graphene.* AIP Adv. **2**, 032183 (2012).

[25] L.G. Cançado, A. Jorio, E.H.M. Ferreira, F. Stavale, C.A. Achete, R.B. Capaz, M.V.O. Moutinho, A. Lombardo, T.S. Kulmala, A.C. Ferrari. *Quantifying Defects in Graphene via Raman Spectroscopy at Different Excitation Energies.* Nano Lett. **11**, 3190 (2011).

[26] R. Krishna, A.N. Jones, L. McDermott, B.J. Marsden. *Neutron irradiation damage of nuclear graphite studied by high-resolution transmission electron microscopy and Raman spectroscopy.* J. Nucl. Mater. **467**, 557 (2015).

[27] R.D. Rodriguez, Z. Khan, B. Ma, A. Mukherjee, P. Meszmer, J. Kalbacova, E. Garratt, H. Shah, J. Heilmann, A.R.H. Walker, B. Wunderle, E. Sheremet, M. Hietschold, D.R.T. Zahn. *Ion Induced Defects in Graphite: A Combined Kelvin Probe and Raman Microscopy Investigation.* Phys. Status Solidi A **216**, 1900055 (2019).

[28] A. Eckmann, A. Felten, A. Mishchenko, L. Britnell, R. Krupke, K.S. Novoselov, C. Casiraghi. *Probing the nature of defects in graphene by Raman spectroscopy.* Nano Lett. **12**, 3925 (2012).

[29] I.D. Wolf. *Micro-Raman spectroscopy to study local mechanical stress in silicon integrated circuits.* Semicond. Sci. Technol. **11**, 139 (1996).

[30] R. Krishna, A.N. Jones, R. Edge, B.J. Marsden. *Residual stress measurements in polycrystalline graphite with micro-Raman spectroscopy.* Radiat. Phys. Chem. **111**, 14 (2015).

[31] A.C. Ferrari, J, Robertson. *Interpretation of Raman spectra of disordered and amorphous carbon.* Phys. Rev. B **61**, 14095 (2000).

[32] A.C. Ferrari. *Raman spectroscopy of graphene and graphite: Disorder, electron-phonon coupling, doping and nonadiabatic effects.* Solid State Commun. **143**, 47 (2007).

[33] A.C. Ferrari, J.C. Meyer, V. Scardaci, C. Casiraghi, M. Lazzeri, F. Mauri, S. Piscanec, D. Jiang, K.S. Novoselov, S. Roth, A.K. Geim. *Raman spectrum of graphite and graphene layers.* Phys. Rev. Lett. **97**, 187401 (2006).

[34] J. Hodkiewicz. *Characterizing graphene with Raman spectroscopy*. Thermoscientific Application Note; Thermo Fisher Scientific, Inc.: Madison, WI, 51946 (2010).

[35] A.C. Ferrari, S.E. Rodil, J. Robertson. *Interpretation of infrared and Raman spectra of amorphous carbon nitrides.* Phys. Rev. B **67**, 155306 (2003).

[36] K. Bogdanov, A. Fedorov, V. Osipov, T. Enoki, K. Takai, T. Hayashi, V. Ermakov, S. Moshkalev, A. Baranov. *Annealing-induced structural changes of carbon onions: High-resolution transmission electron microscopy and Raman studies.* Carbon **73**, 78 (2014).

[37] K. Nakamura, M. Kitajima. *Ion-irradiation effects on the phonon correlation length of graphite studied by Raman spectroscopy.* Phys. Rev. B **45**, 78 (1992).

[38] K. G. Nakamura, M. Kitajima. *Time-resolved Raman measurements of a graphite surface under ion irradiation.* Surf. Sci. **283**, 255 (1993).

Chapter 5

DFT calculation of the Pt cluster on defective graphite structure

5.1 Introduction

The changes in the electronic structure originating from Pt−C bonding due to the introduction of vacancies into the carbon substrates have been found by X-ray spectroscopic analysis in Chapter 3. The defective structure at the interface between Pt nanoparticles and ion-beam irradiated HOPG surface has been investigated by Raman spectroscopy in Chapter 4. In Chapter 5, DFT calculations are performed with Pt clusters on defective graphite structures to investigate the metal-supported interactions at the interface between Pt and carbon support in terms of theoretical calculations.

In a previous study [1], the specific interfacial interaction between graphite and Pt nanoparticles is reported to enhance the ORR activity of Pt nanoparticles; the Pt−C interaction, which is a metal-supported interaction, is thought to modulate the electronic state of Pt, resulting in unique catalytic properties that are not seen in single crystals. Specifically, the 5d electron orbital of Pt and the π electron orbital of C form a hybrid orbital (which may be described as the formation of a Pt−C bonding), so that the d-band center of Pt is away

from the Fermi energy than it is for Pt in bulk. In general, the adsorption energy of the adsorbed species decreases as the d-band center moves away from the Fermi energy. This relationship is called the d-band theory [2–5]. Pt nanoparticles with weakened adsorption energies of molecules and atoms are known to be highly active, and how to lower the d-band center is the key to increase the activity. Since the d-band center has an optimal value for the highest activity, it is necessary to find the value and to control the electronic structure of Pt nanoparticles.

Pt−C interactions are a partial covalent bond due to the delocalization of electrons in Pt 5d electron orbital and C π electron orbital, with a charge transfer between Pt and C. Although the quantitative correlation between Pt−C interactions and catalytic activity has not been found, it is empirically known that increased Pt−C interactions are effective in improving catalytic activity [6, 7]. In order to increase the Pt−C interactions, it has been suggested that a strong anchor site at the Pt/C interface should be created by surface modification of carbon substrates [7].

For increasing the Pt−C interactions, the model of the Pt nanoparticles on the graphene having lattice defects has been considered and calculated by computer simulations [8–10]. The overview is described below.

1. Point defects in graphene act as strong binding traps for Pt clusters, the inducting pre-existing point defects in graphene supports could provide an easy method for synthesizing robust carbon-supported Pt nanocatalysts.
2. The formation of strong bonds with the carbon substrate, which is Pt−C bonding, potentially influences the strain in a cluster.
3. Electronic structure analysis revealed charge transfer from Pt clusters to the graphene substrate, suggested a positive correlation between the strength of binding to the defect and the extent of charge transferred.

4. Stronger binding of the Pt cluster to the graphene substrate appears to lead to a greater downshift of the cluster d-band center.

As described above, using of the carbon support having lattice defects is helpful for preparing the highly active Pt catalysts. However, since there is an optimal value of d-band center for the highest activity, the amount and type of lattice defects must be controlled when introducing them into the carbon substrate. Therefore, the ion beam with the parameters of ion species, fluence, and energy can be a strong tool for introducing lattice defects into the carbon support.

In Chapter 5, a model of Pt cluster on the graphitic structures with lattice defects formed by ion-beam irradiation is studied theoretically. The aforementioned previous work deals with calculations for Pt clusters on single-phase graphene with point defects, but not with composite defects and defects over multiple layers that would be introduced by ion-beam irradiation. By constructing a model and performing DFT calculations, the influence of lattice defects in the graphitic structure on the electronic state of the Pt cluster is investigated [11, 12].

5.2 DFT calculation

All the DFT calculations were performed using the Vienna ab-initio Simulation Package (VASP). VASP is a first-principles calculation program developed at the University of Vienna [13, 14]. VASP implements a potential library by projector augmented wave (PAW), which expresses the wave function by superposition of the basis function of plane waves and calculates the electronic structure based on the DFT. The PAW is a generalization of the pseudopotential and linear augmented-plane-wave methods and allows for density functional theory calculations to be performed with greater computational efficiency [15].

VASP is one of the most commonly used packages of first-principles calculation software and is also often used for simulating the physical properties of platinum nanoparticles on carbon supports [16].

The NCAR, POSCAR, POTCAR, and KPOINTS files are necessary as input information on VASP. The role of each file is described below [17]. These files are prepared to calculate the model of Pt cluster on defective graphite supports.

1. INCAR is the central input file of VASP. It determines 'what to do and how to do it', and contains a relatively large number of parameters.
2. The POSCAR file contains the lattice geometry and the ionic positions.
3. The POTCAR file contains the pseudopotential for each atomic species used in the calculation.
4. The file KPOINTS must contain the k-point coordinates and weights or the mesh size for creating the k-point grid.

5.2.1 Calculation setup

The projector augmented wave method combined with a plane-wave basis set and cutoff energy of 400 eV was used to describe the core and valence electrons. The revised Perdew-Burke-Ernzerhof (RPBE) form of the generalized gradient approximation was implemented in all the calculations. A conjugate gradient algorithm was used to relax ions into their ground states. The ions were allowed to relax, but the unit cell and its shape were kept constant. The energy converge criteria were set to 10^{-4} eV for the self-consistent calculations with a gamma-center $9\times9\times1$ k-mesh. To accelerate the electronic convergence, Gaussian smearing of the Fermi surface was employed with a smearing width of 0.1 eV. All the periodic slabs had a vacuum spacing of 18 Å.

5.2.2 Calculation model

When the materials with graphite structure are irradiated by ion-beams, the generation of single vacancy (SV) [18] and double vacancy (DV) [19] has been predicted by molecular dynamics simulations [20]. TRIM calculations of Ar^+ irradiation to carbon support indicated the LET is distributed in the depth direction (c-axis direction). Therefore, the SV and DV introduced into the carbon supports by ion-irradiation may be present not only in the first layer of graphite structure but also in the second layer and beyond.

Here, the model of the irradiated carbon substrate and Pt nanoparticles was indicated in Figure 5.1(a). The carbon substrate was modeled as three layers of graphene; each layer had a 5×5 structure [21–23]. To simulate the irradiation defects, vacancies with different configurations ((b) single vacancy only in the upper layer (SV), (c) double vacancies only in the upper layer (DV), (d) single vacancies in the upper 2 layers (2SV), and (e) double vacancies in the upper 2 layers (2DV)) were introduced to the upper two layers. An icosahedral Pt_{13} cluster was allowed to interact with the carbon atoms [24–26]. One face of the icosahedron was in contact with the graphene, and the face center of gravity was centered at each vacancy.

The graphite structures used in the calculations were obtained by multiplying the basic structure of graphite downloaded from the National Institute for Materials Science's inorganic materials database [27] by a factor of 5×5 in the horizontal direction (a-axis and b-axis plane) and a factor of 1.5 in the depth direction (c-axis direction). The number of carbon atoms in one layer is 50 atoms. This model of graphite layers with this shape has been used in previous studies to calculate the interaction between Pt nanoparticles and graphite [22]. The size of the layer, which is the length of the diagonal of the parallelogram-shaped layer is 2.13 nm.

On the other hand, Pt_{13} cluster is used in the model as shown in Figure 5.1(a).

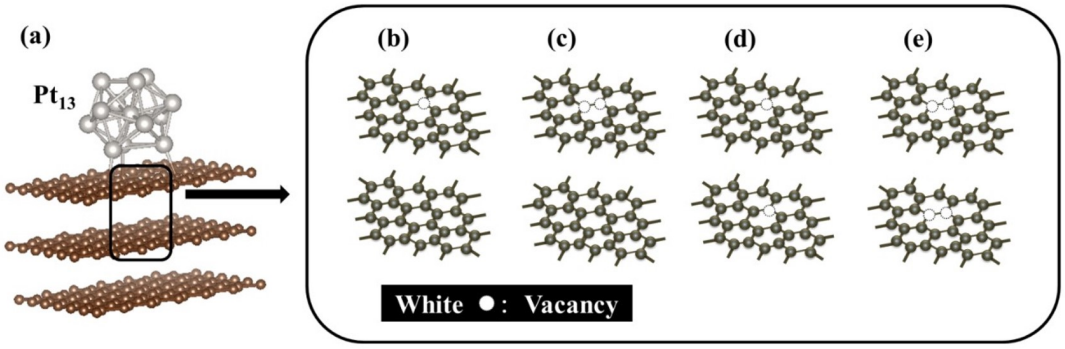

Fig. 5.1: (a) Calculation models of the irradiated carbon support and Pt nanoparticles. The interface was modeled as an icosahedral Pt_{13} cluster and three layers of graphene with (b) SV, (c) DV, (d) 2SV and (e) 2DV. This figure is obtained from Fig. S5 of the preprint, T. Kimata et al., ChemRxiv. Preprint. (2017).

Park *et al.* suggested that the Pt deposited on the carbon surface is neither a single atom nor a bulk, and that it is reasonable to model it as a cluster consisting of several Pt atoms [28]. For many metal atoms, the number of constituent atoms that can form a stable structure as a cluster is fixed and is called the magic number [29, 30]. In the case of Pt_n, it is known to have a relatively stable structure at n=13, 38 and 55, and Aprá reported each structure [31]. The Pt_{13} cluster is used in these calculations because a smaller number of Pt atoms would be more appropriate to study the effect of the interfacial structure on the electronic state of the Pt nanoparticles. Pt_{13} is the structure used in many DFT calculation papers on Pt catalysts [24, 26]. The basic model of Pt_{13} was also downloaded from NIMS's inorganic materials database [27].

5.3 Results and discussion

DFT calculations were performed to investigate the interfacial effect of the irradiation defects in the carbon support on the electronic structure of the Pt nanoparticles.

The difference between the charge density of the Pt_{13} cluster on the carbon

substrate and the sum of its separated constituents (cluster and substrate) was calculated by

$$\Delta\rho = \rho_{Pt-C} - \rho_{Pt} - \rho_{C}, \tag{5.1}$$

where $\Delta\rho$ is differential charge density distribution. Fig. 5.2 shows the isosurfaces of the charge difference in the case when the substrate structure was the 2DV. Charge accumulation and depletion mainly occurred in the vicinity of the support-cluster interface; this tendency was clearly observed for all the support structures including the PG. This suggests that the Pt atoms at the interface were mainly involved in the charge transfer between the Pt_{13} cluster and the carbon support.

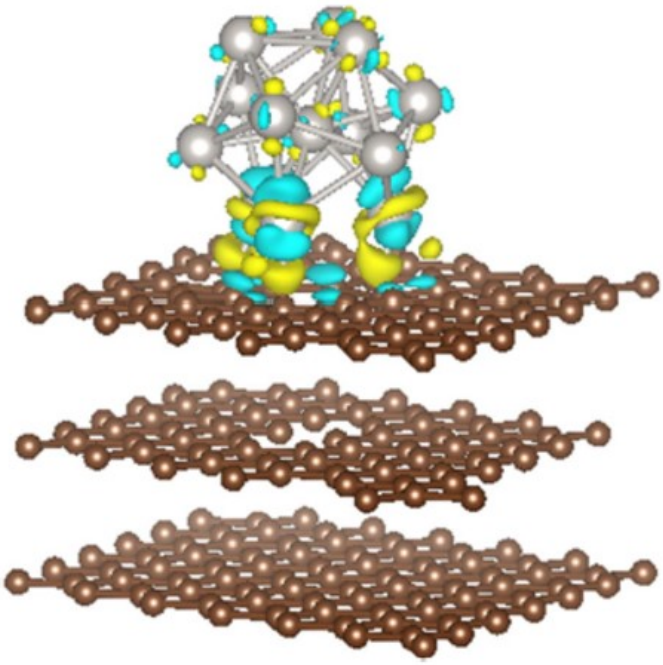

Fig. 5.2: Isosurfaces of the charge density difference of a Pt_{13} cluster on the graphite with the 2DV. The density increases in the yellow regions and decreases in the blue regions. The isosurface value is 50 e/nm^3. This figure is obtained from Fig. 4 of the paper, K. Kakitani et al., Surf. Coat. Technol. 355, 259 (2018).

Next, the density of state (DOS) of Pt atoms in Pt_{13} cluster was calculated and shown in Fig. 5.3. Although the average of Pt_{13} atoms showed no significant

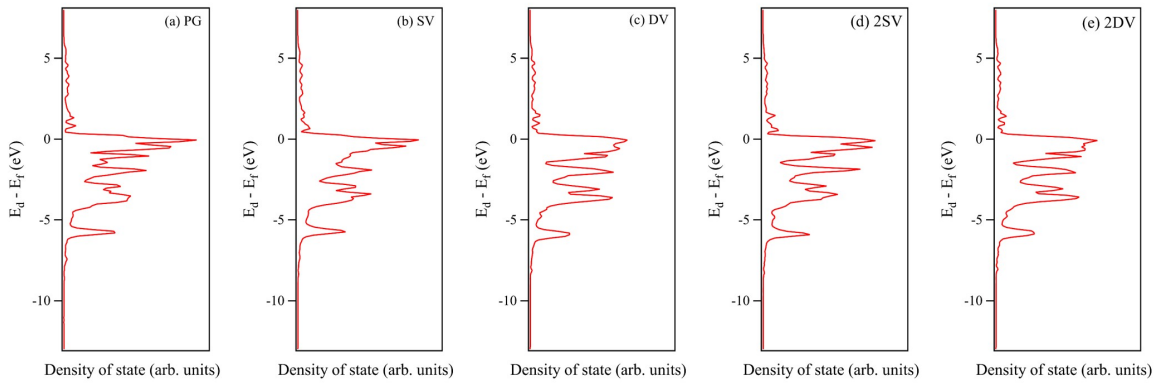

Fig. 5.3: DOS of a Pt_{13} cluster on each graphite structure.

change in DOS regardless of the type of defect, the average of Pt_3 atoms near the Pt/C interface showed a change in DOS. The change in the band structure can be attributed to the charge transfer from Pt to C. The average energy of the d-states is called d-band center, and is known as a parameter that correlates with the reactivity of metals and oxygen [16]. The d-band center, ϵ_d, is obtained by

$$\epsilon_d = \frac{\int_{-\infty}^{E_f} E \cdot g_d(E) dE}{\int_{-\infty}^{E_f} g_d(E) dE}, \tag{5.2}$$

where $g_d(E)$ and E_f are density of state and Fermi level, respectively [3].

After structural relaxation, the d-band center over the Pt atoms for each model was calculated (Table 5.1). Compared to the case of the pristine graphite, when the Pt_{13} cluster was supported on the multiple vacancies (defined as defective structures with more than two lattice vacancies), ϵ_d became lower by 0.05 eV or more. It is broadly accepted that ϵ_d correlates with the chemical reactivity of the Pt surface [3], and the bonding of oxygen to the Pt surface has been reported to weaken with a lower ϵ_d value [32, 33]. Therefore, the lower ϵ_d value indicates that the multiple vacancies of the carbon support probably weaken the bonding of oxygen to the Pt clusters. Such low oxygen-adsorption ability would originate from the Pt-carbon support interaction involving the electron transfer between the Pt d-orbitals and the carbon π-sites. Thus, the suppression of the Pt oxidation can be ascribed to the Pt$-$C bonding between Pt atoms and the

multiple vacancies of the carbon support. This result suggests that the weak adsorption of oxygen on the irradiated sample observed in the XAFS measurements (Chapter 3).

Table 5.1: Average d-band center values of the Pt_{13}on the substrates having different defective structures. This table is obtained by modifying Table 1 of the preprint, T. Kimata et al., ChemRxiv. Preprint. (2017).

substrate	ϵ_d of 13 atoms (eV)
Pristine graphene (PG)	-2.36
Single vacancy only in the upper layer (SV)	-2.34
Double vacancies only in the upper layer (DC)	-2.43
Single vacancies in the upper 2 layers (2SV)	-2.41
Double vacancies in the upper 2 layers (2DV)	-2.41

5.4 Summary

DFT calculations were performed with Pt_{13} cluster on defective graphite structures to investigate the influence of the defective structure in carbon support on the electronic state of Pt atoms, in Chapter 5. The results of the DFT calculation indicated the lower ϵ_d value on the multiple vacancies. The lower ϵ_d value explains the suppressed oxidation of the Pt nanoparticles, which is known to enhance the ORR activity. The formation of the $Pt-C$ bonding promoted by the ion-beam-induced lattice defects would be the origin of the higher activity.

References

[1] T. Kondo, Y. Iwasaki, Y. Honma, Y. Takagi, S. Okada, J. Nakamura. *Formation of non-bonding π electronic states of graphite due to Pt−C hybridization.* Phys. Rev. B **80**, 233408 (2009).

[2] B. Hammer, J.K. Norskov. *Why gold is the noblest of all the metals.* Nature **376**, 238 (1995).

[3] B. Hammer, J.K. Nørskov. *Electronic factors determining the reactivity of metal surfaces.* Surf. Sci. **343**, 211 (1995).

[4] M. Mavrikakis, B. Hammer, J.K. Nørskov. *Effect of strain on the reactivity of metal surfaces.* Phys. Rev. Lett. **81**, 2819 (1998).

[5] J.R. Kitchin, J.K. Nørskov, M.A. Barteau, J.G. Chen. *Trends in the chemical properties of early transition metal carbide surfaces: A density functional study.* Catalysis Today **105**, 66 (2005).

[6] X. Yu S. Ye. *Recent advances in activity and durability enhancement of Pt/C catalytic cathode in PEMFC: Part I. Physico-chemical and electronic interaction between Pt and carbon support, and activity enhancement of Pt/C catalyst.* J. Power Sources **172**, 133 (2007).

[7] X. Yu S. Ye. *Recent advances in activity and durability enhancement of Pt/C catalytic cathode in PEMFC: Part II: Degradation mechanism and durability enhancement of carbon supported platinum catalyst.* J. Power Sources **172**, 145 (2007).

[8] D.-H. Lim, J. Wilcox. *DFT-based study on oxygen adsorption on defective graphene-supported Pt nanoparticles.* J. Phys. Chem. C **115**, 22742 (2011).

[9] D.-H. Lim, J. Wilcox. *Mechanisms of the oxygen reduction reaction on defective graphene-supported Pt nanoparticles from first-principles.* J. Phys. Chem. C **116**, 3653 (2012).

[10] I. Fampiou, A. Ramasubramaniam. *Binding of Pt nanoclusters to point defects in graphene: Adsorption, morphology, and electronic structure.* J. Phys. Chem. C **116**, 6543 (2012).

[11] K. Kakitani, T. Kimata, T. Yamaki, S. Yamamoto, T. Taguchi, T. Kobayashi, W. Mao, T. Terai. *The interface between platinum nanoparticle catalysts and an Ar^{+}-irradiated carbon support.* Surf. Coat. Technol. **355**, 259 (2018).

[12] T. Kimata, K. Kakitani, S. Yamamoto, I. Shimoyama, D. Matsumura, A. Iwase, W. Mao, T. Kobayashi, T. Yamaki, T. Terai. *Activity enhancement of platinum oxygen-reduction electrocatalysts using ion-beam induced defects.* ChemRxiv. Preprint. (2017).

[13] G. Kresse, J. Furthmler. *Efficiency of ab-initio total energy calculations for metals and semiconductors using a plane-wave basis set.* Comput. Mater. Sci. **6**, 15 (1996).

[14] G. Kresse, D. Joubert. *From ultrasoft pseudopotentials to the projector augmented-wave method.* Phys. Rev. B **59**, 1758 (1999).

[15] P. E. Blöchl. *Projector augmented-wave method.* Phys. Rev. B **50**, 17953 (1994).

[16] T. Holme, Y. Zhou, R. Pasquarelli, R. O'Hayre. *First principles study of doped carbon supports for enhanced platinumcatalysts.* Phys. Chem. Chem. Phys. **12**, 9461, (2010).

[17] VASP the GUIDE, (https://cms.mpi.univie.ac.at/vasp/vasp/vasp.html).

[18] M.M. Ugeda, I. Brihuega, F. Guinea, J.M. Gómez-Rodríguez. *Missing Atom as a Source of Carbon Magnetism.* Phys. Rev. Lett. **104**, 096804 (2010).

[19] M.M. Ugeda, I. Brihuega, F. Hiebel, P. Mallet, J.-Y. Veuillen, J.M. Gómez-Rodríguez, F. Ynduráin. *Electronic and structural characterization of divacancies in irradiated graphene.* Phys. Rev. B **85**, 121402(R) (2012).

[20] O. Lehtinen, J. Kotakoski, A.V. Krasheninnikov, A. Tolvanen, K. Nordlund, J. Keinonen. *Effects of ion bombardment on a two-dimensional target: Atomistic simulations of graphene irradiation.* Phys. Rev. B **81**, 153401 (2010).

[21] G. Ramos-Sanchez, P. B. Balbuena. *Interactions of platinum clusters with a graphite substrate.* Phys. Chem. Chem. Phys. **15**, 11950 (2013).

[22] J. Ma, A. Habrioux, C. Morais, A. Lewera, W. Vogel, Y. Verde-Gómez, G. Ramos-Sanchez, P. B. Balbuena, N. Alonso-Vante. *Spectroelectrochemical probing of the strong*

interaction between platinum nanoparticles and graphitic domains of carbon. ACS Catal. **3**, 1940 (2013).

[23] Y. Tian, Y.-J. Liu, J.-X. Zhao, Y.-H. Ding. *High stability and superior catalytic reactivity of nitrogen-doped graphene supporting Pt nanoparticles as a catalyst for the oxygen reduction reaction: a density functional theory study*. RSC Adv. **5**, 34070 (2015).

[24] Y. Okamoto. *Density-functional calculations of icosahedral M_{13} (M=Pt and Au) clusters on graphene sheets and flakes*. Chem. Phys. Lett. **420**, 382 (2006).

[25] D. Higgins, M. A. Hoque, M. H. Seo, R. Wang, F. Hassan, J.-Y. Choi, M. Pritzker, A. Yu, J. Zhang, Z. Chen. *Development and simulation of sulfur-doped graphene supported platinum with exemplary and activity towards oxygen reduction*. Adv. Funct. Mater. **24** 4325 (2014).

[26] N. T. Cuong, A. Fujisawa, T. Mitani, D. H. Chi. *Effect of carbon supports on Pt nanocluster catalyst*. Comput. Mater. Sci. **44**, 163 (2008).

[27] Inorganic Material Database, (http://crystdb.nims.go.jp/).

[28] N. Park, D. Sung, S. Lim, S. Moon, S. Hong. *Realistic adsorption geometries and binding affinities of metal nanoparticles onto the surface of carbon nanotubes*. Appl. Phys. Lett. **94**, 073105 (2009).

[29] Y. Yamada, A.W. Castleman Jr.. *The magic numbers of metal and metal alloy clusters*. J. Chem. Phys. **97**, 4543 (1992).

[30] M. Sakurai, K. Watanabe, K. Sumiyama, K. Suzuki. *Magic numbers in transition metal (Fe, Ti, Zr, Nb, and Ta) clusters observed by time-of-flight mass spectrometry*. J. Chem. Phys. **111**, 235 (1999).

[31] E. Aprá, A. Fortunelli. *Density-Functional Calculations on Platinum Nanoclusters: Pt_{13}, Pt_{38}, and Pt_{55}*. J. Phys. Chem A **107**, 2934 (2003).

[32] V. Stamenkovic, B. S. Mun, K. J. Mayrhofer, P. N. Ross, N. M. Markovic, J. Rossmeisl, J. Greeley, J. K. Nørskov. *Changing the activity of electrocatalysts for oxygen reduction by tuning the surface electronic structure*. Angew. Chem. **118**, 2963 (2006).

[33] F.H.B. Lima, J. Zhang, M.H. Shao, K. Sasaki, M.B. Vukmirovic, E.A. Ticianelli, R.R. Adzic. *Catalytic Activity−d-Band Center Correlation for the O_2 Reduction Reaction on Platinum in Alkaline Solutions*. J. Phys. Chem. C **111**, 404 (2007).

Chapter 6

Ultrafast dynamics and coherent control of optical phonons

6.1 Introduction

The time scale of ultrafast phenomena such as atomic and electronic motions in matter is picoseconds (ps) to attoseconds (as) order. The phenomena are faster than the temporal response of electronic devices, as shown in Fig. 6.1; *e.g.*, a heartbeat $\sim$1 second (s), a blink of eye $\sim$150 millisecond (ms), a shutter speed of camera $\sim$2 microsecond (μs), the throughput of a general computer for nanosecond (ns), and chemical reaction and scattering between electrons and phonons for as to ps order. The changes in optical intensity occurring on a time scale of approximately 1 ns can be measured electrically using a photodiode and an oscilloscope. However, the time-resolved measurement using femtosecond optical pulses is necessary to detect the dynamics of ultrafast phenomena. Femtosecond optical pulses excite the in-phase lattice vibrations in solids which are called coherent phonon. The dynamic processes of their generation and relaxation are affected by many factors such as phonon symmetry, electronic band structure of the solid, photoexcitation density, surface condition, etc. Thus, ultrafast spectroscopy is a strong tool to investigate the details

of the electronic state of materials and chemical reactions.

In Chapter 6, the coherent control theory of optical phonons is modified for large detuning case such as diamond, as a first step to investigate the effect of ion-beam-induced defects on the ultrafast dynamics in carbon materials.

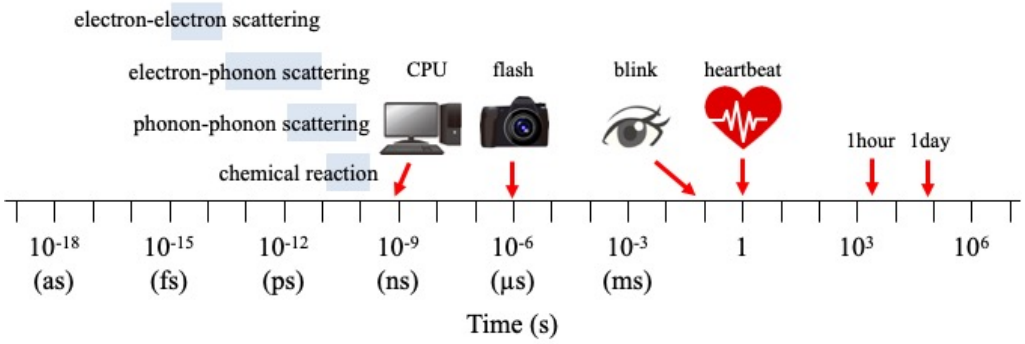

Fig. 6.1: Typical time-scales of phenomena.

6.1.1 Coherent phonon

Phonon is a quantum of lattice vibrations and is a boson as well as a photon. Usually, phonons are randomly oscillation, incoherent, in thermal equilibrium as shown in Fig. 6.2 (a). Then the average of displacement of the atoms is almost zero in time and space because they have each deferent wave vectors and frequencies. In contrast, when an ultrashort optical pulse with a duration much shorter than an oscillation period of optical phonons is irradiated on materials, the optical phonons are excited impulsively and coherently (Fig. 6.2 (b)). These excited-phonons are called coherent phonons. Oscillation of the induced optical phonons is detected via a transient change in reflectivity or transmissivity. Coherent phonons have been observed in several materials such as metals [1], semimetals [2], semiconductors [3, 4], and superconductors [5].

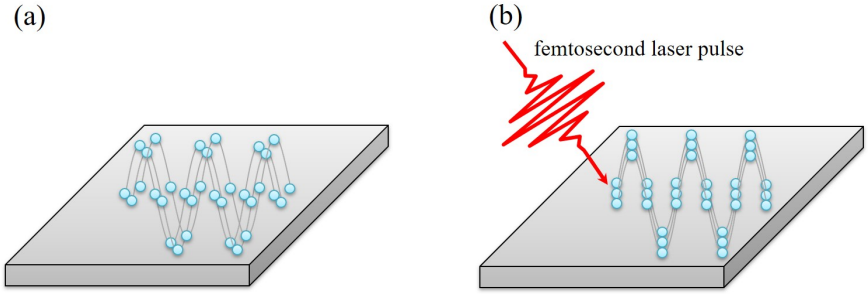

Fig. 6.2: Schematic of (a) incoherent phonon and (b) coherent phonon generation.

6.1.2 Ultrafast spectroscopy

Pump-probe measurement is known as the simplest experimental technique of ultrafast spectroscopy used to study ultrafast electronic dynamics. The coherent phonons are excited and measured via pump-probe transmission or reflection measurements, as shown in Fig. 6.3. In this technique, an ultrashort laser pulse is split into two portions; the first pulse is used to excite the sample, generating a non-equilibrium state, and the second pulse is used to monitor the pump-induced changes in the optical constants of the sample such as reflectivity or transmission. Measuring the changes in the optical constants as a function of the time delay between the arrival of the pump and probe pulses yields information about the electronic structure in the sample.

In this study, a dual pump-probe method is used to excite the sample using two phase-locked pump pulses. Figure 6.4 shows a schematic of the method. This method not only measures the transient changes in the sample by controlling the time interval between the pump and probe pulses but also controls the excited state by manipulating the time interval for the two-pump pulses.

6.1.3 Coherent control

Coherent control is a technique to manipulate quantum states in matter using optical pulses [6–8] and applied to electronic states, spins, molecular vibrations, and phonons [9–17]. The coherent control of optical phonons has been widely

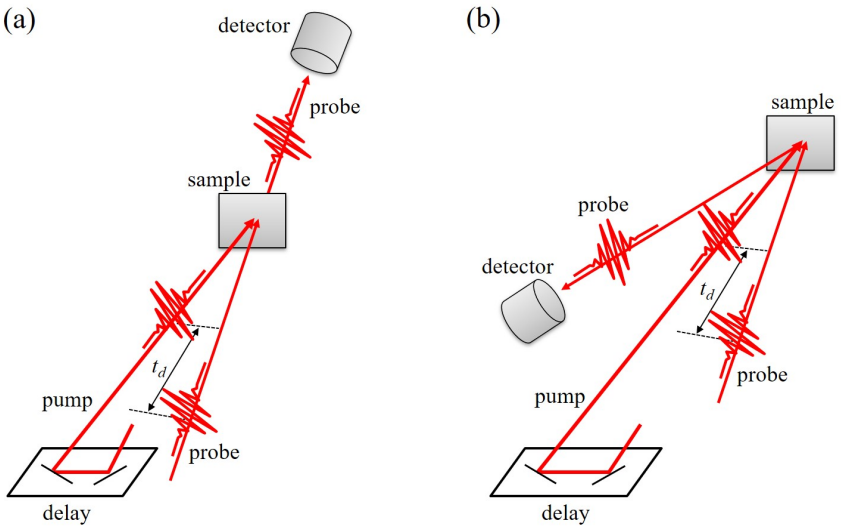

Fig. 6.3: Schematic of pump-probe spectroscopy: (a) transmittance measurement, (b) reflectance measurement.

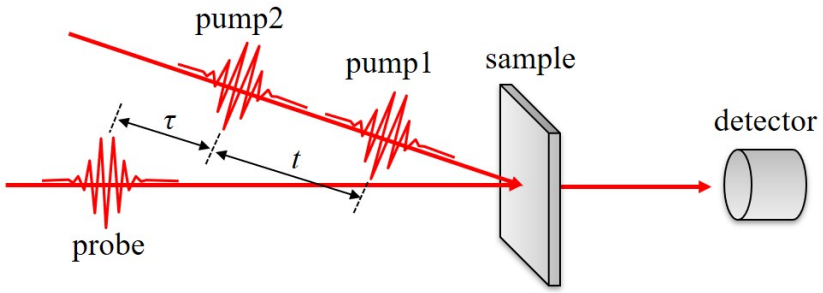

Fig. 6.4: Schematic of a dual pump-probe method.

achieved in various materials such as semiconductors, semimetals, superconductors, topological materials, strongly-correlated materials, and dielectric materials [18–24]. In a theoretical study, a theory of the coherent control of optical phonons by double-pulse excitation had been developed based on the simple quantum mechanical model with two-electronic bands and shifted harmonic oscillators [25, 26]. Sasaki *et al.* demonstrated the coherent control experiment on the optical phonons in a single crystal of diamond and analyzed the data by using the developed theory [27].

The optical phonon in diamond has high frequency (approximately 40 THz) and is expected to be used as a qubit operating at room temperatures [28–31]. The coherent optical phonons in diamond have been studied using femtosecond optical pulses and its generation mechanism has also been discussed with quantum mechanical calculations [26, 27, 32–35]. Sasaki *et al.* have demonstrated the coherent control of amplitude and phase of the coherent optical-phonon oscillation in diamond using a pair of sub-10-fs infrared pulses at delays between 230 and 270 fs, in which two pump pulses were well separated [27]. The observed behavior of the amplitude and phase were well reproduced as a simple interference between two phonon oscillations by the developed theory.

However, it is very important to study the time region around where two optical pulses are overlapped, because a sign of interference in electron-phonon coupled states [36–41], which could not be reproduced by a classical mechanics, appears in this region. The difference of the interference patterns for the impulsive absorption process and the impulsive stimulated Raman scattering (ISRS) process has been clearly shown in a GaAs crystal [18]. In order to study in the large detuning conditions and a non-Gaussian pulse shape, the modification of the theory should be required.

In Chapter 6, I modify the theory to calculate the large detuning case without using a rotating-wave approximation and take the frequency chirping and non-

Gaussian pulse shape into consideration. The coherent control of amplitude of the 40-THz optical phonons in diamond was performed by using a pair of infrared pulses at pump-pump delays between -10 and 120 fs, then the experimental result was analyzed using the modified theory based on the quantum mechanical model.

6.2 Theoretical model

6.2.1 Coherent phonon generation

At first, I describe the model and Hamiltonian for coherent phonon generation. Nakamura *et al.* previously calculated the generation of the coherent phonons using a simple model with two-electronic levels and shifted harmonic oscillators as shown in Fig. 6.5 [25, 27, 42]. The Hamiltonian is given by

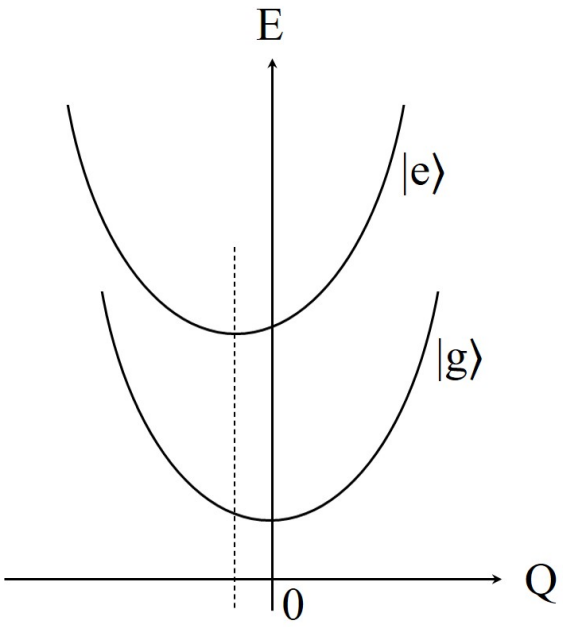

Fig. 6.5: Schematic of the model potential consisting of two electronic states and shifted harmonic potentials.

$$H_0 = H_g|g\rangle\langle g| + (\epsilon + H_e)|e\rangle\langle e|, \tag{6.1}$$

$$H_g = \hbar\omega b^\dagger b, \tag{6.2}$$

$$H_e = \hbar\omega b^\dagger b + \alpha\hbar\omega(b^\dagger + b), \tag{6.3}$$

where the state vector $|g\rangle$ denotes the electronic ground state of the crystal, and $|e\rangle$ denotes the electronic excited state with the excitation energy ϵ. In the case of a diamond, $|e\rangle$ corresponds representatively to the electronic states above the direct bandgap, and ϵ is approximately equal to the direct bandgap energy 7.3 eV [43, 44]. The Hamiltonian H_g and H_e are the phonon Hamiltonians in the subspace $|g\rangle$ and $|e\rangle$. $b^\dagger$ and b denote creation and annihilation operators for the phonon. The energy of the interaction mode $\hbar\omega$ is equal to the optical phonon energy at Γ point, where ω is the phonon frequency. α represents the electron-phonon coupling. Thus, the model Hamiltonian of the electron-phonon system is given by

$$H_0 = \hbar\omega b^\dagger b|g\rangle\langle g| + \left(\epsilon + \hbar\omega b^\dagger b + \alpha\hbar\omega(b + b^\dagger)\right)|e\rangle\langle e|. \tag{6.4}$$

Next, the dipole interaction between the materials and the incident light is assumed and the interaction Hamiltonian is represented by

$$\begin{aligned} H_I(t) &= \mu E(t)(|g\rangle\langle e| + |e\rangle\langle g|) \\ &= \mu E_0 f(t)\left(e^{-i\Omega t} + e^{i\Omega t}\right)(|g\rangle\langle e| + |e\rangle\langle g|) \\ &\approx \mu E_0 f(t)\left(e^{-i\Omega t}|e\rangle\langle g| + e^{i\Omega t}|g\rangle\langle e|\right), \end{aligned} \tag{6.5}$$

where the optical pulse $E(t)$ is

$$E(t) = E_0 f(t)\left(e^{-i\Omega t} + e^{i\Omega t}\right). \tag{6.6}$$

The μ is the transition dipole moment, E_0 and $f(t)$ are an amplitude and envelope of the electric field of the pulse, respectively. Ω is the angular frequency of the light. The rotating wave approximation (RWA) is used on the transformation of (6.5). The operator $|e\rangle\langle g|$ causes a transition from the electronic ground state $|g\rangle$ to the excited state $|e\rangle$.

The model Hamiltonian H_0 is not time dependent and the interaction Hamiltonian H_I is time dependent. The system Hamiltonian is

$$H(t) = H_0 + H_I(t). \tag{6.7}$$

The time evolution of the electron-phonon coupled state is obtained by solving the time-dependent Schrödinger (TDS) equation as given below:

$$i\hbar\frac{d}{dt}|\psi(t)\rangle_S = H|\psi(t)\rangle_S. \tag{6.8}$$

Details for the calculation of the density operator and the second-order perturbation were described elsewhere [18, 42].

6.2.2 Four-level model and double-sided Feynman diagram of ISRS process

Here, let us consider the ISRS process for exciting the coherent phonons in the electronic ground state [25, 42]. The coherent optical phonons should be excited by the ISRS process at an off-resonant condition because the energy of the optical pulses (around 1.5 eV) is well below the direct bandgap (7.3 eV) of diamond [43, 44]. Figure 6.6 shows the four-level model and double-sided Feynman diagram of the ISRS process with the $|g,0\rangle \rightarrow |e,1\rangle \rightarrow |g,1\rangle$ and $|g,0\rangle \rightarrow |e,0\rangle \rightarrow |g,1\rangle$ transitions. Each transition is represented as path (a) and path (b) in Fig. 6.6, and the energy of each level is set as shown in Fig. 6.6 (c). The final state $|g,1\rangle\langle g,0|$ is in the electronic ground state with vibrational polarization.

In the path (a), $|g,0\rangle$ changes to $|e,1\rangle$ at time t'' via the dipole interaction with the incident pulse and the electron-phonon coupling. The total interaction causes the multiplicative coefficient

$$\alpha\left(\frac{\mu E(t'')}{i\hbar}\right) = \alpha\left(\frac{\mu E_0}{i\hbar}\right) f(t'')e^{-i\Omega t''}. \tag{6.9}$$

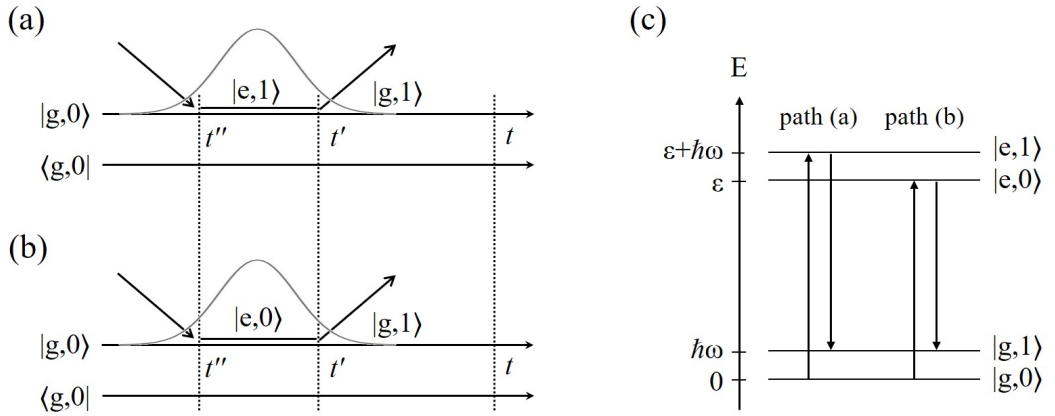

Fig. 6.6: Schematic of the ISRS process ((a) passes through $|e,1\rangle$ state and (b) passes through $|e,0\rangle$ state) and (c) four-level model. Time flows from the left to the right. The upper side of the diagram shows an envelope of the optical pulse. Interaction between the optical pulse and the systems occurs at the time t'' and t'.

At time between t'' and t', the state $|e,1\rangle\langle g,0|$ has a time evolution factor of

$$e^{-\frac{i}{\hbar}(\epsilon+\hbar\omega)(t'-t'')}. \tag{6.10}$$

At time t', $|e,1\rangle$ changes to $|g,1\rangle$ via the dipole interaction with the incident pulse, the total interaction represents the multiplicative coefficient

$$\left(\frac{\mu E^*(t')}{-i\hbar}\right) = \left(\frac{\mu E_0}{-i\hbar}\right) f(t')e^{i\Omega t'}, \tag{6.11}$$

because the light goes out from the material system. After time t', the state $|g,1\rangle\langle g,0|$ has a time evolution factor of

$$e^{-i\omega(t-t')}. \tag{6.12}$$

The time evolution of the density matrix for the path (a) is gotten as

$$\rho_1(t:t'',t') = \alpha\left(\frac{\mu E_0}{\hbar}\right)^2 f(t'')f(t')e^{-i\left(\frac{\epsilon}{\hbar}-\Omega\right)(t'-t'')}e^{-i\omega(t-t'')}|g,1\rangle\langle g,0|. \tag{6.13}$$

The density operator $\rho_1(t)$ is obtained by integrating $\rho_1(t:t'',t')$ over t'' and t'

as:

$$\rho_1(t) = \alpha \left(\frac{\mu E_0}{\hbar}\right)^2 \int_{-\infty}^{t} dt' \int_{-\infty}^{t'} dt'' f(t'') f(t') e^{-i\left(\frac{\epsilon}{\hbar}-\Omega\right)(t'-t'')} e^{-i\omega(t-t'')} \cdot |g,1\rangle\langle g,0|. \tag{6.14}$$

In the path (b), at the t'', $|g,0\rangle$ changes to $|e,0\rangle$ via the dipole interaction with the incident pulse, the interaction causes the multiplicative coefficient

$$\left(\frac{\mu E(t'')}{i\hbar}\right) = \left(\frac{\mu E_0}{i\hbar}\right) f(t'') e^{-i\Omega t''}. \tag{6.15}$$

At time between t'' and t', the state $|e,0\rangle\langle g,0|$ has a time evolution factor of

$$e^{-\frac{i}{\hbar}\epsilon(t'-t'')}. \tag{6.16}$$

At time t', $|e,0\rangle$ changes to $|g,1\rangle$ via the dipole interaction with the incident pulse and the electron-phonon coupling. The total interaction causes the multiplicative coefficient

$$-\alpha \left(\frac{\mu E^*(t')}{-i\hbar}\right) = -\alpha \left(\frac{\mu E_0}{-i\hbar}\right) f(t') e^{i\Omega t'}. \tag{6.17}$$

The ground state harmonic potential shits in the $-\alpha$ direction. After time t', the state $|g,1\rangle\langle g,0|$ has a time evolution factor of

$$e^{-i\omega(t-t')}. \tag{6.18}$$

The time evolution of the density matrix for the path (b) is gotten as

$$\rho_2(t:t'',t') = -\alpha \left(\frac{\mu E_0}{\hbar}\right)^2 f(t'') f(t') e^{-i\left(\frac{\epsilon}{\hbar}-\Omega\right)(t'-t'')} e^{-i\omega(t-t')} |g,1\rangle\langle g,0|. \tag{6.19}$$

The density operator $\rho_2(t)$ is obtained by integrating $\rho_2(t:t'',t')$ over t'' and t' as:

$$\rho_2(t) = -\alpha \left(\frac{\mu E_0}{\hbar}\right)^2 \int_{-\infty}^{t} dt' \int_{-\infty}^{t'} dt'' f(t'') f(t') e^{-i\left(\frac{\epsilon}{\hbar}-\Omega\right)(t'-t'')} e^{-i\omega(t-t')} \cdot |g,1\rangle\langle g,0|. \tag{6.20}$$

The total density matrix $\rho(t)$ is obtained by

$$\rho(t) = \rho_1(t) + \rho_2(t) + H.c.. \tag{6.21}$$

In the case of resonance condition ($\epsilon/\hbar - \Omega = 0$), $\rho(t)$ is obtained to be

$$\begin{aligned}\rho(t) =& \alpha \left(\frac{\mu E_0}{\hbar}\right)^2 \int_{-\infty}^{t} dt' \int_{-\infty}^{t'} dt'' f(t'') f(t') \\ & \cdot \left(e^{-i\omega(t-t'')} - e^{-i\omega(t-t')}\right) |g,1\rangle\langle g,0| + H.c..\end{aligned} \tag{6.22}$$

In the stimulated Raman scattering process, phonons are excited in the electronic ground state, and the phonon coordinate operator Q_R is expressed by

$$Q_R = \sqrt{\frac{\hbar}{2\omega}}(b + b^\dagger). \tag{6.23}$$

Therefore, the expectation value of the phonon amplitude on the ISRS process is calculated by

$$\begin{aligned}\langle Q_R(t)\rangle =& Tr\left\{Q_R \rho(t)\right\} \\ =& \alpha \left(\frac{\mu E_0}{\hbar}\right)^2 \sqrt{\frac{\hbar}{2\omega}} \int_{-\infty}^{t} dt' \int_{-\infty}^{t'} dt'' f(t'') f(t') \\ & \cdot \left(e^{-i\omega(t-t'')} - e^{-i\omega(t-t')}\right) \qquad (6.24) \\ =& 2\alpha \left(\frac{\mu E_0}{\hbar}\right)^2 \sqrt{\frac{\hbar}{2\omega}} \int_{-\infty}^{t} dt' \int_{-\infty}^{t'} dt'' f(t'') f(t') \\ & \cdot \left(\cos\omega(t-t'') - \cos\omega(t-t')\right). \qquad (6.25)\end{aligned}$$

In the case of off-resonance condition ($\epsilon/\hbar - \Omega \neq 0$), the analytic transformation of this equation is not possible. In this study, the expectation value of the phonon amplitude in diamond is calculated by numerical simulation. The details are described in 6.5 Discussion.

6.3 Coherent control theory for optical phonons

Figure 6.7 shows the double-side Feynman diagrams for ISRS paths on the double pulse excitation [18]. $E_1(t)$ and $E_2(t)$ are the electric field of pump 1

and pump 2. Interaction between the optical pulse and the system occurs at time t_1 and t_2. The first diagram (Fig. 6.7 (A)) indicates the path A, in which the phonons generated by only the pump 1; the electronic excitation and de-excitation occur within the pulse. Similarly, the phonons are generated by the only pump 2, which is the path B and shown in the second diagram (Fig. 6.7 (B)). Figures 6.7 (C) and (D) show the path C and D in which the phonons are excited by both pump 1 and 2. The phonon-excitation and de-excitation are induced by the pump 1 and pump2, respectively, in the path C and vis versa in the path D. It should be noted that time t should be enough after the irradiation of pump 2.

The density operators for the four paths shown in Fig. 6.7 are denoted below.

In the path A, the time-evolution factor and multiplicative coefficient on $|g,0\rangle \rightarrow |e,1\rangle \rightarrow |g,1\rangle$ are gotten as

$$\text{interaction } (t_1) : \alpha \left(\frac{\mu E_0}{i\hbar}\right) f_1(t_1) e^{-i\Omega t_1}, \tag{6.26}$$

$$\text{time-evolution } (t_1 \rightarrow t_2) : e^{-\frac{i}{\hbar}(\epsilon+\hbar\omega)(t_2-t_1)}, \tag{6.27}$$

$$\text{interaction } (t_2) : \left(\frac{\mu E_0}{-i\hbar}\right) f_1(t_2) e^{i\Omega t_2}, \tag{6.28}$$

$$\text{time-evolution } (t_2 \rightarrow t) : e^{-i\omega(t-t_2)}. \tag{6.29}$$

The time evolution of density matrix on $|g,0\rangle \rightarrow |e,1\rangle \rightarrow |g,1\rangle$ is obtained by

$$\rho_A^{(1)}(t : t_1, t_2) = \alpha \left(\frac{\mu E_0}{\hbar}\right)^2 f_1(t_1) f_1(t_2) e^{-\frac{i}{\hbar}(\epsilon-\hbar\Omega)(t_2-t_1)} e^{-i\omega(t-t_1)} |g,1\rangle\langle g,0|, \tag{6.30}$$

where $|g,1\rangle$ and $\langle g,0|$ indicate the state vector for the electronic ground state with one-phonon state and that with zero-phonon state, respectively. The time-evolution factor and multiplicative coefficient on $|g,0\rangle \rightarrow |e,0\rangle \rightarrow |g,1\rangle$ are

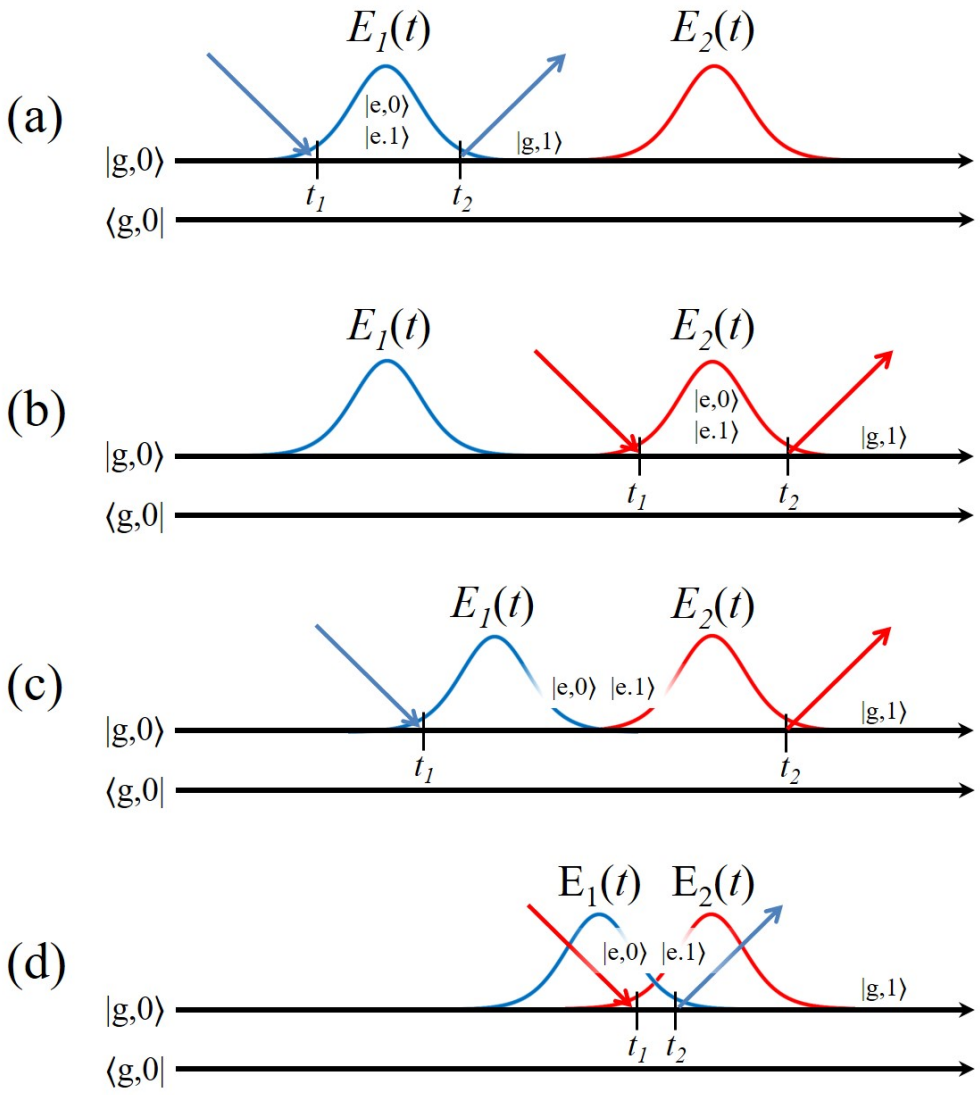

Fig. 6.7: Diagram of the ISRS paths. Transition occurs by only the pump 1 (A) or the pump 2 (B). (C) and (D) represent the transition occurring by both the pump 1 and pump 2. Time flows from the left to the right. The upper part of the diagram shows an envelope of the optical pulse. Interaction between the optical pulse and the system occurs at time t_1 and t_2. This figure is obtained from Fig. 1 of the paper, T. Kimata et al., Phys. Rev. B 101, 174301 (2020).

gotten as

$$\text{interaction } (t_1) : \left(\frac{\mu E_0}{i\hbar}\right) f_1(t_1) e^{-i\Omega t_1}, \tag{6.31}$$

$$\text{time-evolution } (t_1 \to t_2) : e^{-\frac{i}{\hbar}\epsilon(t_2-t_1)}, \tag{6.32}$$

$$\text{interaction } (t_2) : -\alpha \left(\frac{\mu E_0}{-i\hbar}\right) f_1(t_2) e^{i\Omega t_2}, \tag{6.33}$$

$$\text{time-evolution } (t_2 \to t) : e^{-i\omega(t-t_2)}. \tag{6.34}$$

The time evolution of density matrix on $|g,0\rangle \to |e,0\rangle \to |g,1\rangle$ is obtained by

$$\rho_A^{(2)}(t : t_1, t_2) = -\alpha \left(\frac{\mu E_0}{\hbar}\right)^2 f_1(t_1) f_1(t_2) e^{-\frac{i}{\hbar}(\epsilon-\hbar\Omega)(t_2-t_1)} e^{-i\omega(t-t_2)} |g,1\rangle\langle g,0|. \tag{6.35}$$

Therefore, the time evolution of density matrix of the path A is represented by

$$\begin{aligned}\rho_A(t) =& \rho_A^{(1)} + \rho_A^{(2)} + H.c. \\ =& \alpha \left(\frac{\mu E_0}{\hbar}\right)^2 e^{-i\omega t} \int_{-\infty}^{t} dt_2 \int_{-\infty}^{t_2} dt_1 f_1(t_1) f_1(t_2) \\ & \times e^{-\frac{i}{\hbar}(\epsilon-\hbar\Omega)(t_2-t_1)} \left(e^{i\omega t_1} - e^{i\omega t_2}\right) |g,1\rangle\langle g,0| + H.c.\end{aligned} \tag{6.36}$$

For the path B, the same process as for the path A occurs in electric field of pump 2 $E_2(t)$; the envelope of pump 1 $f_1(t)$ is replaced by that of pump 2 $f_2(t)$. Therefore, the time evolution of density matrix of the path B is represented by

$$\begin{aligned}\rho_B(t) =& \alpha \left(\frac{\mu E_0}{\hbar}\right)^2 e^{-i\omega t} \int_{-\infty}^{t} dt_2 \int_{-\infty}^{t_2} dt_1 f_2(t_1) f_2(t_2) \\ & \times e^{-\frac{i}{\hbar}(\epsilon-\hbar\Omega)(t_2-t_1)} \left(e^{i\omega t_1} - e^{i\omega t_2}\right) |g,1\rangle\langle g,0| + H.c.\end{aligned} \tag{6.37}$$

Next, path C and path D, which are paths where two interactions occur in different pump pulses, are described. When the delay between the pump 1 and pump 2 is very short, the path C and path D are important. In the path C, the first and second interactions occur at $E_1(t)$ and $E_2(t)$, respectively. The time-evolution factor and multiplicative coefficient on $|g,0\rangle \to |e,1\rangle \to |g,1\rangle$ are

obtained by

$$\text{interaction } (t_1) : \alpha \left(\frac{\mu E_0}{i\hbar} \right) f_1(t_1) e^{-i\Omega t_1}, \tag{6.38}$$

$$\text{time-evolution } (t_1 \rightarrow t_2) : e^{-\frac{i}{\hbar}(\epsilon+\hbar\omega)(t_2-t_1)}, \tag{6.39}$$

$$\text{interaction } (t_2) : \left(\frac{\mu E_0}{-i\hbar} \right) f_2(t_2) e^{i\Omega t_2}, \tag{6.40}$$

$$\text{time-evolution } (t_2 \rightarrow t) : e^{-i\omega(t-t_2)}. \tag{6.41}$$

The time evolution of density matrix on $|g,0\rangle \rightarrow |e,1\rangle \rightarrow |g,1\rangle$ is calculated as

$$\rho_C^{(1)}(t : t_1, t_2) = \alpha \left(\frac{\mu}{\hbar} \right)^2 E_0^2 f_1(t_1) f_2(t_2) e^{-\frac{i}{\hbar}(\epsilon-\hbar\Omega)(t_2-t_1)} e^{-i\omega(t-t_1)} |g,1\rangle\langle g,0|. \tag{6.42}$$

These parameters on $|g,0\rangle \rightarrow |e,0\rangle \rightarrow |g,1\rangle$ are also obtained by

$$\text{interaction } (t_1) : \left(\frac{\mu E_0}{i\hbar} \right) f_1(t_1) e^{-i\Omega t_1}, \tag{6.43}$$

$$\text{time-evolution } (t_1 \rightarrow t_2) : e^{-\frac{i}{\hbar}\epsilon(t_2-t_1)}, \tag{6.44}$$

$$\text{interaction } (t_2) : -\alpha \left(\frac{\mu E_0}{-i\hbar} \right) f_2(t_2) e^{i\Omega t_2}, \tag{6.45}$$

$$\text{time-evolution } (t_2 \rightarrow t) : e^{-i\omega(t-t_2)}. \tag{6.46}$$

The time evolution of density matrix $\rho_C^{(2)}$ is calculated as

$$\rho_C^{(2)}(t : t_1, t_2) = -\alpha \left(\frac{\mu E_0}{\hbar} \right)^2 f_1(t_1) f_2(t_2) e^{-\frac{i}{\hbar}(\epsilon-\hbar\Omega)(t_2-t_1)} e^{-i\omega(t-t_2)} |g,1\rangle\langle g,0|. \tag{6.47}$$

Therefore, the time evolution of density matrix of the path C is represented by

$$\begin{aligned} \rho_C(t) =& \rho_C^{(1)} + \rho_C^{(2)} + H.c. \\ =& \alpha \left(\frac{\mu E_0}{\hbar} \right)^2 e^{-i\omega t} \int_{-\infty}^{t} dt_2 \int_{-\infty}^{t_2} dt_1 f_1(t_1) f_2(t_2) \\ & \times e^{-\frac{i}{\hbar}(\epsilon-\hbar\Omega)(t_2-t_1)} \left(e^{i\omega t_1} - e^{i\omega t_2} \right) |g,1\rangle\langle g,0| + H.c. \end{aligned} \tag{6.48}$$

For the path D, the excitation and relaxation are induced by the pump 2 and pump 1, respectively. The density operator of the path D is

$$\begin{aligned}\rho_D(t) =&\alpha\left(\frac{\mu E_0}{\hbar}\right)^2 e^{-i\omega t}\int_{-\infty}^{t} dt_2 \int_{-\infty}^{t_2} dt_1 f_2(t_1) f_1(t_2) \\ &\times e^{-\frac{i}{\hbar}(\epsilon-\hbar\Omega)(t_2-t_1)}\left(e^{i\omega t_1}-e^{i\omega t_2}\right)|g,1\rangle\langle g,0| + H.c. \end{aligned} \tag{6.49}$$

Therefore, the density operator for all paths, $\rho(t)$, is obtained as

$$\rho(t) = \rho_A(t) + \rho_B(t) + \rho_C(t) + \rho_D(t) \tag{6.50}$$

$$\begin{aligned}=&\alpha\left(\frac{\mu}{\hbar}\right)^2 e^{-\imath\omega t}\int_{-\infty}^{t} dt_2 \int_{-\infty}^{t_2} dt_1 e^{-\frac{i}{\hbar}\epsilon(t_2-t_1)}\left(e^{i\omega t_1}-e^{i\omega t_2}\right) \\ &\cdot\left(E_0E_0f_1(t_1)f_1(t_2)e^{-\Omega(t_2-t_1)} + E_0E_0f_2(t_1)f_2(t_2)e^{-\Omega(t_2-t_1)}\right. \\ &\left.+ E_0E_0f_1(t_1)f_2(t_2)e^{-\Omega(t_2-t_1)} + E_0E_0f_2(t_1)f_1(t_2)e^{-\Omega(t_2-t_1)}\right) \\ &\cdot|g,1\rangle\langle g,0| + H.c. \end{aligned} \tag{6.51}$$

Here, if $(i,j) = (1,1),(2,2),(1,2),(2,1)$ corresponds to paths A, B, C, and D, respectively, the density operator is represented by

$$\begin{aligned}\rho(t) =&\alpha\left(\frac{\mu}{\hbar}\right)^2 e^{-i\omega t}\sum_{j=1}^{2}\sum_{k=1}^{2}\int_{-\infty}^{t} dt_2 \int_{-\infty}^{t_2} dt_1 E_j(t_1)E_k(t_2) \\ &\times e^{-\frac{i}{\hbar}\epsilon(t_2-t_1)}\left(e^{i\omega t_1}-e^{i\omega t_2}\right)|g,1\rangle\langle g,0| \\ &+ H.c., \end{aligned} \tag{6.52}$$

where $E_{1,2}(t) = E_0 f_{1,2}(t)\exp(-i\Omega t)$. This density operator is used for the numerical calculations, in 6.5 Discussion.

6.4 Transient transmittance measurement

6.4.1 Experimental Setup

The coherent optical phonons were investigated using a pump-probe-type transient-transmission measurement with two pump pulses (Fig. 6.8). The used laser was a Ti:sapphire oscillator (FEMTOLASERS: Rainbow) operating with

a repetition rate of 75 MHz. Fig. 6.9 (a) shows the spectrum measured immediately behind the output port, which has peaks at 694, 742, 792, 846 and 896 nm, measured using a USB spectrometer (OceanOptics: USB2000). Fig. 6.9 (b) shows the pulse waveform derived from the five Gaussian peaks. The pulse width was estimated to be 8.3 fs as full width at half maximum by using the frequency-resolved autocorrelation measurement (FEMTOLASERS: Femtometer).

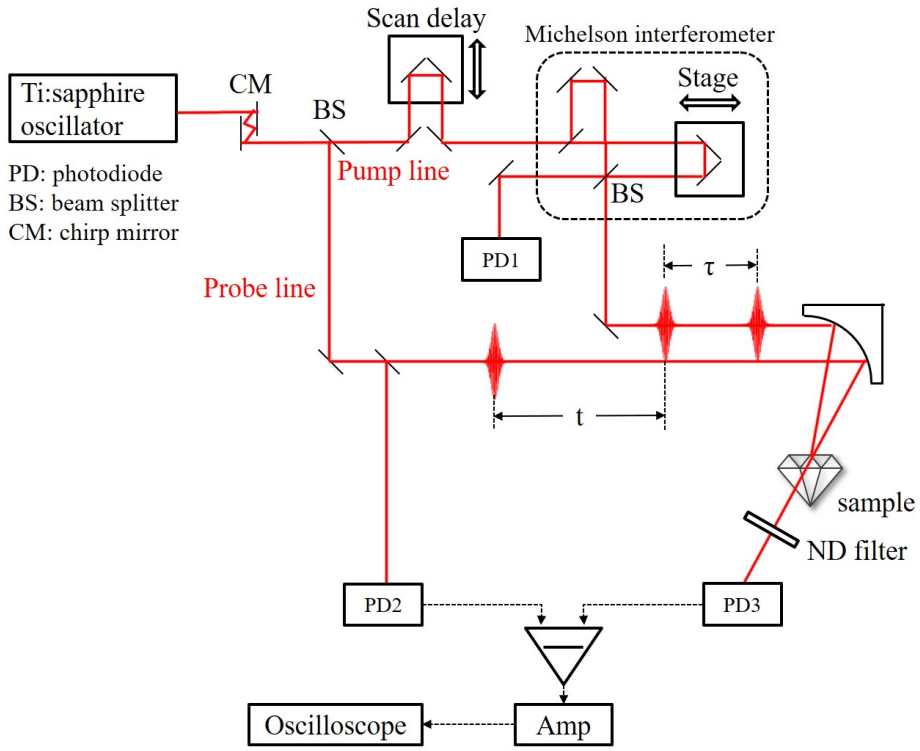

Fig. 6.8: Schematic of the experimental setup for coherent control measurements of optical phonons using the dual pump-probe technique. This setup was used for transient transmission measurements. Red and black dashed lines represent the optical path and electrical connection, respectively. This figure is obtained from Fig. 1 of the preprint, T. Kimata et al., arXiv:1912.12402v1 [physics.optics] 28 Dec 2019.

The output from the Ti:sapphire oscillator was introduced to compensate the group-velocity dispersion using a pair of chirp mirrors and divided into two pulses by a beam splitter. One was used as a pump pulse and the other was used as a probe pulse. The pump pulse was introduced to a scan-delay unit operating

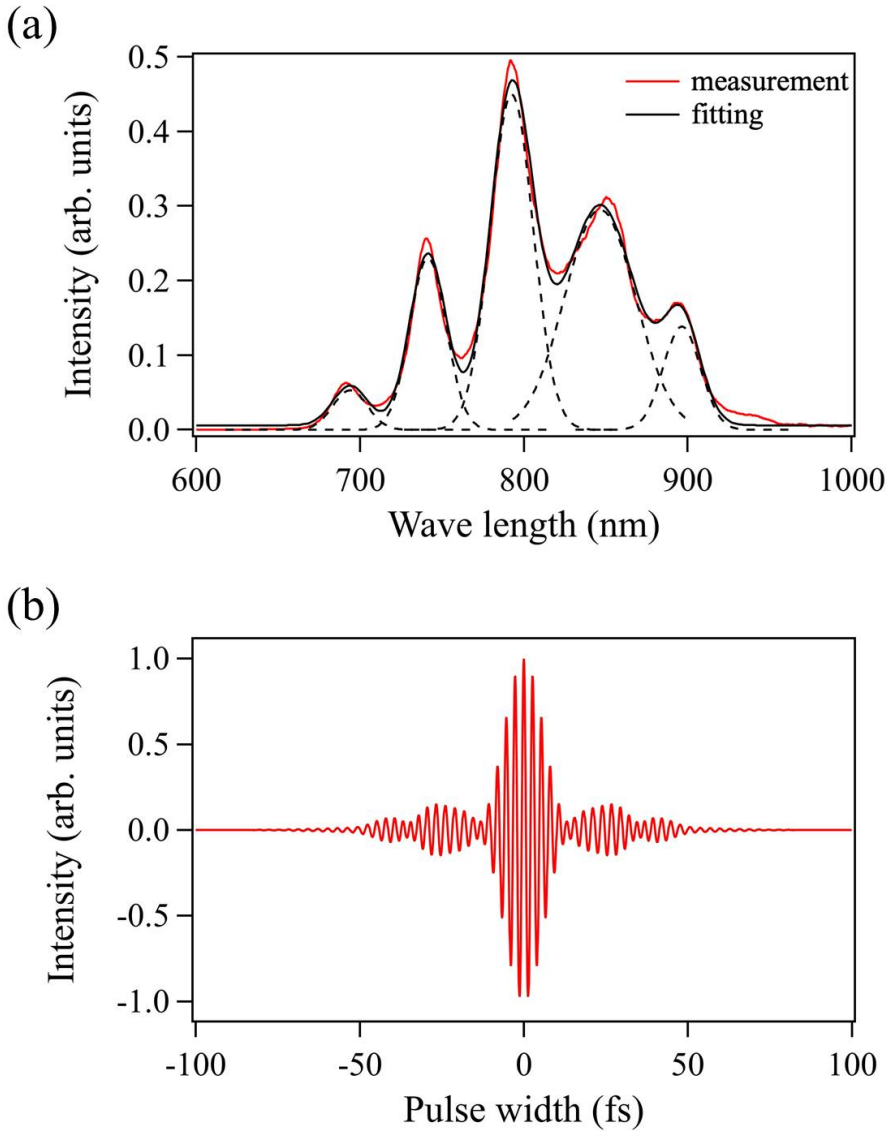

Fig. 6.9: (a) The measured spectrum of the ultrafast laser pulse (red) and the curve fitting with five Gaussian peaks (black). The dashed curves are each Gaussian peaks. (b) Electric field intensity generated from the five Gaussian pulses. The parameters for five Gaussian pulses are listed in the text. These figures are obtained by modifying Fig. 2 of the paper, T. Kimata et al., Phys. Rev. B 101, 174301 (2020).

at 20 Hz in order to control a delay (t) between pump and probe pulses. The pump pulse is introduced to a home-made Michelson-type interferometer [45] to produce a pair of pump pulses (pump 1 and 2). One optical arm of the interferometer was equipped with an automatic positioning stage (Sigma Tech Co. Ltd., FS-1050UPX), which moves with a minimum step of 1 nm. The delay between pump 1 and 2, τ (fs), was controlled by the stage of Michelson interferometer in 0.5 fs steps. The optical interference of pump-pump delay was detected by a photodiode (PD1).

The probe pulse was picked up by a 95:5 beam splitter to measure the reference beam intensity at a photodiode (PD2). Thereafter, both pump and probe pulses were focused on the sample by using an off-axis parabolic mirror. The transmitted pulse from the sample was detected with a photodiode (PD3). By applying the opposite bias voltages to PD2 and PD3, we set the balanced detection before the experiment. Its differential signal, amplified with a low-noise current amplifier (Stanford Research Systems: SR570), was measured by a digital oscilloscope (Iwatsu: DS5534). To reduce the statistical error, the 32 000 signals were averaged and taken as the measured value. By converting the temporal motion of the scan delay unit to the pump-probe pulse duration, the temporal evolution of the transmittance change $\Delta T/T_0$ was obtained. Here we used the heterodyne detection technique. The powers of the pump 1 and 2 and the probe were 21.2 mW, 21.3 mW, and 3.1 mW, respectively.

The sample used was a single crystal of diamond with a [100] crystal plane, which was fabricated by chemical vapor deposition and obtained from EDP corporation. The type of diamond was intermediate between Ib and IIa and its size was $5 \times 5 \times 0.7$ mm^3. The polarization of the pump and probe pulses were set along the [110] and [$-$110] axes, respectively.

6.4.2 Measurement result

Figure 6.10 is a two-dimensional map of the transient transmittance change $\Delta T/T_0$ as a function of the pump1-probe delay (t: horizontal axis) and pump1-pump2 delay (τ: vertical axis). At the fixed pump1-pump2 delay (τ), $\Delta T/T_0$ shows the sharp peak at delay zero between pump and probe and the successive oscillation with a frequency of 39.9±0.05 THz, which have been reported in a previous paper [27]. The oscillation is assigned to the optical phonons in diamond. On the other hand, at a fixed pump-probe delay (t), $\Delta T/T_0$ shows a rapid oscillation (approximately 380 THz) in addition to the oscillation due to the optical phonon (approximately 40 THz).

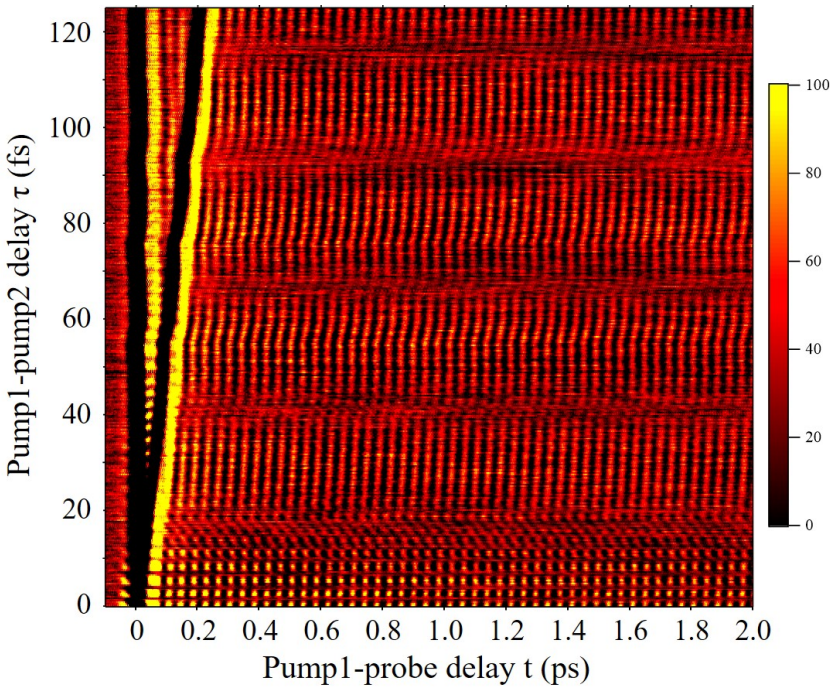

Fig. 6.10: Two-dimensional map of the change in transition intensity with the pump1-probe delay (t) and pump1-pump2 delay (τ). This figure is obtained from Fig. 3 of the paper, T. Kimata et al., Phys. Rev. B 101, 174301 (2020).

The Fourier transformation was performed between 0.5 ps $<$ 1.5 ps along the pump-probe delay after the irradiation of pump 2 at the each pump-pump delay. The optical phonon amplitude was obtained by the integration of the Fourier-

transformed data between 37.5 THz $\sim$ 42.5 THz, and then plotted against the pump-pump delay τ in Fig. 6.11 (a). Figure 6.11 (a) shows slow and fast

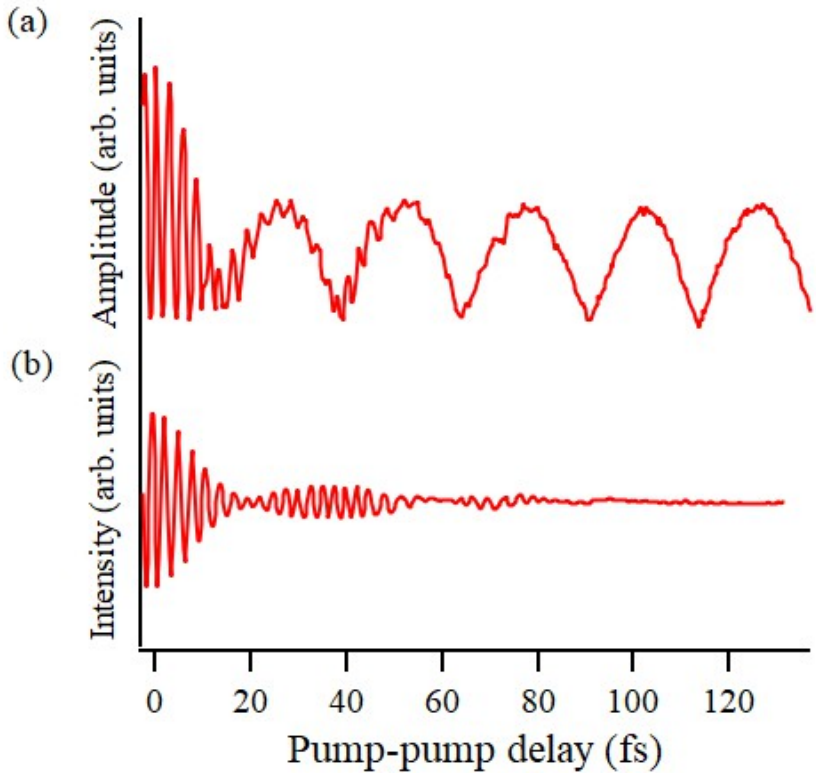

Fig. 6.11: The amplitude of (a) the controlled oscillation after pump 2 and (b) the optical interference against the pump-pump delay (τ). The amplitude is normalized using that obtained after excitation after only pump 1; oscillation between the pump 1 and pump 2 irradiation timing. This figure is obtained from Fig. 4 of the paper, T. Kimata et al., Phys. Rev. B 101, 174301 (2020).

oscillations, with an oscillational period of approximately 25 and 2.7 fs, respectively. The slow oscillation with a period of approximately 25 fs is observed at the pump-pump delay $\tau > 15$ fs. This oscillation is consistent with the oscillating function in the range of the pump-pump delay between 230 and 270 fs in a previous study [27]. The amplitude is enhanced or suppressed at timing of the pump-pump delay which matches to integer or half-integer multiply of the phonon oscillation period. This is due to constructive or destructive interference of coherent phonons. On the other hand, the rapid oscillation with a period of approximately 2.7 fs is observed at the pump-pump delay $\tau < 15$ fs. This oscil-

lation continues on the oscillating function of the constructive and destructive interference of coherent phonons until approximately 80 fs. The rapid oscillation would be originated by the optical interference of the dual pulses because the influence of optical interference detected by PD1 (Fig. 6.11 (b)) appeared in Fig. 6.11 (a).

6.5 Discussion

6.5.1 Pulse shape

In the calculation, we used the optical pulse composed of five Gaussian pulses:

$$E_1(t) = \sum_{k=1}^{5} E_k \exp\left(-\frac{t^2}{\sigma_k^2}\right) \cos\left(2\pi \cdot (\Omega_k + \theta t) \cdot t\right), \tag{6.53}$$

where E_k, Ω_k, and σ_k are the ratio of electric-field strengths, the optical frequency, and the pulse width of each component, respectively. The θ is the linear chirp rating. The electric field of pump 2 is defined as $E_2(t) = E_1(t-\tau)$, where τ is a delay between pump 1 and pump 2. The parameters were determined by curve fitting of the measured spectrum with five Gaussian-shape spectrum. The parameters are shown in Table 6.1. The pulse waveform of Fig. 6.9 (b) was represented by eq. (6.53) and the parameters.

Table 6.1: The parameters of the optical pulse

E_k	Ω_k [1/fs]	σ_k [fs]
0.045	0.432	24.16
0.197	0.405	26.18
0.385	0.379	25.42
0.253	0.354	17.61
0.119	0.335	37.45

The chirping effect is also considered to reproduce the actual pulse-envelope. The first order optical interference is calculated from the electronic field of the

two pump pluses, shown in Fig. 6.12. Figure 6.12 shows the first order optical interference at the linear chirping rates between 0 and 8×10^{-4} fs^{-2}. By comparing with the detected optical interference (Fig. 6.11 (b)), θ was set to 5×10^{-4} fs^{-2}.

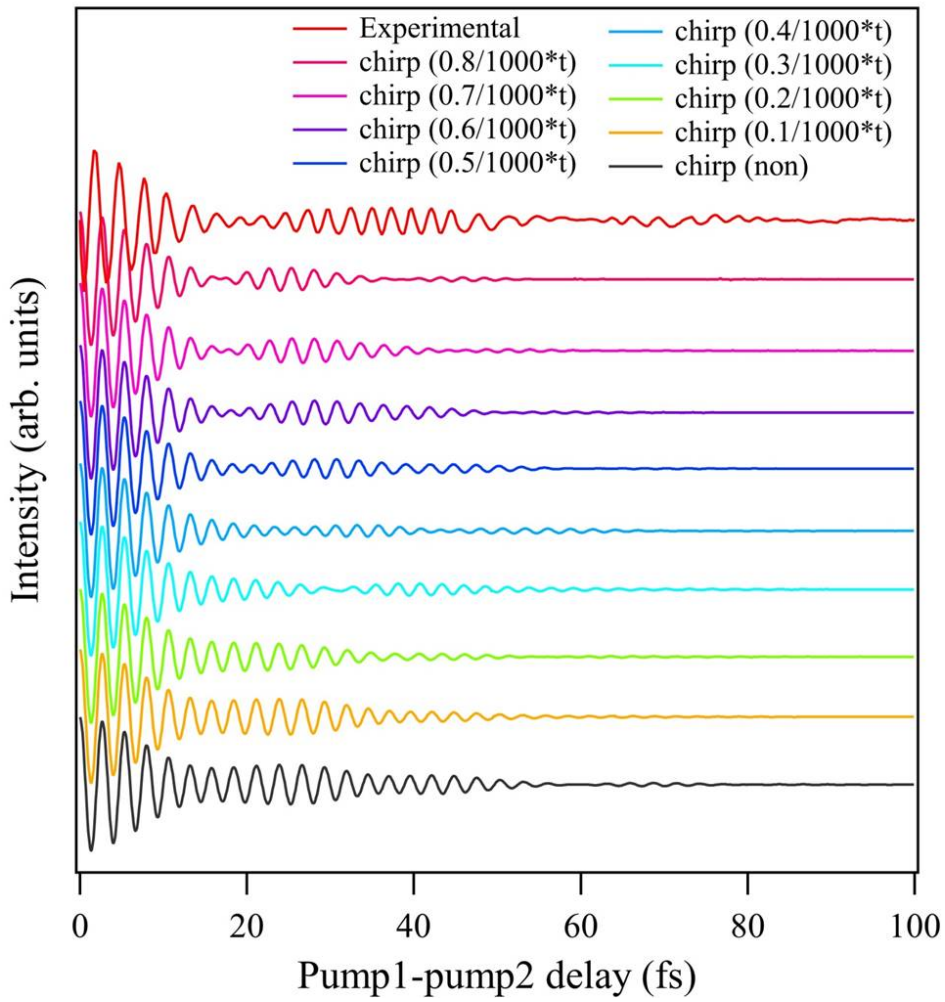

Fig. 6.12: The first order optical interference at each linear chirping rate.

6.5.2 Phonon amplitude

The mean value of the phonon coordinate is obtained by $\langle Q(t)\rangle = \mathrm{Tr}\{Q\rho(t)\}$, where $Q \equiv \sqrt{\hbar/2\omega}(b+b^{\dagger})$ and Tr indicates that the trace should be taken over the electronic and phonon variables. In this study, the mean value was estimated by numeric calculation. As described above, the rotating-wave approximation is not applied due to the large detuning condition (If it is a resonance condition, it

can be calculated using the rotating-wave approximation as the previous report [18].).

The calculated phonon amplitude for all paths shown in Fig. 6.13 (b) represents well the experimental data (Fig. 6.13 (a)). The rapid oscillation with a period of approximately 2.7 fs at the pump-pump delay $\tau < 15$ fs is caused by the optical interference, which is represented by paths C and D. This interference pattern corresponds well to the optical interference (shown in Fig. 6.11 (b)) and no electronic-coherence effect, which was reported in the coherent-control experiments on GaAs at resonance conditions [18], has not been observed. On the other hand, the slow oscillation with a period of approximately 25 fs is caused by the phonon interference, which is due to the path A and B. In fact, the calculated phonon amplitude via path A and B shows only the slow oscillation as shown in Fig. 6.13 (c). As already reported [27], the phonon amplitude after the second pump pulse irradiation is a sum of two sinusoidal functions induced by each pulse.

6.5.2.1 Chirping effect

In order to investigate the influence of the linear chirping on the phonon amplitude, the phonon amplitude at the linear chirp rating of 0 and 5×10^{-4} fs^{-2} is calculated by using eq. (6.53). Figure 6.14 shows the phonon amplitude (a) obtained from the experiment, (b) calculated without the chirp rating, and (c) calculated with the chirp rating of 5×10^{-4} fs^{-2}. As described above, the calculated phonon amplitude with the chirp rating of 5×10^{-4} fs^{-2} (Fig. 6.14 (c)) represents well the experimental data (Fig. 6.14 (a)). A difference of interference pattern between including and non-including the chirp rating (Fig. 6.14 (b)) was observed at the pump1-pump2 delay of 15$\sim$50 fs. It is considered that the pattern of first-order optical interference seen in Fig. 6.12 just appears on the phonon interference (Fig. 6.13 (c)) due to large detuning.

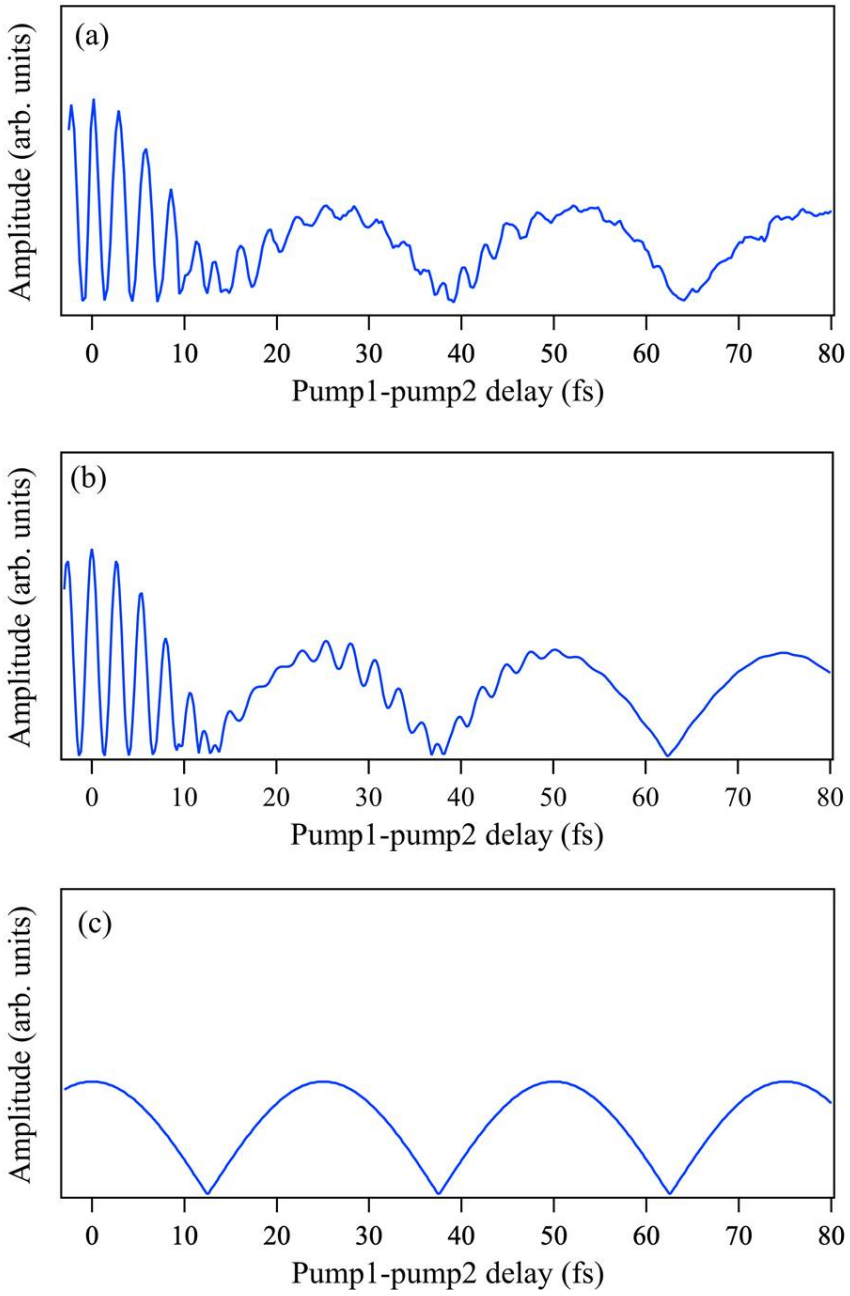

Fig. 6.13: (a) The measured amplitude of the controlled oscillation after pump 2 on the pulse overlap region. (b) The calculated phonon amplitude for all paths. (c) The calculated phonon amplitude for path A and path B. These figures are obtained by modifying Fig. 5 of the paper, T. Kimata et al., Phys. Rev. B 101, 174301 (2020).

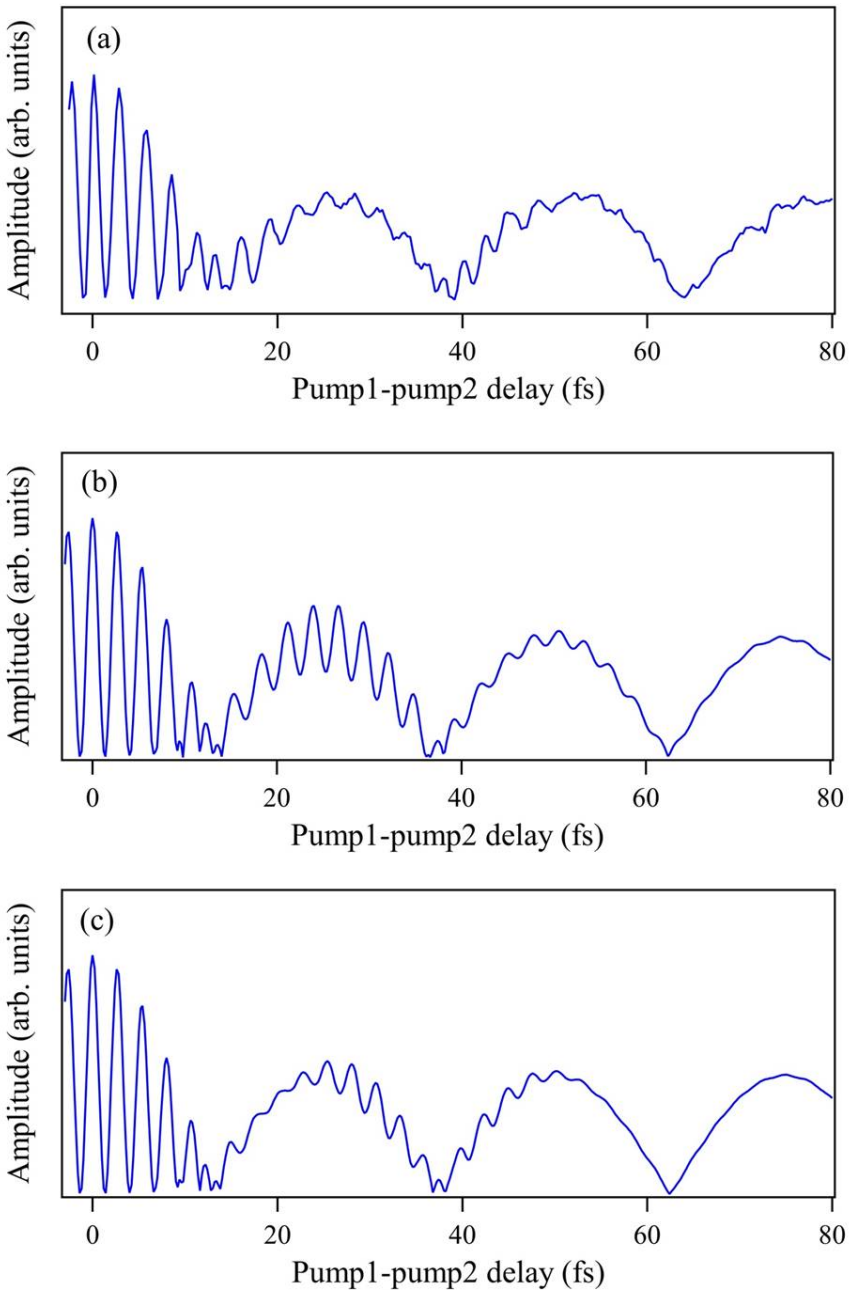

Fig. 6.14: (a) The measured amplitude of the controlled oscillation after pump 2 on the pulse overlap region. (b) The calculated phonon amplitude without the chirp rating ($\theta = 0$). (c) The calculated phonon amplitude with the chip rating (θ=5$\times$10^{-4} fs^{-2}).

6.5.2.2 Resonance condition

The direct bandgap of diamond is well above the energy of the optical pulse, the coherent phonons are excited by the ISRS process at off-resonant condition. Here, the behavior of phonon amplitude at the resonant condition is also calculated to investigate the electronic coherence effect. The following parameters were used in this calculation; (E_k, Ω_k [1/fs], σ_k [fs]) =(0.045, 0.432, 28.45),(0.197, 0.405, 30.82), (0.385, 0.379, 29.94), (0.253, 0.354, 20.73), and (0.119, 0.335, 44.09).

Figure 6.15 shows the phonon amplitude at the pump-pump delay (τ) of 0 fs, on (a) $\theta = 0$ and (b) θ=0.5/1000 (fs^{-2}). The phonon amplitude at $\tau = 0$ was calculated when the ϵ in the eq. (6.52) was varied from 0 to 7.4 eV. In both figures, an increase in phonon amplitude between 1$\sim$2 eV is observed. At energy values higher than about 2 eV, the phonon amplitude becomes smaller as ϵ increases. This trend would be due to the detuning effect. On the other hand, an increase in phonon amplitude between 1$\sim$2 eV is considered due to optical resonance (around 1.5 eV).

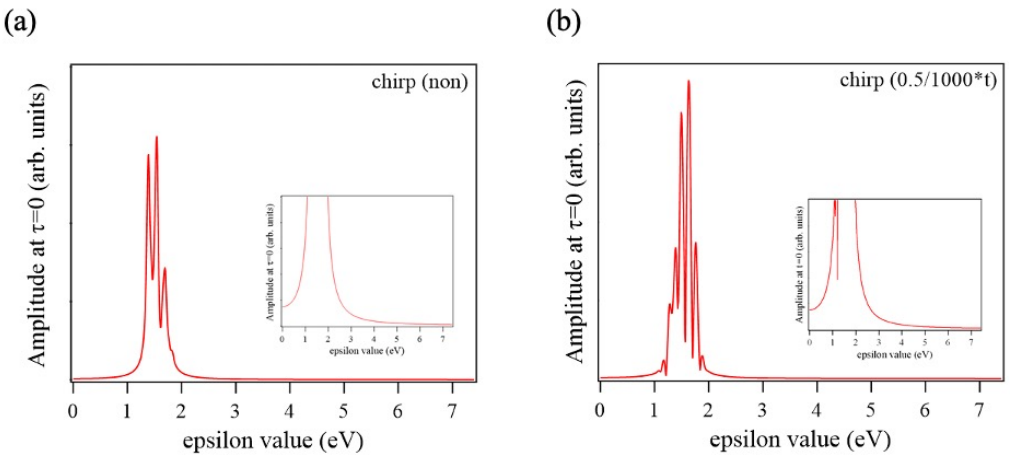

Fig. 6.15: The calculated phonon amplitude at $\tau = 0$ against ϵ. The chirp rating is set (a) θ=0 and (b) θ=0.5/1000 (fs^{-2}) in these numerical calculations.

Here, the energy of each pulse is calculated from the five Gaussian-shape spectrum, and the behavior of the phonon amplitude against the pump-pump

delay is investigated. The center frequency of the five Gaussian-shape spectrum is converted to the energy; the parameters are (frequency [THz], energy [eV]) = (335, 1.38), (354, 1.46), (379, 1.56), (405, 1.67), and (432, 1.79). Figure 6.16 shows the calculated phonon amplitude at ϵ=1.38, 1.46, 1.56, 1.67, and 1.82 eV. Unlike in the case of ϵ=7.4 eV, the rapid oscillation with a period of $\sim$ 2.7 fs was observed even after the optical interference by the pump-pulse overlapping ended at pump-pump delay $>$ ca. 50 fs (except the eps 1.56 eV in Fig. 6.16 (b)). This would be due to the optical interference appears significantly as an interference pattern. The interference pattern of the electronic coherence effect which was reported in the coherent control on GaAs [18] is also observed.

The behavior of the phonon amplitude against pump-pump delay becomes constant above about 2.5 eV, which is dominated by optical and phonon interferences; indicating out of resonance condition. This result suggests that it can be treated as a large detuning case above ca. 2.5 eV.

6.5.2.3 Single Gaussian pulse case

The behavior of the phonon amplitude exited by a single Gaussian pulse is also investigated. The center frequency and width of the optical pulse are set 375 THz and 8.3 fs, respectively; (E_k, Ω_k [1/fs], σ_k [fs]) =(1, 0.375, 8.3).

Figure 6.17 shows (a) the electronic field intensity generated from the Gaussian curve and (b) the first-order optical interference. The chirping rate is set θ=0 and 5.0×10^{-4} fs^{-2}. In comparison to the five Gaussian pulse (Fig. 6.9 (b) and Fig. 6.12), the interference patterns are not observed at the pulse width at 20$\sim$50 fs and the pump-pump delay at 20$\sim$50 fs in Fig6.17 (a) and (b), respectively. The phonon amplitude of these cases on ϵ=7.4 eV is shown in Fig. 6.17 (c). A slight difference due to the chirping effect was observed at the pump-pump delay of 10$\sim$15 fs. This difference was also less pronounced than for the five Gaussian pulse.

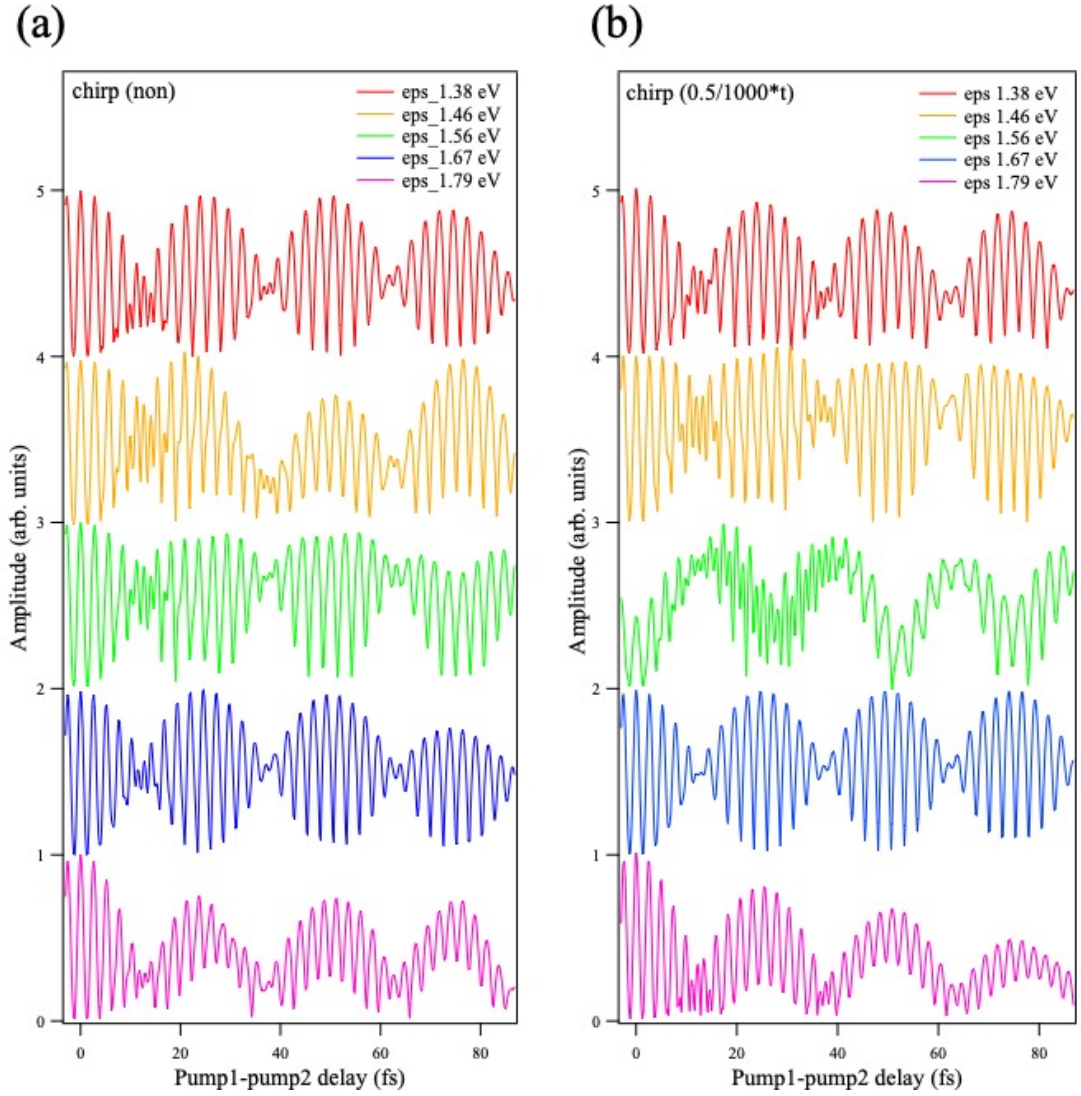

Fig. 6.16: The phonon amplitude calculated at ϵ=1.38, 1.46, 1.56, 1.67, and 1.82 eV. The chirp rating is set (a) θ=0 and (b) θ=0.5/1000 (fs^{-2}) in these numerical calculations.

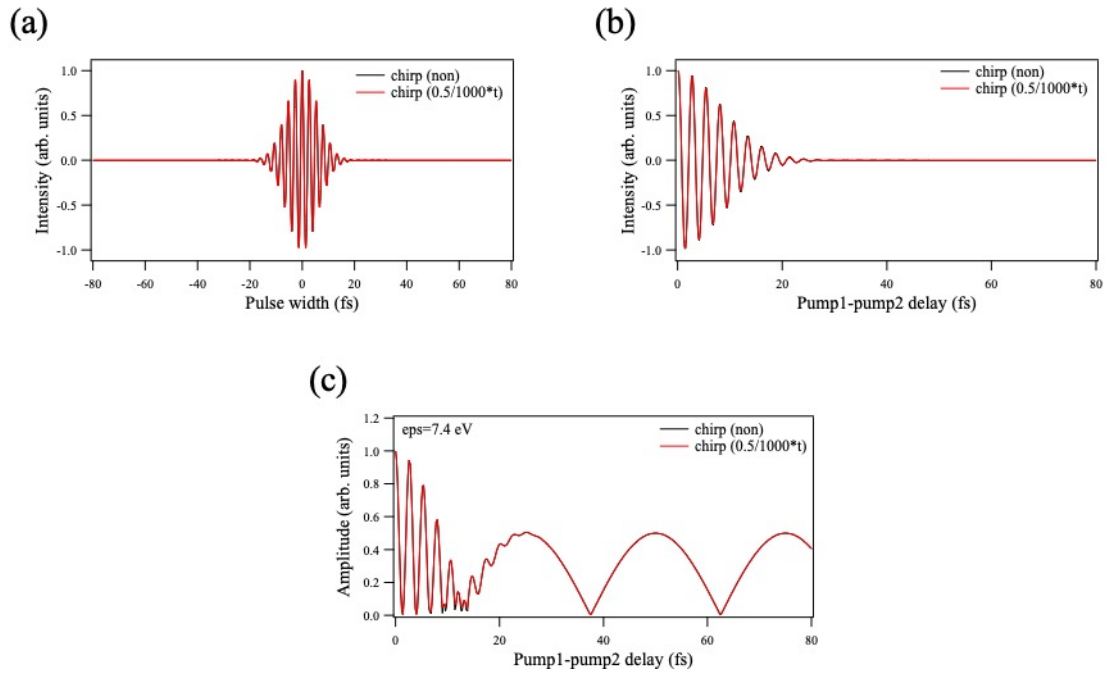

Fig. 6.17: (a) The electronic field intensity generated from the Gaussian curve. (b) The first order optical interference. (c) The calculated phonon amplitude for single Gaussian pulse.

6.5.3 Dephasing

The challenge for the future is to consider the defects induced by ion irradiation in the materials. The simplest approach is to add a dephasing term, $\exp(-\Gamma t)$, to the density matrix. By introducing $\exp(-\Gamma t)$, a time-dependent decay term, into the time evolution factor, relaxation due to lattice defects in the materials would also be discussed. For example, the time evolution factor on $|g,0\rangle \rightarrow |e,1\rangle \rightarrow |g,1\rangle$ would be written as

$$e^{-\frac{i}{\hbar}(\epsilon+\hbar\omega)(t'-t'')}e^{-\Gamma(t'-t'')}, \quad \text{and} \quad e^{-i\omega(t-t')}e^{-\Gamma(t-t')}. \tag{6.54}$$

6.6 Summary

In Chapter 6, I modified the coherent control theory for optical phonons without using a rotating-wave approximation in order to calculate the large detuning case such as diamond crystal. In addition, I take the frequency chirping and non-Gaussian pulse shape into consideration. The coherent control of the am-

plitude of the 40-THz optical phonons in diamond was demonstrated by using a pair of infra-red pulses at the pump-pump delay between -10 and 120 fs, and analyzed by using the modified theory. As a result, the modified theory reproduced well the experimental data. The cases of resonance condition and a single Gaussian pulse were also discussed.

References

[1] H.J. Zeiger, J.Vidal, T.K. Cheng, E.P. Ippen, G. Dresselhaus, M.S. Dresselhaus. *Theory for displacive excitation of coherent phonons.* Phys. Rev. B **45**, 768 (1992).

[2] H. Katsuki, J.C. Delagnes, K. Hosaka, K. Ishioka, H. Chiba, E.S. Zijlstra, M.E. Garcia, H. Takahashi, K. Watanabe, M. Kitajima, Y. Matsumoto, K.G. Nakamura, K. Ohmori. *All-optical control and visualization of ultrafast two-dimensional atomic motions in a single crystal of bismuth.* Nat. Commun. **4**, 2801 (2013).

[3] M. Hase, M. Kitajima, A. M. Constantinescu, H. Petek. *The birth of a quasiparticle in silicon observed in time-frequency space.* Nature **426**, 51 (2003).

[4] I.H. Lee, K.J. Yee, K.G. Lee, E. Oh, D.S. Kim, Y.S. Lim. *Coherent optical phonon mode oscillations in wurtzite ZnO excited by femtosecond pulses.* J. Appl. Phys. **93**, 4939 (2003).

[5] W. Albrecht, Th. Kruse, H. Kurz. *Time-Resolved Observation of Coherent Phonons in Superconducting $YBa_2Cu_3O_{7-\delta}$ Thin Films.* Phys. Rev. Lett. **69**, 1451 (1992).

[6] P. Brumer and M. Shapiro. *Control of unimolecular reactions using coherent light.* Chem. Phys. Lett. **126**, 541 (1986).

[7] S. A. Rice, D. J. Tannor, R. Kosloff. *Coherent pulse sequence induced control of selectivity of reactions. Exact quantum-mechanical calculations.* J. Chem. Soc., Faraday Trans. 2 **82**, 2423 (1986).

[8] N. F. Scherer, R. J. Carlson, A. Matro, M. Du, A. J. Ruggiero, V. Romero-Rochin, J. A. Cina, G. R. Fleming, S. A. Rice. *Fluorescence- detected wave packet interferometry: Time resolved molecular spectroscopy with sequences of femtosecond phase- locked pulses.* J. Chem. Phys. **95**, 1487 (1991).

[9] R. Unanyan, M. Fleischhauer, B. W. Shore, K. Bergmann. *Robust creation and phase-sensitive probing of superposition states via stimulated Raman adiabatic passage (STIRAP) with degenerated dark states.* Opt. Commun. **155**, 144 (1998).

[10] T. C. Weinacht, J. Ahn, P. H. Bucksbaum. *Controlling the shape of a quantum wavefunction*. Nature **397**, 233 (1999).

[11] D. Meshulach, Y. Silberberg. *Coherent quantum control of two-photon transitions by a femtosecond laser pulse*. Nature **396**, 239 (1998).

[12] K. Ohmori, H. Katsuki, H. Chiba, M. Honda, Y. Hagihara, K. Fujiwara, Y. Sato, K. Ueda. *Real-Time Observation of Phase-Controlled Molecular Wave-Packet Interference*. Phys. Rev. Lett. **96**, 093002 (2006).

[13] H. Katsuki, H. Chiba, B. Girard, C. Meier, K. Ohmori. *Visualizing Picometric Quantum Ripples of Ultrafast Wave-Packet Interference*. Science **311**, 1589 (2006).

[14] M.P.A. Branderhorst, P. Londero, P. Wasylczyk, C. Brif, R.L. Kosut, H. Rabitz, I.A. Walmsley. *Coherent Control of Decoherence*. Science **320**, 638 (2008).

[15] K. Ohmori. *Wave-Packet and Coherent Control Dynamics*. Annu. Rev. Phys. Chem. **60**, 487 (2009).

[16] A. Noguchi, Y. Shikano, K. Toyoda, S. Urabe. *Aharonov-Bohm effect in the tunnelling of a quantum rotor in a linear Paul trap*. Nat. Commun. **5**, 3868 (2014).

[17] G. Higgins, F. Pokorny, C. Zhang, Q. Bodart, M. Hennrich. *Coherent Control of a Single Trapped Rydberg Ion*. Phys. Rev. Lett. **119**, 220501 (2017).

[18] K.G. Nakamura, K. Yokota, Y. Okuda, R. Kase, T. Kitashima, Y. Mishima, Y. Shikano, Y. Kayanuma. *Ultrafast quantum-path interferometry revealing the generation process of coherent phonons*. Phys. Rev. B **99**, 180301(R) (2019).

[19] T. Dekorsy, W. Kütt, T. Pfeifer, and H. Kurz. *Coherent control of LO-phonon dynamics in opaque semiconductors by femtosecond laser pulses*. Europhys. Lett. **23**, 223 (1993).

[20] M. Hase, K. Mizoguchi, H. Harima, S. Nakashima, M. Tani, K. Sakai, M. Hangyo. *Optical control of coherent optical phonons in bismuth films*. Appl. Phys. Lett. **69**, 2474 (1996).

[21] Y.-H. Cheng, F. Y. Gao, S. W. Teitelbaum, K. A. Nelson. *Coherent control of optical phonons in bismuth*. Phys. Rev. B **96**, 134302 (2017).

[22] F. Sun, Q. Wu, Y.L. Wu, H. Zhao, C.J. Yi, Y.C. Tian, H.W. Liu, Y.G. Shi, H. Ding, X. Dai, P. Richard, J. Zhao. *Coherent helix vacancy phonon and its ultrafast dynamics waning in topological Dirac semimetal Cd_3As_2*. Phys. Rev. B **95**, 235108 (2017).

[23] L.L. Hu, M. Yang, Y.L. Wu, Q. Wu, H. Zhao, F. Sun, W. Wang, R. He, S.L. He, H. Zhang, R.J. Huang, L.F. Li, Y.G. Shi, J. Zhao. *Strong pseudospin-lattice coupling in $Sr_3Ir_2O_7$: Coherent phonon anomaly and negative thermal expansion.* Phys. Rev, B **99**, 094307 (2019).

[24] H. Mashiko, Y. Chisuga, I. Katayama, K. Oguri, H. Masuda, J. Takeda, H. Gotoh. *Multi-petahertz electron interference in $Cr:Al_2O_3$ solid-state material.* Nat. Commun. **9**, 1468 (2018).

[25] K. G. Nakamura, Y. Shikano, Y. Kayanuma. *Influence of pulse width and detuning on coherent phonon generation.* Phys. Rev. B **92**, 144304 (2015).

[26] K. G. Nakamura, K. Ohya, H. Takahashi, T. Tsuruta, H. Sasaki, S. Uozumi, K. Norimatsu, M. Kitajima, Y. Shikano, Y. Kayanuma. *Spectrally resolved detection in transient-reflectivity measurements of coherent optical phonons in diamond.* Phys. Rev. B **94**, 024303 (2016).

[27] H. Sasaki, R. Tanaka, Y. Okano, F. Minami, Y. Kayanuma, Y. Shikano, K. G. Nakamura. *Coherent control theory and experiment of optical phonons in diamond.* Sci. Rep. **8**, 9609 (2018).

[28] K. C. Lee, M. R. Sprague, B. J. Sussman, J. Nunn, N. K. Langford, X.-M. Jin, T. Champion, P. Michelberger, K. F. Reim, D. England, D. Jaksch, I. A. Walmsley. *Entangling Macroscopic Diamonds at Room Temperature.* Science **334**, 1253 (2011).

[29] K. C. Lee, B. J. Sussman, M. R. Sprague, P. Michelberger, K. F. Reim, J. Nunn, N. K. Langford, P. J. Bustard, D. Jaksch, I. A. Walmsley. *Macroscopic non-classical states and terahertz quantum processing in room-temperature diamond.* Nat. Photon. **6**, 41 (2012).

[30] D. G. England, P. J. Bustard, J. Nunn, R. Lausten, B. J. Sussman. *From Photons to Phonons and Back: A THz Optical Memory in Diamond.* Phys. Rev. Lett. **111**, 243601 (2013).

[31] D. G. England, K. A. G. Fisher, J.-P. W. MacLean, P. J. Bustard, R. Lausten, K. J. Resch, B. J. Sussman, Phs. Rev. Lett. **114**, 053620 (2015).

[32] K. Ishioka, M. Hase, M. Kitajima, H. Petek. *Coherent optical phonons in diamond.* Appl. Phys. Lett. **89**, 231916 (2006).

[33] M. Zukerstein, M. Kozák, F. Trojánek, P. Malý. *Experimental observation of anharmonic effects in coherent phonon dynamics in diamond.* Diamond & Related Matter. **90**, 202-206 (2018).

[34] M. Zukerstein, F. Trojánek, B. Rezek, Z. Šobáň, M. Kozák, P. Malý. *Coherent phonon dynamics in diamond detected via multiphoton absorption.* Appl. Phys. Lett. **115**, 161104 (2019).

[35] A. Yamada, K. Yabana. *Multiscale time-dependent density functional theory for a unified description of ultrafast dynamics: Pulsed light, electron, and lattice motions in crystalline solds* . Phys. Rev. B **99**, 245103 (2019).

[36] J. Shah. In*Ultrafast Spectroscopy of Semiconductors and Semiconductor Nanostructures.* Springer Series in Solid-State Sciences **115**, Springer-Verlag (Berlin, 1996).

[37] A.P. Heberle, J.J. Baumberg. sl Ultrafast coherent control and destruction of excitations in quantum wells. Phys. Rev. Lett. **75**, 2598 (1995).

[38] M.U. Wehner, M.H. Uim, D.S. Chemla, M. Wegener. *Coherent control of electron-LO phonons scattering in bulk GaAs.* Phys. Rev. Lett. **80**, 1992 (1998).

[39] M. Gurioli, F. Bogani, S. Cecheriri, M. Colocci. *Coherent vs incoherentemission from semiconductor structures after resonant femtosecond excitation.* Phys. Rev. Lett. **78**, 3205 (1997).

[40] M. Wegener. *Quantum coherence in semiconductors.* J. Lumin. **87-89**, 20 (2000).

[41] V.M. Axt, T. Kuhn. sl Femtosecond spectroscopy in semiconductors: a ley tocoherences, correlations and quantum kinetics. Rep. Prog. Phys. **67**, 433 (2004).

[42] Kazutaka Nakamura. In *Quantum Phononics.* Springer Tracts in Modern Physics **282** (Springer Nature, 2019).

[43] W. Saslow, T. K. Bergstresser, M. L. Cohen. *Band structure and optical properties of diamond.* Phys. Rev. Lett. **16**, 354 (1996).

[44] R. P. Milden. In *Optical engineering of diamonds*, edited by R. P. Milden and J. R. Rabeau, (Wiley-VCH, Weinheim, 2013), pp. 1-34.

[45] S. Hayashi, K. Kato, K. Norimatsu, M. Hada, Y. Kayanuma, K. G. Nakamura. *Measuring quantum coherence in bulk solids using dual phase-locked optical pluses.* Sci. Rep. **4**, 4456 (2014).

Chapter 7

Conclusion

In the present work, the spectroscopic analyses were performed to clarify the influence of ion-beam irradiation on the defect and electronic structure of the carbon materials used as a support for Pt nanoparticles. Prior to the spectroscopic analysis, the ORR activity of the Pt nanoparticles was investigated by electrochemical measurement; we found that the Pt nanoparticles on the Ar^+-irradiated glassy carbon substrates exhibited more than twice as high ORR activity as those on non-irradiated one.

The findings of this study are described below.

1. X-ray spectroscopic analysis indicated that the electronic structure originating from Pt−C interactions with charge transfer from Pt to C changed due to the introduction of vacancies into the carbon substrates.
2. The phonon correlation length L_a obtained from the Raman spectrum estimated the number of defects interacting with Pt nanoparticles, and indicated that ca. three-point-defects were present at the interface structure between each 5 nm Pt nanoparticle and the HOPG irradiated with Ar^+ at the fluence of 1.0×10^{13} ions/cm^2.
3. DFT calculation of the Pt cluster on graphite structure with vacancies indicated the lower ϵ_d value on the multiple vacancies. The Pt nanoparticles on

the carbon supports with vacancies may exhibit higher ORR activity than that on carbon supports without vacancies.

4. The quantum mechanical theory of the coherent control of optical phonons by femtosecond optical pulses was modified for a large detuning condition. The prospect of revealing the defective structure and electronic state of carbon materials with ultrafast dynamics has been established.

These results will be discussed comprehensively. The ion-beam-induced lattice defects in carbon support would boost the formation of the Pt−C interactions with charge transfer from Pt to C, and change the electronic structure of the Pt nanoparticles, resulting in the enhancement of the ORR activity of Pt nanoparticles. The theoretical model for the coherent control of optical phonons was also developed, as the first step, in order to elucidate the influence of defects in carbon materials on the ultrafast dynamics. The findings of this study were concluded as described above.

In this study, the double vacancy and defects in the second layer in the graphite structure were found to have a significant effect on the electronic structure of Pt atoms. Therefore, ion-beam irradiation into the carbon support would be a useful method to manipulate the electronic state of the deposited metal nanoparticles. As a result, the method will contribute to the preparation of novel functional materials.

Appendix A

Program for numerical calculations

In Appendix A, an example of the python script for numerical calculation used in Chapter 6 is described. However, the Matlab script is also used in the calculations in Chapter 6, in addition to the python script example described below.

A.1 Optical electric field for python

```
import numpy as np
import matplotlib.pyplot as plt
yy=np.arange(0,3201,1.0)
tt1=np.arange(0,3201,1.0)
yy1=np.arange(0,3201,1.0)
yy2=np.arange(0,3201,1.0)
yy3=np.arange(0,3201,1.0)
yy4=np.arange(0,3201,1.0)
yy5=np.arange(0,3201,1.0)
Y1=np.arange(0,3201,1.0)
[E1,E2,E3,E4,E5]=[0.045,0.197,0.385,0.253,0.119]#peak intensity ratio
[L1,L2,L3,L4,L5]=[0.432,0.405,0.379,0.354,0.335]#optical frequency (1/fs)
[S1,S2,S3,S4,S5]=[28.45,30.82,29.94,20.73,44.09]#pulse width (fs)
chirp=0#chirp rating (non-chirp)
```

```
for i in range(3201):
    tt=(i*0.1)-160 #0.1 fs step (-160∼160 fs)
    tt1[i]=tt
    yy1[i]=E1*np.exp(-tt**2/(S1**2))*np.cos(2*np.pi*(L1+chirp*tt)*tt)
    yy2[i]=E2*np.exp(-tt**2/(S2**2))*np.cos(2*np.pi*(L2+chirp*tt)*tt)
    yy3[i]=E3*np.exp(-tt**2/(S3**2))*np.cos(2*np.pi*(L3+chirp*tt)*tt)
    yy4[i]=E4*np.exp(-tt**2/(S4**2))*np.cos(2*np.pi*(L4+chirp*tt)*tt)
    yy5[i]=E5*np.exp(-tt**2/(S5**2))*np.cos(2*np.pi*(L5+chirp*tt)*tt)
    Y1[i]=yy1[i]+yy2[i]+yy3[i]+yy4[i]+yy5[i]
plt.plot(tt1,Y1)
```

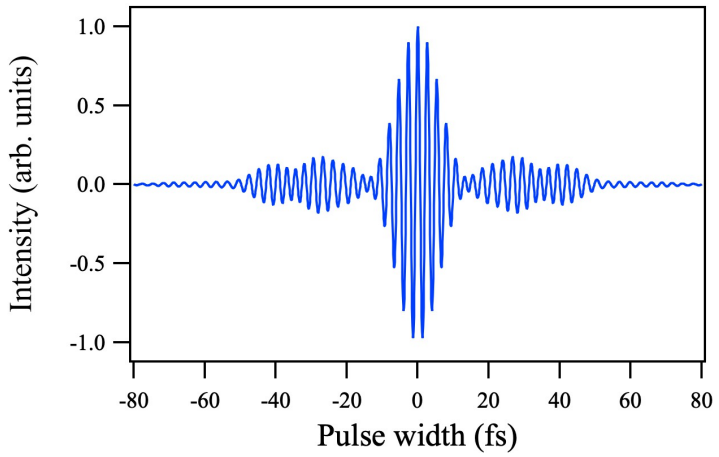

Fig. A.1: Calculated electric field of optical pulse.

A.2 Optical interference for python

```
import numpy as np
from scipy import integrate
import matplotlib.pyplot as plt
yy2=np.arange(0,1000,1.0)
tt2=np.arange(0,1000,1.0)
[E1,E2,E3,E4,E5]=[0.045,0.197,0.385,0.253,0.119]#peak intensity ratio
[L1,L2,L3,L4,L5]=[0.432,0.405,0.379,0.354,0.335]#optical frequency (1/fs)
[S1,S2,S3,S4,S5]=[28.45,30.82,29.94,20.73,44.09]#pulse width (fs)
chirp=0.5/1000 #chirp rating
def Efield(t): #definition of function for electric field of laser pulse
```

```
    EE=E1*np.exp(-t**2/(S1**2))*np.cos(2*np.pi*(L1+chirp*t)*t)\
        +E2*np.exp(-t**2/(S2**2))*np.cos(2*np.pi*(L2+chirp*t)*t)\
        +E3*np.exp(-t**2/(S3**2))*np.cos(2*np.pi*(L3+chirp*t)*t)\
        +E4*np.exp(-t**2/(S4**2))*np.cos(2*np.pi*(L4+chirp*t)*t)\
        +E5*np.exp(-t**2/(S5**2))*np.cos(2*np.pi*(L5+chirp*t)*t)
        return EE
j=1
for j in range(1000):
    tau=j*0.1
    tt2[j]=tau
    def h(t):
        return Efield(t)*Efield(t+tau)
    c1,c2=integrate.quad(h,-np.infty,np.infty)
    yy2[j]=c1

plt.plot(tt2,yy2)
```

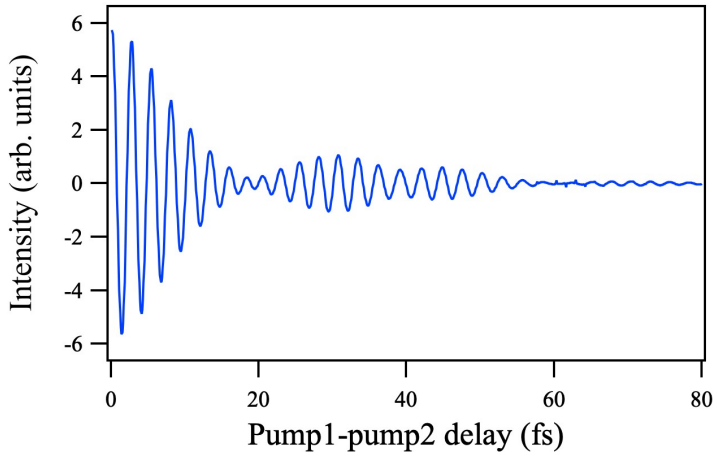

Fig. A.2: Calculated optical interference (θ = 0.5/1000 fs^{-2}).

A.3 Phonon amplitude for python

```
import numpy as np
import matplotlib.pyplot as plt
[E1,E2,E3,E4,E5]=[0.045,0.197,0.385,0.253,0.119]#peak intensity ratio
[L1,L2,L3,L4,L5]=[0.432,0.405,0.379,0.354,0.335]#optical frequency (1/fs)
[S1,S2,S3,S4,S5]=[28.45,30.82,29.94,20.73,44.09]#pulse width (fs)
```

```
def Efield(t): #definition of function for electric field of laser pulse
    EE=E1*np.exp(-t**2/(S1**2))*np.cos(2*np.pi*(L1+chirp*t)*t)\
        +E2*np.exp(-t**2/(S2**2))*np.cos(2*np.pi*(L2+chirp*t)*t)\
        +E3*np.exp(-t**2/(S3**2))*np.cos(2*np.pi*(L3+chirp*t)*t)\
        +E4*np.exp(-t**2/(S4**2))*np.cos(2*np.pi*(L4+chirp*t)*t)\
        +E5*np.exp(-t**2/(S5**2))*np.cos(2*np.pi*(L5+chirp*t)*t)
        return EE
chirp=0.5/1000 #chirp rating
omega=2*np.pi/25.0 #angular frequency of the phonon (vibration period in fs)
hbar=0.656 #eV*fs
eps=7.4 #band gap of diamond
tau1=0.0 #delay of the 1st pulse
def Fa(y,x,tau2):
    FA=Efield(x-tau1)*Efield(y-tau1)*(np.cos(eps/hbar*(y-x))*(np.cos(omega*x)-
np.cos(omega*y))+np.sin(eps/hbar*(y-x))*(np.sin(omega*x)-np.sin(omega*y)))+Efield(x-
tau2)*Efield(y-tau2)*(np.cos(eps/hbar*(y-x))*(np.cos(omega*x)-
np.cos(omega*y))+np.sin(eps/hbar*(y-x))*(np.sin(omega*x)-np.sin(omega*y)))+Efield(x-
tau2)*Efield(y-tau1)*(np.cos(eps/hbar*(y-x))*(np.cos(omega*x)-
np.cos(omega*y))+np.sin(eps/hbar*(y-x))*(np.sin(omega*x)-np.sin(omega*y)))+Efield(x-
tau1)*Efield(y-tau2)*(np.cos(eps/hbar*(y-x))*(np.cos(omega*x)-
np.cos(omega*y))+np.sin(eps/hbar*(y-x))*(np.sin(omega*x)-np.sin(omega*y)))
    return FA
def Fb(y,x,tau2):
    FB=Efield(x-tau1)*Efield(y-tau1)*(np.cos(eps/hbar*(y-x))*(np.sin(omega*x)-
np.sin(omega*y))-np.sin(eps/hbar*(y-x))*(np.cos(omega*x)-np.cos(omega*y)))+Efield(x-
tau2)*Efield(y-tau2)*(np.cos(eps/hbar*(y-x))*(np.sin(omega*x)-np.sin(omega*y))-
np.sin(eps/hbar*(y-x))*(np.cos(omega*x)-np.cos(omega*y)))+Efield(x-tau2)*Efield(y-
tau1)*(np.cos(eps/hbar*(y-x))*(np.sin(omega*x)-np.sin(omega*y))-np.sin(eps/hbar*(y-
x))*(np.cos(omega*x)-np.cos(omega*y)))+Efield(x-tau1)*Efield(y-tau2)*(np.cos(eps/hbar*(y-
x))*(np.sin(omega*x)-np.sin(omega*y))-np.sin(eps/hbar*(y-x))*(np.cos(omega*x)-
np.cos(omega*y)))
    return FB
N=450
YYY=np.arange(0,N,1.0)
tau2=np.arange(0,N,1.0)
```

```
for i in range(N):
    tt=(i*0.2)-3.0
    tau2=tt
    Q1=0
    Q2=0
    for l in range(1001):
        ll = l*0.2-100.0
        lll = ll
        for k in range (l):
            kk = k*0.2-100.0
            kkk = kk
            Q1 = Q1+Fa(kkk,lll,tau2)
            Q2 = Q2+Fb(kkk,lll,tau2)
    Y=abs((Q1**2+Q2**2)**(0.5))
    YYY[i]=Y
plt.xlim([-3,50])
plt.plot(tau2,YYY)
```

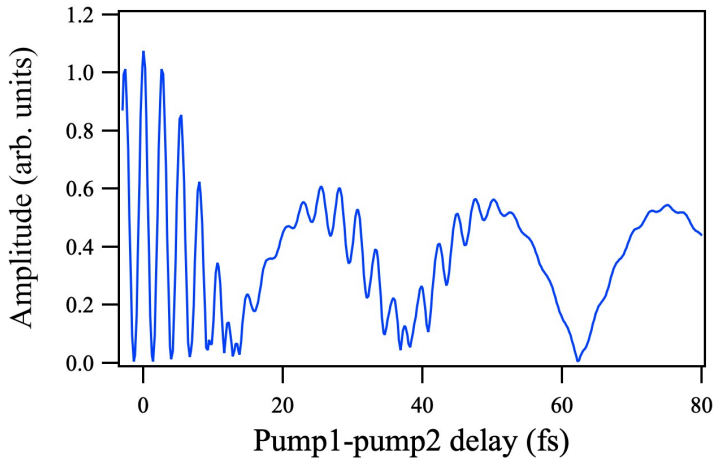

Fig. A.3: Calculated phonon amplitude (θ = 0.5/1000 fs^{-2}).